Evaluation of the Jet Test Method for determining the erosional properties of Cohesive Soils;
A Numerical Approach

Katherine Lourene Weidner

Thesis submitted to the faculty of the Virginia Polytechnic Institute and State University in
partial fulfillment of the requirements for the degree of

Master of Science
In
Civil Engineering

Dr. Panayiotis (Panos) Diplas (Chair)
Dr. Peter J. Vikesland
Dr. Michael F. Hochella

May 2nd, 2012
Blacksburg, VA

Evaluation of the Jet Test Method for determining the Erosional Properties of Cohesive Soils; A Numerical Approach

Katherine Lourene Weidner

ABSTRACT

Estimates of bank erosion typically require field measurements to determine the soil erodibility since soil characteristics are highly variable between sites, especially for cohesive soils. The submerged jet test device is an in situ method of determining the critical shear stress and soil erodibility of cohesive soils. A constant velocity jet, applied perpendicular to the soil surface, creates a scour hole which is measured at discrete time intervals. While the results of these tests are able to provide values of critical shear stress and soil erodibility, the results are often highly variable and do not consider certain aspects of scour phenomena found in cohesive soils. Jet test measurements taken on the lower Roanoke River showed that the results varied for samples from similar sites and bulk failures of large areas of soil were common on the clay banks.

Computational Fluid Dynamics (CFD) can be used to determine the effect of scour hole shape changes on the applied shear stress. Previous calculation methods assumed that the depth of the scour hole was the only parameter that affected the applied shear stress. The analysis of the CFD models showed that depth did heavily influence the maximum shear stress applied to the soil boundary. However, the scour hole shape had an impact on the flow conditions near the jet centerline and within the scour hole. Wide, shallow holes yielded results that were similar to the flat plate, therefore it is recommended that field studies only use jet test results from wide, shallow holes to determine the coefficient of erodibility and the critical shear stress of cohesive soils.

ACKNOWLEDGEMENTS

CONTENTS

LIST OF FIGURES

LIST OF TABLES

1. INTRODUCTION

1.1 INTRODUCTION

Hydropower supplies 7% of the United States' energy and almost two thirds of the nation's renewable energy. While hydropower plants operate without producing air pollution or toxic by-products, there is still a need for research to lessen the impact of dam operation on river ecosystems (NHA 2011). By changing the flow regime of the river, hydropower plants and dams affect the downstream river characteristics including the channel geomorphology by means of erosion. Dam-regulated rivers see adverse effects, such as channel widening and migration (Williams and Wolman, 1984). Changing the river channel structure can affect the suitability of the river as a habitat for fish and other wildlife. The integrity of the channel is important to the vegetation growing at or near the channel bank. Often, trees and plants are left hanging on by just a few roots as the soil supporting them was swept

Figure 1-1 Trees left hanging over the bank after a flood

away during a flood, as seen in Figure 1-1. Furthermore, lateral stream migration can impact the nation's infrastructure by damaging bridges, adjacent roads, water inlets and outlets.

Climate Change will continue to make dam operation more challenging. Extreme weather events are expected to increase the frequency and intensity of rainfall and flooding events. As climatic conditions continue to move away from the conditions used to design most dams, bankfull conditions and overbank flows will become more common. By studying the effect of dam outflows during bankfull conditions on sediment transport, the adverse effects on downstream ecosystems can be mitigated through implementation of new reservoir flow releases.

The purpose of this study is to determine the effect of these new dam outflow schemes on the erosion of cohesive sediment in streams.

Sediment in rivers is transported by erosion from surrounding land areas and from upstream rivers and streams. The amount of sediment entering the oceans is governed by the sediment load carried by the river. This amount changes when the land use surrounding the river changes. Development around the world increases the sediment entering rivers, but development has also led to more reservoirs being built for storage and power generation. The increased sediment load in rivers increases the siltation in reservoirs. Most of this eroded material entering the rivers comes from urban, agricultural, and construction areas, causing streambed erosion to be neglected as a sediment source (Charonko, 2010). Channel erosion contributes 30-40% of the suspended sediment load and the majority of bank erosion is comprised of silt and clay fractions (Odgaard, 1987). The channel bed can be seriously compromised during high flow events leading to loss of bank material and vegetation.

Cohesive sediments, primarily made up of clay and silt particles, behave differently than their non-cohesive counterparts. Cohesive sediments tend to be held together by interparticle forces, rather than gravitational force. Since the behavior of cohesive soils does not follow the sediment transport theory of non-cohesive sediment, empirical methods of developing erodibility parameters are used to estimate channel erosion.

One widely used method of estimating cohesive soil erosion is the excess shear stress equation. This equation is based on the theory that a soil has a critical shear stress, τ_c, under which no soil will be eroded by the flow. When the shear stress exceeds the critical shear stress, erosion will occur. The estimated erosion rate is adjusted by applying a coefficient of erodibility, k_d. This coefficient, like the critical shear stress, is a property of the soil bed.

In order to predict river bed erosion rates, the soil properties needed for the excess shear stress equation must be known. The submerged jet test is an in situ field test used to determine the critical shear stress and the coefficient of erodibility of a soil. The jet test uses a tank of constant head to supply a circular jet used to impact the soil bed at a right angle. This simple and inexpensive test is used to document the scour hole depth generated in the soil bed due to the impinging jet as time elapses.

Using the observed erosion rate during the jet test, the two unknown soil parameters can be found through an iterative procedure. This numerical procedure makes many assumptions

including that the soil boundary is behaving like a smooth, flat plate. While this assumption might hold true for the initial conditions, where the soil is relatively flat, though not completely smooth, as a scour hole develops the jet is no longer impinging against a flat surface. Currently there is no research into how the jet test behaves as the geometry of the soil surface changes over time. A better understanding of how the shear stress acting on the soil profile changes as the test progresses will help to achieve better field results. More accurate estimates of a site's erosion parameters will help to estimate future erosion.

1.2 GOALS AND OBJECTIVES

The main goal of this project is to better understand the limits of the submerged jet test and the methods used to determine the critical shear stress and the coefficient of erodibility using the jet test results. The specific objectives are:

- Use field data and lab data to determine model parameters that characterize the majority of jet test conditions and scour hole geometries that are encountered in the field.
- Evaluate shear stress and velocity profiles across jet created scour holes of different aspect ratios and depths.
- Examine the assumptions in the numerical methods for solving the excess shear stress equation for the critical shear stress and the coefficient of erodibility.

2. Literature Review

2.1 Effect of Dams on Erosion

Erosion, both overland and in rivers, is heavily affected by human development. Land development increases overland erosion. This increased eroded material is transported to the oceans through rivers. When a river is impounded by a reservoir, the majority of the transported load is settled out. This siltation in the reservoir can severely decrease the storage volume of the reservoir (Syvitski, Vorosmarty, Kettner and Green, 2005).

When a dam is constructed on a river, the flood peaks are always decreased. The exact effect of the flow changes on the river are difficult to quantify, since dams may have many types of flow regimes. Though the impact is hard to define explicitly, many trends are evident. River sediment is trapped in the reservoirs behind the dam, either incidentally, which is true in the case of most hydropower facilities, or by design in order to reduce downstream aggregation of material. Overall the decrease in sediment load in a dam controlled river is significant. The average trap efficiency of dams is greater than 99% and most rivers do not recover their sediment load until far downstream, often hundreds of kilometers (Williams and Wolman, 1984).

The decrease in downstream sediment load results in bed degradation as the river begins to approach the recovery of its sediment. Bed degradation is well known in alluvial streams downstream of dam structures when the river is not constrained by bed rock. Most of this degradation occurs within the first few decades after dam closure. These geomorphic changes to the river are proven to be the effects of dam construction because of four main reasons. First, the greatest bed degradation is found at or near the dam, then as the distance from the dam increases the amount of degradation noticeably decreases. Also, most rivers were seen to be at a stable state prior to dam closure and saw degradation only after the dam was completed. Downstream of dams, there is usually a large amount of bed erosion but upstream there is little or no change in bed elevation. Finally, if post-dam closure degradation rates were extrapolated back to pre-dam times, the resultant bed elevations would be unrealistically high (Williams and Wolman, 1984).

Degradation downstream of a dam will continue to occur until a constraint is met. This constraint can be local controls such as bedrock or armor, downstream base level controls such as oceans or reservoirs, a decrease in the flow's ability to erode the sediment, infusion of

sediment from another source such as a tributary, or growth of vegetation. The degradation continues downstream as time passes. Downstream sites experience a lag time before the degradation effects of the dam are felt (Williams and Wolman, 1984).

2.2 SHEAR STRESS AND INCIPIENT MOTION CONCEPTS

A.F. Shields (1936) first defined sediment entrainment in terms of dimensionless shear stress. The Shields diagram is used to find critical shear stress based on the representative grain size of the sediment. Discrepancies can be found in critical shear stress approximations by using slightly different definitions of incipient motion. Shields' work, and those that followed, contributed to defining a threshold force below which incipient motion would not occur (Buffington, 1999, Buffington and Montgomery, 1997).

The critical shear stress approach is related to the time-averaged shear stress in the channel. Turbulence in the channel can contribute to the likelihood of incipient motion due to sudden peaks in velocity and associated stresses. Turbulence in natural streams can be increased by the presence of structures which create vortices within the flow. Sumer et al. (2003) found that turbulence had a greater effect when there were greater values of bed shear stress. Also, higher turbulence levels led to higher rates of sediment transport.

While Shields concentrated on the force on a grain needing to exceed a threshold value in order to become entrained in the flow, Diplas et al. (2008) showed that the impulse had to exceed a critical value. Therefore if the application time of the force was long enough, the critical force would cause a grain to move. When the time applied was very small, a larger force was required to meet the impulse needed to create incipient motion. While there still is a minimum force for incipient motion, the time of application is also important.

Two types of incipient motion are saltation and rolling. Saltation is created by lift force action on the grain. Rolling is caused by a combination of drag and lift forces. Saltation occurs when the grain is surrounded by neighboring particles and at stresses well above the critical value. Rolling occurs when the particle is fully exposed to the flow and at conditions very close to the threshold of motion. Force-duration, or the impulse concept, was proven to be a more suitable criterion for both types of motion. The Impulse method takes into account the time history of turbulent fluctuations. Peaks can surpass the force threshold but sufficient duration is

required to create enough impulse to entrain a soil particle (Valyrakis, Diplas, Dancey, Greer and Celik, 2010).

2.3 COHESIVE SOIL EROSION

Estimating the erosion rate of clay soils must take into account effects of cohesion. Critical shear stresses for cohesive soils are larger than would be expected using noncohesive models (Ternat, Boyer, Anselmet and Amielh, 2008). Cohesive sediment is made up of clay, silt, fine sand, organics, inorganic chemicals and water. The solid phase is characterized by its size distribution. Clay minerals exhibit cohesion due to their small size and flat shape resulting in a high surface area with a charge distribution. The soil components are made up of silicate minerals, salts, oxides, and hydroxides. The amount of particulate organic matter (POM) and dissolved organic carbon (DOC) affect the floc formation of the sediment. The organic materials act as polymers allowing the clays to sorb onto them to form larger flocs (Winterwerp and van Kesteren, 2004).

Detachment of cohesive sediments can be induced through two processes: Hydraulic erosion and Subaerial erosion. Hydraulic erosion is caused by lift and drag forces imposed by flow. Subaerial erosion is the weakening and weathering of bank material by soil moisture conditions. Subaerial erosion is created by the groundwater interaction and seepage within the river banks (Julian and Torres, 2006).

There is a link between hydraulic erosion and the excess shear stress applied to the banks due to the channel flow. The excess shear stress equation is

$$E = k_d \left(\tau - \tau_c \right)^{\xi} \tag{1}$$

Where,

E=erosion rate

k_d=erodibility coefficient

τ=applied shear stress

τ_c=critical shear stress

ξ= exponent, usually assumed to be unity

Surface erosion and mass erosion are the two main types of hydraulic erosion. Surface erosion, or particle erosion, is the detachment of individual particles and or aggregates (Mostafa, Imran, Chaudhry and Kahn, 2008). Mass erosion is when clusters or lumps of aggregates break

away at the same time. This type of erosion is more difficult to predict and quantify (Zhu, Lu, Liao, Wang, Fan and Yao, 2008).

The rate of erosion is susceptible to a large number of factors. As the clay fraction is increased, the erosion resistance also increases. The erosion rate of the soil is affected by the salinity, pH, sodium adsorption ratio, the chemical composition of the pore water, and the properties of the eroding fluid (Zhu, Lu, Liao, Wang, Fan and Yao, 2008). Properties of the soil play an important role as well. Some properties include moisture content, bulk density, soil type, clay and organic content, plasticity, size distribution, aggregate sizes, and dispersion ratio (Charonko, 2010). The composition of the suspended load and the bed load of a river is based on the crust bedrock type, weathering, and sorting. The suspended load concentration increases with depth and is defined by the Rouse profile (Bouchez, Gaillardet, France-Lanord, Maurice and Dutra-Maia, 2011).

The erodibility of cohesive sediments can be affected by the aggregation of particles during settling. The settling of particles is usually governed by Stoke's law, but the effective viscosity of the fluid can be complicated to define. The effective velocity is modified by nearby suspended particles. Well mixed suspension will start to settle as ungraded, but as the larger particles push past smaller particles during settling, a graded deposit will begin to form (Dorrell, Hogg, Sumner and Talling, 2011). Settling has three main categories: clarification, zone settling, and compression. In zone settling, sediment settles in groups and sometimes water escapes from the layers through preferred flow paths, or channels. Channel formation was observed whenever there was flocculation during settling. As the solids in lower zones are compressed by the accumulating load, the light water is pushed upward through channels (Nam, 2005, Nam, Gutierrez and Diplas, 2008).

2.4 THE THEORETICAL SUBMERGED CIRCULAR IMPINGING JET

For a submerged turbulent jet, there is initially a zone of establishment where the potential core exists. Eddy regions are formed as the jet enters the stagnant fluid. These eddies are the result of the jet flow entraining the surrounding fluid. This zone ends end the jet becomes completely turbulent at the point where the expanding eddy regions meet (Albertson, Dai, Jensen and Rouse, 1949). The length of the potential core is approximately 6d (where d = the diameter of the jet). Beyond the potential core, the jet is fully developed (Beltaos and Rajaratnam, 1977).

An impinging circular jet is made up of three distinct regions as shown in Figure 2-1. In the first one, the free jet region, the jet behavior is independent of any wall effects. The impingement region contains the stagnation point and the major deflection of the jet. The final zone is the wall jet zone, where the jet behaves as a radial wall jet with all flow acting parallel to the wall (Beltaos and Rajaratnam, 1977). The jet feels the effect of the wall at approximately $x/H \geq 0.86$, where x is the distance measured from the jet origin and H is the height of the jet origin above the flat plate (Rajaratnam, 1976).
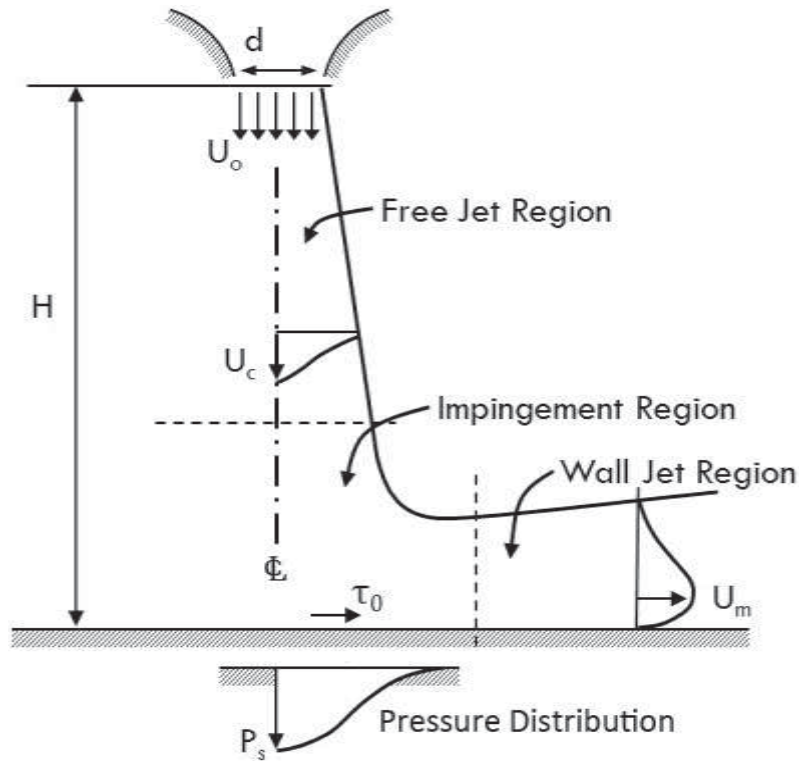
Figure 2-1 Turbulent Jet Impacting a Flat Plate

The flow at the stagnation point of an impinging turbulent jet can be characterized by irrotational flow. The velocity and pressure distributions are such that the maximum velocity occurs away from the centerline of the jet (Poreh and Cermak, 1959)

The pressure distribution on the flat wall is given by (Rajaratnam, 1976):

$$\frac{P_w}{P_s} = \exp\left(-114\left(\frac{r}{H}\right)^2\right) \tag{2}$$

Where,

$$\text{Stagnation Pressure} = P_s \approx \frac{50}{(H/d)^2} \frac{\rho U_0^2}{2} \tag{3}$$

8

The bed shear stress increases linearly with radial distance up to a maximum value, τ_{0max}, and then decreases. The equation for τ_{0max}, where τ_{0max} occurs at $r = 0.14H$, is given by (Beltaos and Rajaratnam, 1974):

$$\tau_{0max} = 0.16 \, \frac{\rho U_0^2}{\left(\frac{H}{d}\right)^2}$$

(4)

2.5 EROSION BY JETS AND THE JET EROSION TEST

The ASTM Standard procedure (ASTM, 2000) is to measure the maximum depth of material removed while maintaining a constant pressure. The constant pressure will ensure that the jet maintains a constant exit velocity. The discrete time steps at which depth measurements are taken are at the user's discretion. According to the standard the velocity of the jet at the nozzle is found using the following equation:

$$U_o = C \sqrt{2gh}$$

(5)

Where,

U_o= jet velocity

C= nozzle coefficient

g= acceleration due to gravity

h= pressure head acting on the jet

The jet test is repeatable and provides a reasonable measurement of erosion parameters in the field (Charonko, 2010). The device is useful as it is relatively easy to use during fieldwork (Potter, Velázquez-Garcia and Torbert, 2002). The procedure for determining the k_d and τ_c of the soil is based on a combination of Blaisdell's (1981) and Stein's (1997) method for determining the equilibrium scour depth (Hanson and Cook, 1997).

In jet erosion tests, three types of erosion are encountered: flake, surface erosion, and mass erosion (Mazurek, Rajaratnam and Sego, 2003). Flake erosion is when circular flakes of approximately 1-3mm in diameter and less than 0.5 mm thick are pulled away. Removal of these flakes formed a scoured circle around the jet centerline. Mass erosion is erosion of small to large chunks ripped or torn from soil body. Moore and Masch (1962) noticed that this type of erosion play a large part in skewing time versus scour depth data. Rapid Surface erosion occurs at higher stresses, greater than 200 Pa. There is no obvious removal of large chunks, just particle by particle erosion rapidly occurring. This type of erosion usually occurred near the beginning of

9

the test. Though rapid surface erosion occurred early on during jet tests, the total contribution to the amount of scour was small in comparison to the other mechanisms (Mazurek, Rajaratnam and Sego, 2001).

The jet erosion test uses an equilibrium depth of scour to determine the critical shear stress of the soil. As jet scour hole size increases with time, the applied shear stress decreases due to increasing dissipation of jet energy. Therefore, detachment is initially high and asymptotically approaches zero. The applied shear stress approaches the critical shear stress as the distance from the jet origin to the soil bed increases. The actual maximum depth of the scour hole at equilibrium, $\epsilon_{m\infty}$, depends on multiple properties:

$$\frac{\epsilon_{m\infty}}{H} = f_1 (M_0, \rho, H, \mu, \tau_c) \tag{6}$$

Where,

$\epsilon_{m\infty}$ = maximum depth at equilibrium

M_0 = Momentum Flux from the nozzle, $M_0 = \frac{\pi}{4} d^2 \rho U_0^2$

d = the diameter of the nozzle

U_0 = the velocity at the nozzle

H = height of jet above the clay surface

τ_c = critical shear stress

Through dimensional analysis, this relation can be simplified to:

$$\frac{\epsilon_{m\infty}}{H} = f_2 \left\{ \frac{\rho U_0^2 \left(\frac{d}{H}\right)^2}{\tau_c}, \frac{\rho U_0 d}{\mu} \right\} \tag{7}$$

Therefore, the max depth is a function of the jet Reynolds number and the ratio of max shear stress on the bed to the critical shear stress of the bed material. Since at high Reynolds numbers (greater than 10,000) there is only a mild dependence upon Reynolds number, the contribution of the second parameter can be ignored (Poreh, Tsuei and Cermak, 1967). Mazurek (2001) assigned the variable X to be equal to the max shear stress: $X = \rho U_0^2 \left(\frac{d}{H}\right)^2$. Assuming that X equals the critical shear stress at X_c, the parameter $\frac{\rho U_0^2 \left(\frac{d}{H}\right)^2}{\tau_c}$ can be rewritten as $\frac{X - X_c}{X_c}$ and used to correlate with the maximum scour depth, center line scour depth, and scour hole volume.

The shape of the scour hole can affect the scour equilibrium. Deep holes can form when the velocity gradient in the impingement zone is high. Shallow holes form when the velocity at the impingement point does not decrease as much when the radius increases (Hollick, 1976). When the ratio of H/d is low (less than 7), scour holes are observed to be deep and narrow. Higher values of H/d create wide, ratios greater than 7, shallow scour holes (Moore and Masch, 1962). Mazurek (2001) defined these two types of scour holes as strongly and weakly deflected. The strongly deflected jet created a narrow and deep profile due to the jet being almost completely reversed upon impingement of the soil. The weakly deflected jet created wider and shallower scour holes than the strongly deflected jet. Strongly deflected jet scour holes had less volume probably due to the momentum dissipated by the entrainment of the return flow of the jet within the scour hole.

In jet tests on sand and clays, the scour holes are found to grow linearly with the logarithm of time. For sand, at small times, t, the ϵ_{max} was located away from the jet centerline, but at large values of t, ϵ_{max} was on the jet centerline (Rajaratnam and Beltaos, 1977). In cohesive soils, the location of ϵ_{max} was more dependent on the type of jet, either strongly or weakly deflected. For strongly deflected jets, $\epsilon_{max} = \epsilon_{CL}$, but the ϵ_{max} location for weakly deflected jets was variable (Mazurek, 2001). Scour profiles at equilibrium were found to be similar in both sand and clays (Mazurek, Rajaratnam and Sego, 2001, Rajaratnam and Beltaos, 1977). Both strongly and weakly deflected scour holes plot on the same curve when normalized using the maximum depth and radius of the scour hole (Mazurek, 2001).

The equilibrium scour depth for a jet test on cohesive soil was reached after 80 to 100 hours of testing, while most field jet tests are performed for around 1 hour. Field jet tests use extrapolation methods to determine the equilibrium depth based on the scour depths measured during the test. The goal of the jet test is to determine the critical stress, τ_c, and the erodibility coefficient, k_d, as defined in equation 1, the excess shear stress equation (Hanson and Cook, 2004). The critical shear stress, τ_c, and the erodibility coefficient, k_d, are related. High critical shear stresses corresponded to low k_d values. Similarly, low values of τ_c corresponded to higher k_d values (Arulanandan, 1980).

The jet test calculation finds the two erosional parameters using two separate techniques. The critical shear stress is found by fitting a curve to the depth data in order to determine the equilibrium depth. This curve equation is based on Blaisdell's (1981) work in determining

equilibrium depth of a hole created at a plunge pool. The second step is to find the erodibility coefficient. This stage uses Stein's (1997) method of fitting the integral of the excess shear equation to the depth over time data.

Many assumptions are made in the solution procedure developed for determining the critical stress, τ_c, and the erodibility coefficient, k_d. One assumption is that the peak shear stress value causes the max scour beneath the impinging jet. As the jet impinges on the boundary, a stagnation point forms that creates a maximum pressure (and normal stress) along with a shear stress of zero along the centerline. In addition, the equations are developed assuming that the exponent of the excess shear stress equation is 1 and that the jet is acting on a flat smooth surface (Stein and Nett, 1997). The solution for the jet test is different depending on whether the impingement zone is within the potential core of the jet. In the potential core, the shear stress, τ, is equal to the initial shear stress, τ_0. Beyond the potential core the shear stress is inversely related to the distance, H, from the jet origin along the centerline (Stein and Nett, 1997). In the jet setup, the jet nozzle is placed at least six to nine jet diameters above the soil surface to ensure that the impingement zone is beyond the potential core (Hanson and Cook, 1997).

Mazurek (2009) compared Blaisdell's (1981) method of estimating the equilibrium depth with experimental values of the equilibrium depth found using a jet test device. Blaisdell's approach yielded lower τ_c numbers because the equilibrium depth was overestimated based on "early" test data. The value of k_d was found to depend on the length of time the test was run. As test duration increased, the value of k_d decreased. Since Blaisdell (1981) assumed that the jet was deflected by a flat plate, the overestimation could be expected. His method did not consider the decay of velocity caused by reverse flow of the jet after hitting the scour hole. The experiments also showed a dependence of the critical shear stress on the aspect ratio of the scour hole.

.

3. BACKGROUND

The goal of this research is to analyze the impact of the changing shape of a scour hole on the applied shear stress. In order to assess the effect of the scour hole shape, a series of numerical models representing different scour hole geometries were built to compare to a flat plate model. The chosen scour holes geometries were determined from results from previous field studies on the lower Roanoke River and from laboratory studies on erosion of clay materials by a submerged jet. The results from each scour hole model were compared to the flat plate results in order to determine the validity of the flat plate assumption used in the jet test calculation of critical shear stress.

3.1 JET TEST DEVICE

The geometry of the FLUENT model was based on the dimensions of the jet erosion test. The Jet test apparatus is made up of a jet tube, adjustable head tank, and a jet submergence tank as shown in Figure 3-1. The submergence tank has an inner diameter of 30 cm. Prior to the start of the test, the submergence tank is pressed into the soil and filled with water. The water enters the submergence tank through the nozzle at the end of the jet tube. The jet tube has a diameter of 9 cm and the nozzle diameter is 0.64 cm (Hanson 2004).
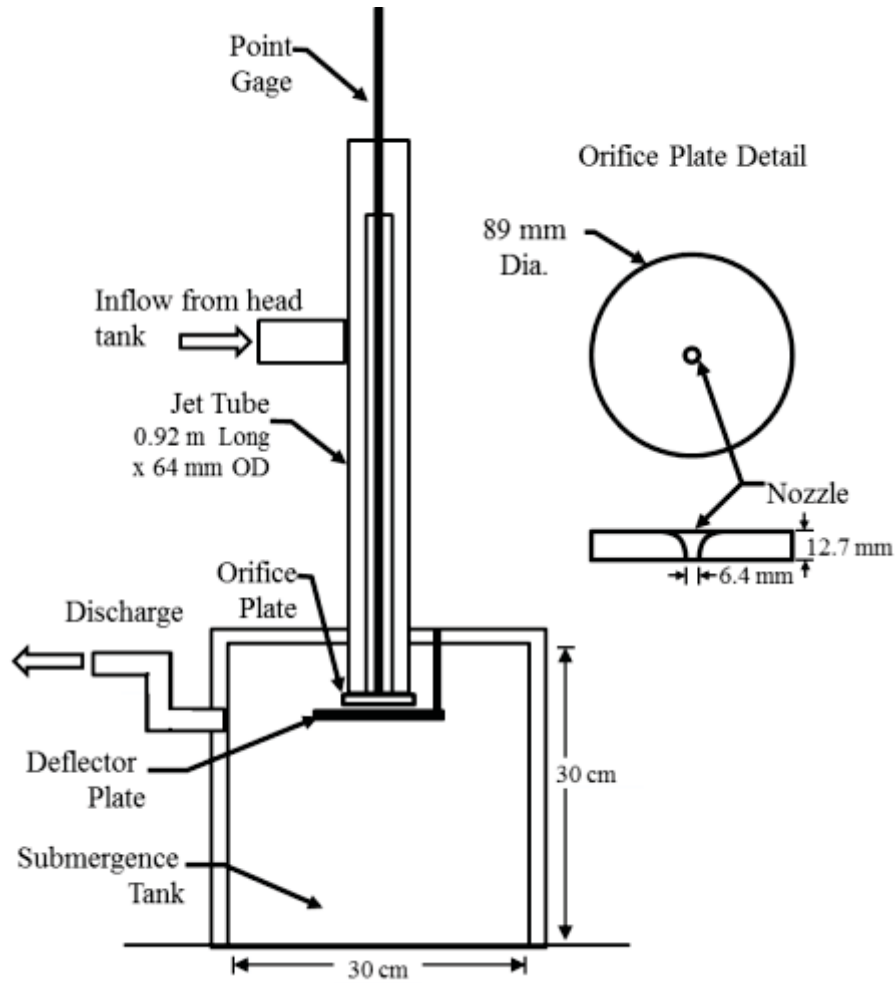
Figure 3-1 The Jet Erosion Test Apparatus (Hanson 2004)

The results of the jet test include the time intervals and the scour depth at each time. The distance from the jet nozzle to the initial flat soil bed, H_0, is measured prior to the start of the test. The velocity of the jet near the soil boundary can be determined using the scour hole depth and the initial distance to the soil boundary. Disregarding wall effects, the centerline velocity of the jet, U, in the region of $H>H_p$ is given by:

$$\frac{U}{U_0} = C_d \frac{d}{H} \tag{8}$$

Where,

U_0 = jet velocity at the nozzle

C_d = diffusion coefficient, avg C_d=6.2

d = nozzle diameter

H = distance from the jet origin

In the wall jet zone, the jet flow is parallel to planar boundary. Shear stress is defined as:

$$\tau = C_f \rho\, U^2 \tag{9}$$

The velocity parallel to the bed is assumed to be equal to the jet velocity at the distance, H, from the jet nozzle. Therefore combining equations 8 and 9, the shear stress based on the Jet velocity is

$$\tau_0 = C_f \rho \left(C_d U_0 \frac{d}{H}\right)^2 \quad \text{when H>H}_p \tag{10}$$

Where,

C_f=friction coefficient

The friction coefficient, C_f, is independent of the Reynolds number if the Reynolds number is sufficiently large and the boundary surface is not perfectly smooth. In open channels, the friction factor is dominated by the surface roughness and is usually found empirically (Sabersky, Acosta, Hauptmann and Gates, 1999). Hanson (1997) determined the friction coefficient for the jet erosion test to be 0.00416.

By defining the erosion rate of the soil as equal to the change in depth over time, the rate of change of scour can be substituted into the excess shear stress equation:

$$\frac{dH}{dt} = k_d \left(\tau_0 \left(\frac{C_d d}{H}\right)^2 - \tau_c\right) \quad \text{for H} \geq \text{H}_p \tag{11}$$

When scour no longer occurs (dH/dt = 0), the equilibrium depth has been reached (H = H_e). Therefore,

$$\tau_c = \tau_0 \left(\frac{C_d d}{H_e}\right)^2 \tag{12}$$

Through application of equation 10, the shear stress acting on the flat plate can be defined as $\tau_{oFP} = C_f \rho \left(C_d U_o \frac{d}{H_o}\right)^2$. The shear stress at the depth of the scour hole is $\tau_{o\epsilon} = C_f \rho \left(C_d U_o \frac{d}{H_o + \epsilon}\right)^2$.

By dividing the flat plate equation by the scour hole equation, the relationship between shear stress on the flat plate and the shear stress on the eroded scour hole is:

$$\tau_{o\epsilon}=\frac{H_o^2}{(H_o+\epsilon)^2}\ \tau_{oFP}\tag{13}$$

By using dimensionless analysis, a theoretical time can be found to compare to the measured time. The dimensionless parameters used are:

$$H_p^*=\frac{H_p}{H_e}\qquad H^*=\frac{H}{H_e}\qquad T^*=\frac{t}{T_r}\qquad T_r=\frac{H_e}{k\tau_c}$$

The time is found by integrating the excess shear equation (equation 1):

$$t_m=T_r\left(0.5\ln\left(\frac{1+H*}{1-H*}\right)-H*-0.5\ln\left(\frac{1+H_{i*}}{1-H_{i*}}\right)+H_{i*}\right)\tag{14}$$

3.2 THE EQUILIBRIUM SCOUR HOLE (MAZUREK 2001)

Mazurek conducted a series of laboratory jet tests on cohesive soil materials. The tests varied the flow rate, the nozzle height, and the nozzle diameter. Each jet test was run until the scour hole reached an equilibrium depth. The time to reach equilibrium depth was about 80 to 100 hours. The depth, radius, and volume of the scour hole were measured at discrete time steps. At equilibrium, the geometry of each scour hole was measured by measuring the depth along two perpendicular radii from the center of the jet to the edge of the disturbed soil. The study also determined that the shape of the scour hole, both for narrow, strongly deflected curves and for wide, weakly deflected curves could be well represented by a sine curve.

Mazurek (2001) found that these ratios ranged from 0.55 to 5.7. Ratios of 0.5, 1, 2.5 and 5 were chosen as ratios of interest. A ratio of 0.5 represents a narrow scour hole, while a ratio of 5 indicates a wider scour hole. The average ratio was around 2. The majority of the values fell within the 1 to 3 range. Many narrow holes were seen about the 0.5 mark, but only a few cases reached the very wide case of a ratio of 5 or more. A plot of this distribution can be seen in the appendix.

Mazurek (2001) defined narrow and wide holes by the strength of the jet applied to the surface. Strongly deflected jets created deep, narrow scour shapes while weakly deflected jets led to wide, shallow holes. The tendency of a jet to create either type of scour hole depended on the ratio of the excess stress to the critical shear stress. Wide, shallow scour holes tend to form to ratios less than five, while deep scour holes tend to form for stress ratios greater than 5. Table 3-1 summarizes Mazurek's observations on narrow and wide holes.

16

Table 3-1 Characteristics of different scour hole geometries

Strongly Deflected Jets	Weakly Deflected Jets
Narrow, Deep Scour	Wide, Shallow Scour
Jet is completely reversed upon soil impingement	Greater total volume of eroded material than seen in narrow scour holes
$\epsilon_{max} = \epsilon_{CL}$	The location of ϵ_{max} was variable, not always occurring at the jet centerline

3.3 FIELD TESTS ON THE LOWER ROANOKE RIVER

Approximately 30 field jet erosions tests were performed on the banks of the lower Roanoke River near Scotland Neck, NC. The measurements were taken as part of a study to determine the effect of hydropower dams on bank erosion in the downstream reach. There jet tests were carried out at several locations downstream of the Roanoke Rapids dam. A map of the study area is presented in Figure 3-2.
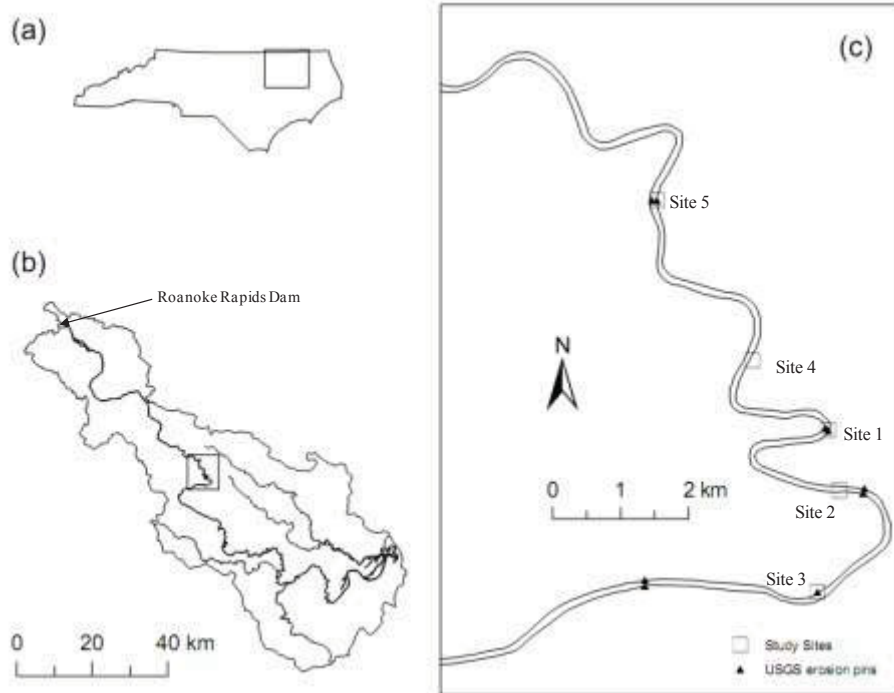
Figure 3-2 (a) North Carolina with a box showing the location of the Roanoke River watershed that falls within North Carolina. (b) The Roanoke River watershed below the Roanoke Rapids Dam with a box showing the location of the study reach. (c) The study reach on the lower Roanoke River.

The reach downstream of the Roanoke Rapids dam has been subjected to high levels of bank erosion and failure. The lower Roanoke River's bank material is made up of mostly silts

Table 3-1 Characteristics of different scour hole geometriesand clays. Soil samples from the jet test sites were tested in the laboratory. The soils were classified as low plasticity silts (ML), high plasticity silts (MH), and low plasticity clay (CL) by the unified soil classification system (USCS). The clay content of the soils ranged from 26% to 46% by weight. Grain size distributions for the three types of soils are seen in Figure 3-3 (Nam, 2010).
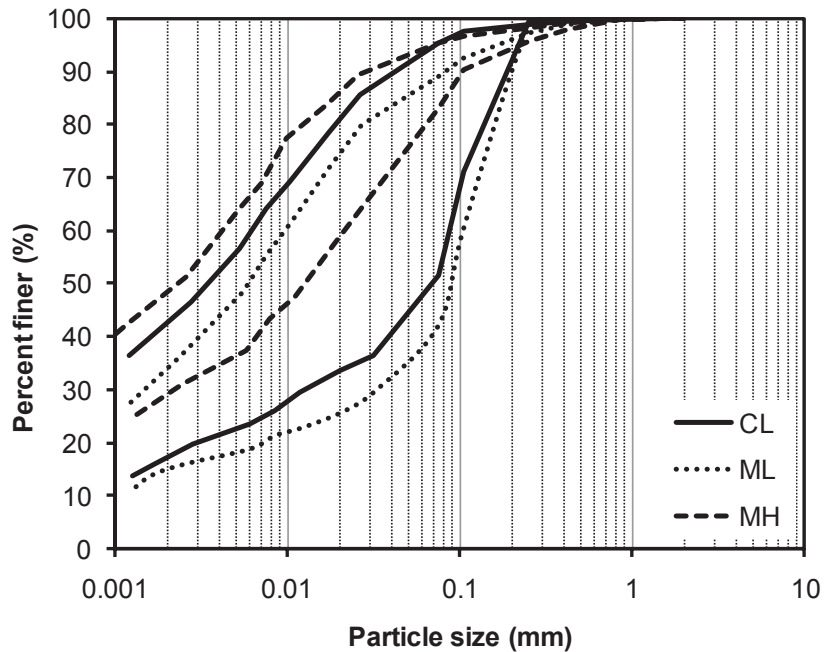
Figure 3-3 Particle size distribution curve

The jet erosion tests from the Lower Roanoke River resulted in large variations in the erosive properties of the soil even in tests from the same site. This is consistent with results reported in the literature (Hanson 2004, Mazurek 2001). The critical shear stress of the soil ranged from less than 1 Pascal to as high as 21 Pascals. The minimum and the maximum critical shear stress were found at the same site. Large amounts of variation from test to test were seen at all five sites. In general, the jet tests showed that smaller final scour hole depths corresponded to high values of critical shear stress, τ_c, and low erodibility coefficients as seen in Figure 3-4**Error! Reference source not found.**.
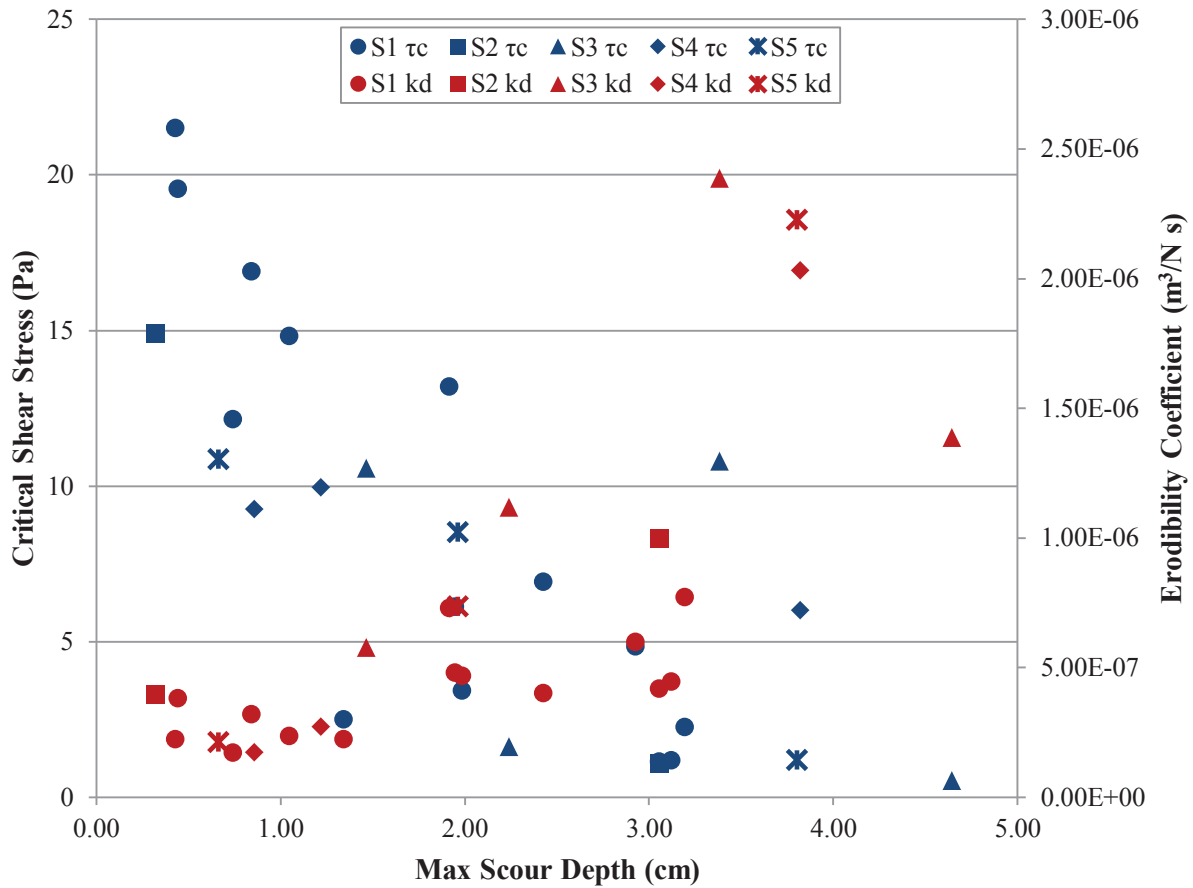
Figure 3-4 Relation between Scour Depth and Excess Shear Stress Equation Parameters

In addition to dependence on the maximum scour depth, the critical shear stress and the erodibility coefficient changed based on the path of the depth versus time curve. Figure 3-5 shows the depth and time data for four jet erosion tests performed at site 1. The head tank heights in the four tests ranged from 2.2 m to 2.61 m. In Test 1, there was very little rate of change in the depth. The test only reached a maximum depth of 0.44 cm. The results found a high critical shear stress, τ_c = 19.54 Pa, based on the low depth and slow rate of change of depth. The opposite was seen in Test 6. The depth of the scour hole grew steadily over the 45 minute period resulting in a final measured depth of 3.06 cm. The critical shear stress was calculated to be much lower, τ_c = 1.14 Pa. Tests 8 and 9 resulted in similar final depths. The depths were 1.92 and 1.99 cm, respectively. The depths in Test 9 increased gradually over the time period, but in Test 8 there was a large initial jump in the depth followed by a slow rate of change in depth for the remainder of the time period. Test 9 resulted in a critical shear stress of 3.42 Pa. Test 8 resulted in a much higher critical shear stress of 13.19 Pa because of the slow rate of change in the depth after the

19

initial mass erosion. Using the critical shear stress calculated from Test 9 would estimate a much greater amount of erosion than using the parameters calculated in Test 8.

	S1T1	S1T6	S1T8	S1T9
Head Tank Height (m)	2.20	2.61	2.50	2.59
Max Scour Depth (cm)	0.44	3.06	1.92	1.99
Nozzle Height, H (cm)	9.87	9.08	9.36	10.46

$\tau_c = 1.14$ Pa
$k_d = 4.16 \times 10^{-7}$ m³/N s

$\tau_c = 13.19$ Pa
$k_d = 7.28 \times 10^{-7}$ m³/N s

$\tau_c = 3.42$ Pa
$k_d = 4.67 \times 10^{-7}$ m³/N s

$\tau_c = 19.54$ Pa
$k_d = 3.79 \times 10^{-7}$ m³/N s
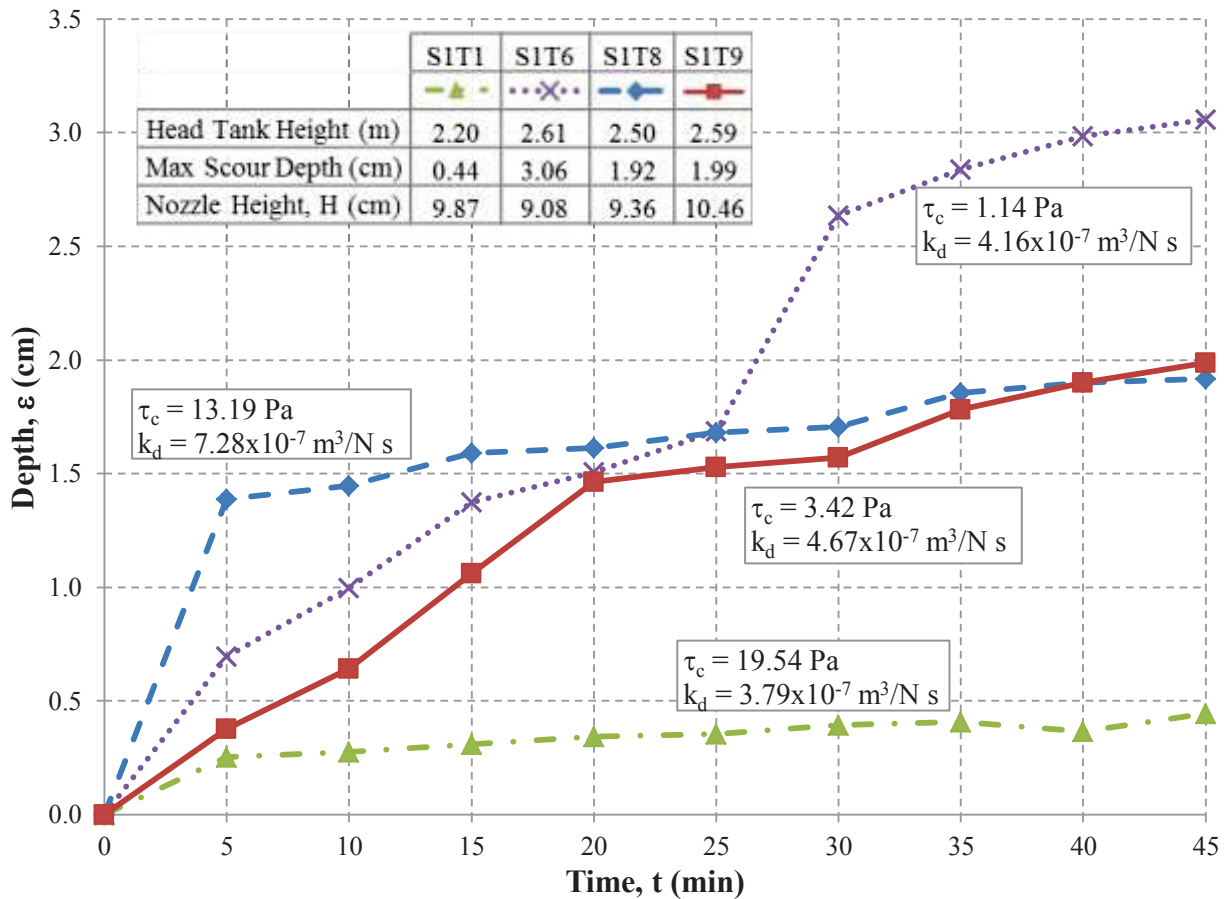
Figure 3-5 Depth data from Jet Erosion Tests on Site 1 on the lower Roanoke River

The measured depths varied between 0.32 cm and 8.8 cm. The majority of the depths were less than 3 cm as seen in **Error! Reference source not found.**, with almost a third of the values being less than 1 cm. The maximum depth measured in the test depended on the head tank height, which determined the jet velocity, as well as the soil properties. Bulk failures of large aggregates of soil can also increase the measured depth. In future testing, similar depths would be expected to be seen in jet tests on clay and silt soils.
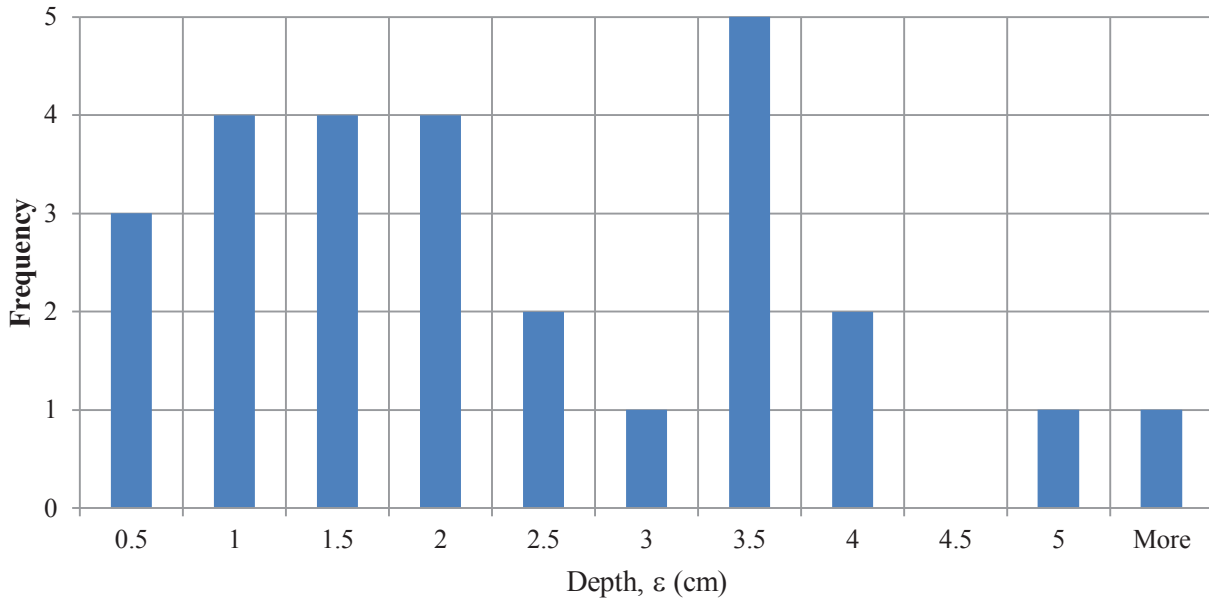
Figure 3-6 Scour depths measured using a Jet Test on the lower Roanoke River

A range of depths was chosen to use in the numerical model to represent the scour depths seen in the Lower Roanoke River study. The chosen depths are 0.5 cm, 1 cm, 2.5 cm, and 5 cm.

4. NUMERICAL SIMULATION OF JETS

4.1 OVERVIEW OF CFD MODELING

ANSYS FLUENT 13 was used to model the jet erosion test. FLUENT is part of ANSYS's workbench platform for constructing computational fluid dynamic models. FLUENT uses equations for conservation of mass and momentum, in addition to turbulence closure methods, to model flow and turbulence (Theory guide). ANSYS Design Modeler and Meshing were used to define the geometry of the tests and mesh the flow area.

The jet test was modeled using 2D axisymmetric Reynolds averaged Navier Stokes equations. The 2D axisymmetric equation for continuity is

$$\frac{\partial \rho}{\partial t} + \rho \left[\frac{\partial}{\partial x}(\rho u) + \frac{\partial}{\partial r}(\rho v) + \frac{\rho v}{r} \right] = S_m \qquad (15)$$

Where,

x = axial coordinate

r = radial coordinate

u = axial velocity

v = radial velocity

S_m = Mass added to the continuous phase

The 2D axisymmetric equations for momentum conservation are

$$\rho \left[\frac{\partial u}{\partial t} + \frac{1}{r}\frac{\partial}{\partial x}(ru^2) + \frac{1}{r}\frac{\partial}{\partial r}(ruv) \right] = -\frac{\partial P}{\partial x} + \frac{1}{r}\frac{\partial}{\partial x}\left[r\mu \left(2\frac{\partial u}{\partial x} - \frac{2}{3}(\nabla \cdot \vec{V}) \right) \right] + \frac{1}{r}\frac{\partial}{\partial r}\left[r\mu \left(\frac{\partial u}{\partial r} + \frac{\partial v}{\partial x} \right) \right] + F_x \qquad (16)$$

$$\rho \left[\frac{\partial v}{\partial t} + \frac{1}{r}\frac{\partial}{\partial x}(ruv) + \frac{1}{r}\frac{\partial}{\partial r}(rv^2) \right] = -\frac{\partial P}{\partial r} + \frac{1}{r}\frac{\partial}{\partial x}\left[r\mu \left(\frac{\partial v}{\partial x} + \frac{\partial u}{\partial r} \right) \right] + \frac{1}{r}\frac{\partial}{\partial r}\left[r\mu \left(2\frac{\partial v}{\partial r} - \frac{2}{3}(\nabla \cdot \vec{V}) \right) \right] - 2\mu \frac{v}{r^2} + \frac{2}{3}\frac{\mu}{r}(\nabla \cdot \vec{V}) + F_r$$
$$(17)$$

The choice of turbulence model in computational fluid dynamics is important to verify that a solution is properly converged and valid. While no one turbulence model is considered "the best," several Reynolds Averaged Navier-Stokes turbulence models are applicable to hydraulic problems, like the jet test.

One widely used method is the k-ϵ method. This is a 2 equation, semi-empirical model. It is widely used due to its robust nature, calculation economy, and reasonable accuracy. K is the turbulent kinetic energy and ϵ is the dissipation coefficient (Theory guide). This method has three different types: the standard method, the realizable method and the renormalization group theory (RNG) method. The k-ϵ models are heavily used because they provide reasonable

accuracy over a wide range of different types of problems. Unfortunately, these models are susceptible to adverse pressure gradients and boundary layer separation (Users guide). The RGN method improves the accuracy of the standard method, especially with the effect of swirl and with low Reynolds number effects. The realizable k-ϵ method usually has the best performance of the k-ϵ models for separated flows and flows with complex secondary flow features. Unfortunately, k-ϵ's prediction of spreading axisymmetric jets is poor so this method was not considered a valid solution method for this project (Theory guide).

The k-ω method has several advantages over the ϵ dissipation equation. Its formation is less sensitive to y+ values. The standard k-ω method is not highly recommended for calculations since it can be sensitive to flow variations outside the wall shear layer (User's guide). The SST method uses a hybrid approach. It uses the k-ω method in the near wall region where y+ values are important, but uses the k-ϵ method in the far field region to help with the sensitivity in the k-ω method. The k-ω method is better for low Reynolds number simulations, compressibility, and shear flow spreading (Theory Guide).

The k and ω equations for the SST model are:

$$\frac{\partial}{\partial t}(\rho k) + \frac{\partial}{\partial x_i}(\rho k u_i) = \frac{\partial}{\partial x_j}\left(\Gamma_k \frac{\partial k}{\partial x_j}\right) + \widetilde{G}_k - Y_k + S_k \tag{18}$$

$$\frac{\partial}{\partial t}(\rho \omega) + \frac{\partial}{\partial x_i}(\rho \omega u_i) = \frac{\partial}{\partial x_j}\left(\Gamma_\omega \frac{\partial \omega}{\partial x_j}\right) + G_\omega - Y_\omega + D_\omega + S_\omega \tag{19}$$

Where $\widetilde{G}_k$ Gk is the generation of turbulent kinetic energy due to mean velocity gradients, G_ω is the generation of ω, Γ_k and Γ_ω are the effective diffusivity of k and ω, respectively, Y_k and Y_ω are the dissipations of k and ω due to turbulence, D_ω is the cross-diffusion term and S_k and S_ω are defined source terms.

The SST k-ω turbulence closure was employed to calculate the Reynolds stress. The SIMPLE method was used for the pressure calculation and second order upwind discretization was used for the convective terms. The viscous terms are represented with a second-order scheme in FLUENT. Using a personal laptop with a CORE i7 2.2 GHz processor and 6 GB of RAM, the FLUENT model converged after approximately 2 hours with residuals less than 5 x 10^{-5}.

4.2 MODEL GEOMETRY AND MESHING

The shape of the scour hole, both for narrow, strongly deflected curves and for wide, weakly deflected curves can be well represented by a sine curve (Mazurek, 2001). For each combination of scour depth and radius to depth ratio, a sine curve was created to define the boundary of the scour hole. The equation of the scour hole is

$$\epsilon = -\epsilon_{max} \sin\left(\frac{\pi}{2} \frac{r}{r_{max}} + \frac{\pi}{2}\right) \tag{20}$$

Where,

ϵ = depth of scour hole measured from the flat plate soil boundary

r = radius of the scour hole

$r_{max} = \epsilon_{max} R$

R = ratio of r_{max} to ϵ_{max}

The assumed sine curve scour hole boundary based on Mazurek (2001) produced a sharp edge where the scour hole met up with undisturbed soil. The code generating the sine curve boundary was slightly to allow for a smooth transition between the scour hole and the undisturbed soil outside the hole.

At one-tenth of the depth from the top of the hole, the sine curve was replaced by an arc of a circle. The slope at the start and end of the circle arc was forced to match the slopes in the hole and at the undisturbed surface to ensure no sharp corner or edges in the model boundary. An example of the smoothed boundary is shown in Figure 4-1.
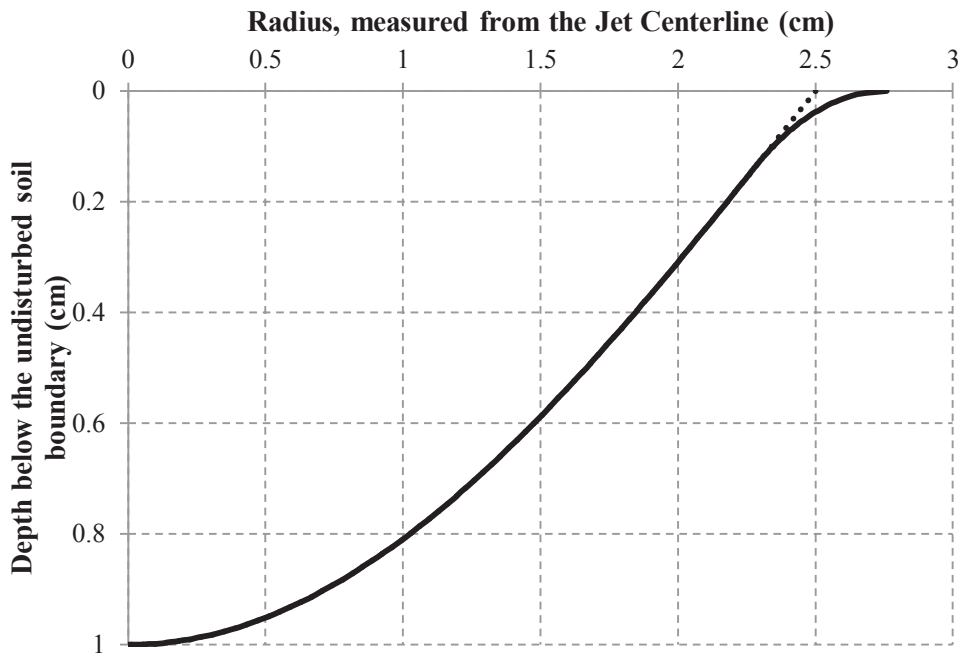
Figure 4-1 Smoothed Scour Hole Boundary

Geometries of the combinations of chosen depths and aspect ratios were meshed as 2-dimensional axisymmetric planes. In order to get accurate measures at the wall, the mesh was refined at the edges to allow for low y+ values, less than 5, in order to be within the viscous sublayer. The mesh was an unstructured, quadrilateral with approximately 64,000 elements. The mesh was imported in FLUENT to solve the Reynolds averaged Navier Stokes equation. The centerline of the jet served as the axis of symmetry. The basic geometry of a scour hole model is shown in Figure 4-2 along with an example of the mesh within the scour hole.
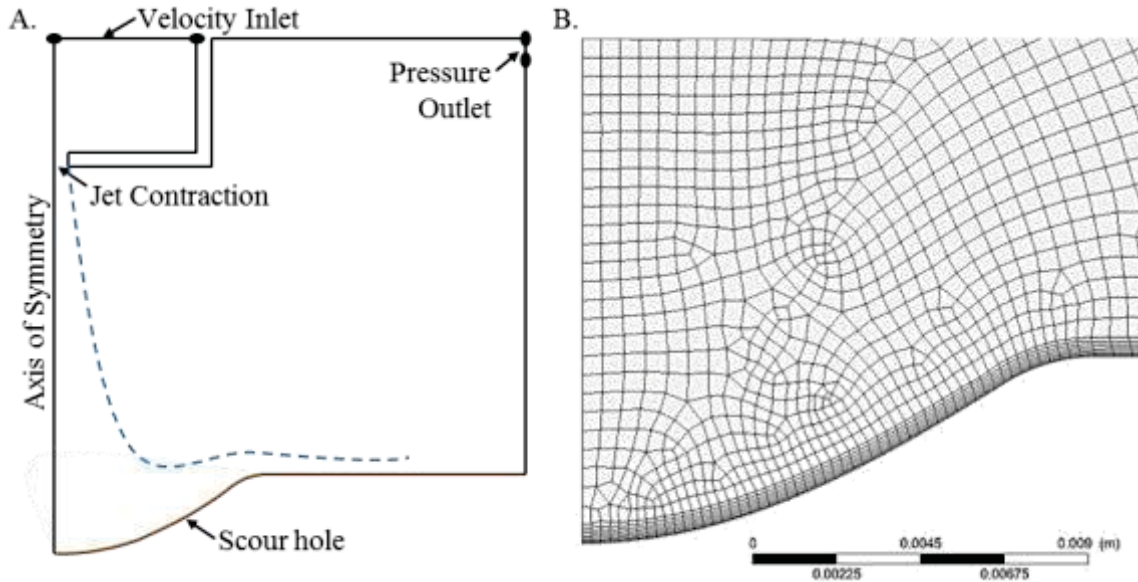
Figure 4-2 A) Schematic of Jet Test Model Geometry B) Mesh within the Scour hole

The sensitivity of the model to the density of the mesh was tested by halving the number of cells in the mesh. The model was fairly resilient to changes in the mesh density. The jet velocity profile and the wall jet velocity profiles are show in Figure 4-3. The velocity profile within the free jet was similar in terms of the maximum and the shape of the profile. The wall velocity profiles are also similar with small differences, less than 10%.
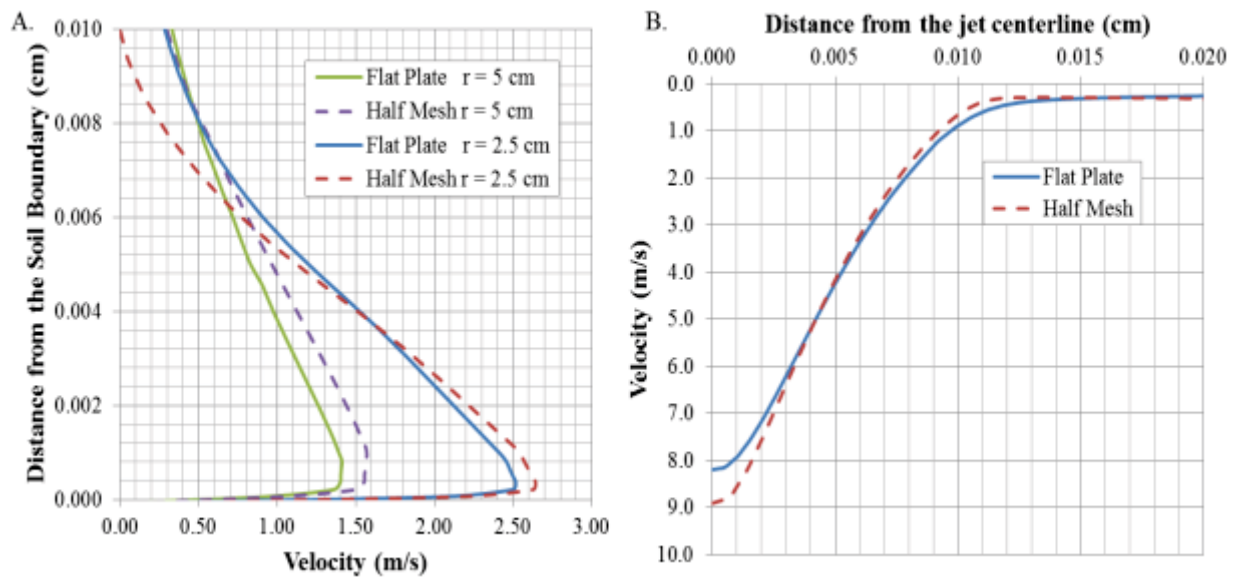
Figure 4-3 Comparison of flat plate models with different mesh densities a) wall jet velocity profiles at radial distances of 2.5 cm and 5 cm, b) free jet profile at 5 cm from the jet nozzle

4.3 BOUNDARY CONDITIONS

4.3.1   Velocity Inlet

In the Fluent Model, the velocity inlet is defined as a cross section of the Jet tube. The profile was assumed to be fully developed in the jet tube. A separate FLUENT model was used to solve the fully developed profile. A section of the jet tube was meshed as a 2d axisymmetric pipe with periodic boundary conditions. The periodic boundary conditions forced the inlet and outlet profiles to be identical. When the solution converges, the inlet velocity profile is fully developed. The magnitude of the profile was controlled by the mass flux entering the jet tube. This mass flux was determined by assuming an average jet velocity leaving the nozzle. Jet velocities in the Lower Roanoke jet tests and in Mazurek's (2001) laboratory jet tests ranged from approximate 5 to 11 m/s. A value in this range, 10 m/s, was chosen for use in the numerical model.

4.3.2   Pressure Outlet

The outlet was placed at the top of the outer wall of the submergence tank as seen in Figure 4-2. The pressure is atmospheric at the boundary allowing water to overflow the submergence tank. Because of the axisymmetric conditions in the model, the outlet acts as a weir. The actual outlet on the jet test is a tube attached to the submergence tanks. The effect of this change on the scour hole region is expected to be minimal due to the distance from the jet impingement zone and the small magnitude of the velocities found close to the outlets.

4.3.3   Walls

The jet test calculation procedures were developed based on experiments using jets impinging flat, smooth plates. The model was tested as to the sensitivity of the results to the boundary roughness. The flat plate model was adjusted so that the soil boundary had a roughness height of 0.4 mm. The boundary roughness had very little effect on the velocity profile within the free jet as seen in Figure 4-4b. The smooth wall maximum velocity was 8.1 m/s and the rough boundary model had a maximum velocity of 7.8 m/s at a distance of 5 cm from the jet nozzle. The wall jet profiles in Figure 4-4a showed that the increased boundary roughness slowed the velocity considerably. The difference between the smooth and rough models increased with the distance from the centerline. At a radius of 2.5 cm, the difference between the maximum

velocities of the smooth and rough plate was 0.34 m/s. At 5 cm, the difference increased to 0.52 m/s. The effect of this decrease was seen in the stress values. The maximum shear stress in the rough boundary case was 85% of the maximum shear stress in the smooth plate model. While the shape of the shear stress distribution was the same, the values were less than the smooth wall model. In subsequent models, the walls are assumed to be smooth in order to isolate the effect of the scour hole shape.
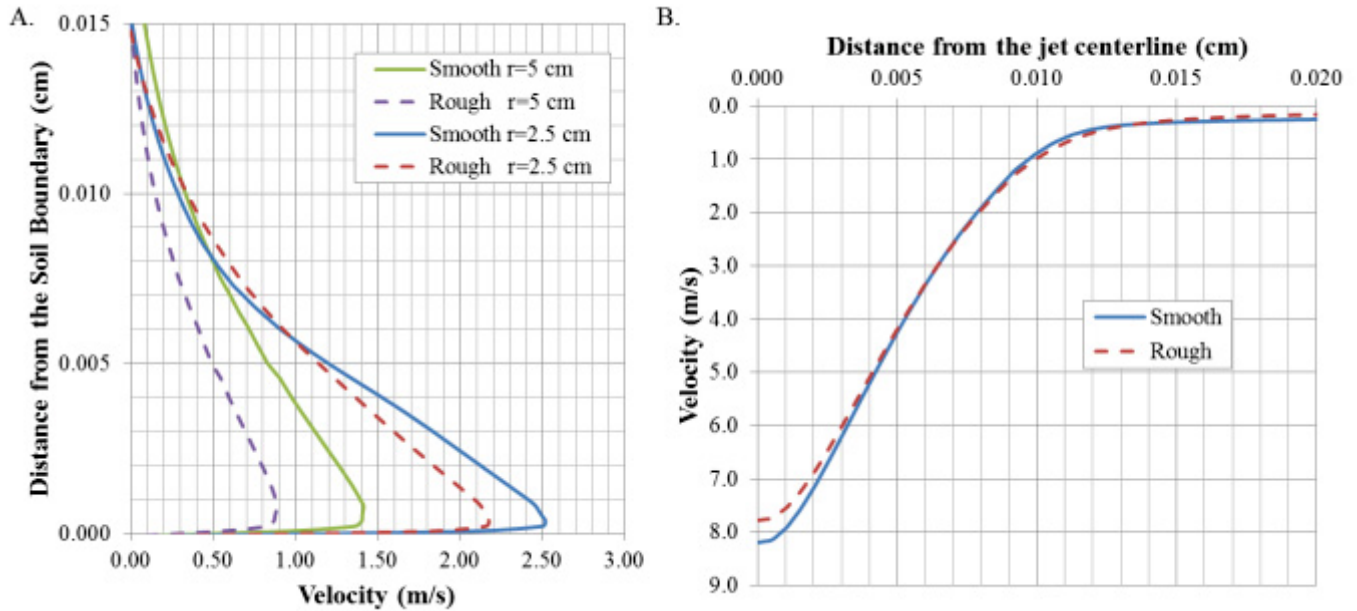
Figure 4-4 Comparison of Smooth and Rough flat plate models a) wall jet velocity profiles at radial distances of 2.5 cm and 5 cm, b) free jet profile at 5 cm from the jet nozzle

4.4 OVERVIEW OF MODELING CASES

The impinging jet is defined by the flowrate and the net nozzle diameter. A jet of consistent strength was used in each model to isolate the reaction of the jet to the change in scour hole geometry. The flat plate model serves as a baseline for all subsequent scour hole models. The effect of the jet on the flat plate was validated by experimental data.

The wall jet velocity profile is important in determining the resultant shear stress on the soil boundary. A summary of experimental studies on wall jet velocity profiles is provided in Table 4-1. The data was recording using several techniques, including particle image velocimetry (PIV), laser Doppler anemometry (LDA), and hot wire anemometry, on either air or water jets.

Table 4-1 Summary of Wall Jet Studies

Authors	Year	Measurement Technique	Fluid	r/d range
Cooper et. al	1993	Hot Wire	Air	1 to 3
Fairweather and Hargrave	2002	PIV	Air	10
Poreh, Tsuei, and Cermak	1967	Hot Wire	Air	1 to 2.75
Looney and Walsh	1984	Hot Wire	Air	> 30
Yoshida, Suenaga, and Echigo	1990	LDA	Air	1 to 4
Hargrave et. al	2006	PIV	Water	0.5 to 1

Figure 4-5 shows the velocity profile of a wall jet created by an axisymmetric jet impinging on a flat plate. The solid lines show model outputs for the flat plate case. The data points represent experimental data from past studies. The velocity profile of the wall jet collapses for all radii when normalized by the maximum velocity. The height measured from the solid boundary is normalized by δ, the location of the half maximum velocity. The model data matches fairly well with the experimental data, especially with the data from Looney and Walsh. Using the wall jet profile to compute the wall shear stress is valid because of the correlation to the experimental data. (Dianat 1996, Fairweather 2002, Yoshida 1990, Poreh 1967, Looney 1984, Hargrave 2006)
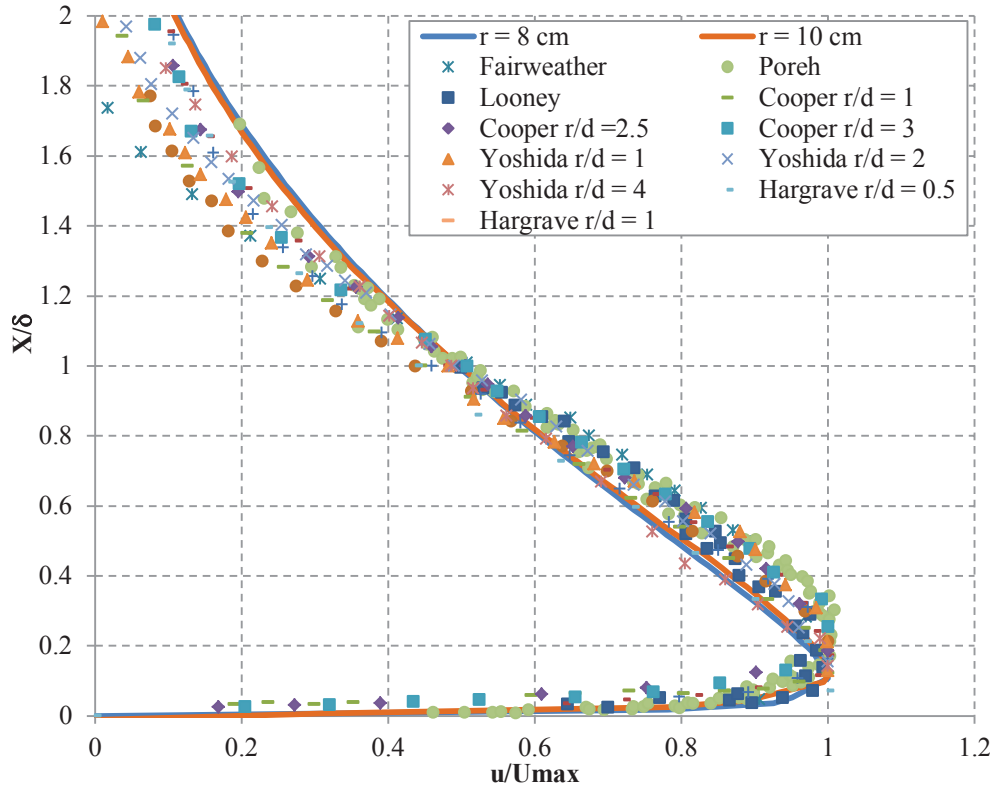
Figure 4-5 Comparison of the numerical model wall jet velocity profile to previous studies

The distribution of the shear stress on the soil boundary is important to consider in estimating erosion due to the impinging jet. The shear stress distribution was well defined by Beltaos and Rajaratnam (1976). The study used a Preston tube to measure the wall shear stress created by an air jet on a flat plate. The experiment found shear stress profiles for three values of H/d, where H is the impingement height and d is the nozzle diameter. Beltaos's experiments were completed at H/d ratios of 18.0, 21.2 and 65.7. The wall shear measured radially out from the jet centerline fell along a single curve when nondimensionalized by the maximum wall shear and the impingement height. Rajaratnam (1976) also fit a curve to the data emphasizing the experimental data close to the jet centerline. The H/d ratio of the numerical model was 15.6. The numerical model agrees fairly well with the plotted experimental data both near the jet centerline and farther away. Near the jet, Rajaratnam's curve has a slightly better fit to the data, but overall the model captures all the data in the distribution better. The numerical model does suggest that the max shear would occur slightly closer to the centerline. Rajaratnam's study found that the max would occur at r/H = 0.14, but the maximum shear stress in the numerical model occurred at r/H = 0.12. Given the accuracy of the distribution of the shear stress and the wall jet velocity

profiles, the model was determined to well represent the jet impinging on a flat plate. The next step is to compare the flat plate case to the results from models of scour holes of differing sizes.
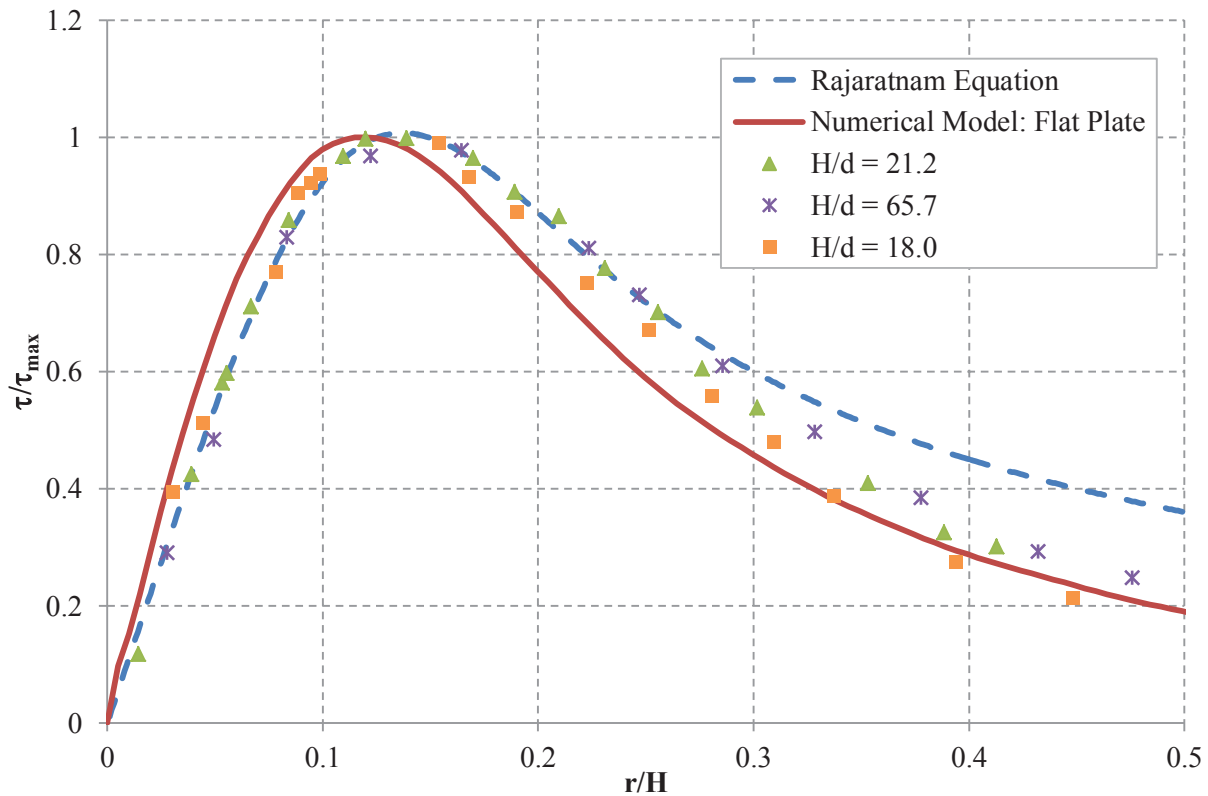
Figure 4-6 Comparison of Model Results to Previous Studies

The scour hole shapes used in this study were determined by selecting possible depth of erosion from results in the lower Roanoke River study and possible aspect ratios seen in the laboratory experiments completed by Mazurek (2001). The depths chosen were 0.5 cm, 1 cm, 2.5 cm, and 5 cm. The aspect ratios used were 0.5, 1, 2.5 and 5. The parameters for the 16 models defined by these depths and aspect ratios are seen in Table 4-2. There is no model for a depth of 5 cm and an aspect ratio of 5 since the radius of the scour hole (r = 25 cm) would exceed the diameter of the jet submergence tank.

Table 4-2 Summary of Numerical Model Parameters

Model	Depth, ε (cm)	H (cm)	d (cm)	U (m/s)	Radius, r (cm)	Ratio, R=ε/r
U10_H10_R0_E0	0	10.0	0.64	10.0	Flat Plate	
U10_H10_R05_E05	0.5	10.0	0.64	10.0	0.25	0.5
U10_H10_R1_E05	0.5	10.0	0.64	10.0	0.50	1.0
U10_H10_R25_E05	0.5	10.0	0.64	10.0	1.25	2.5
U10_H10_R5_E05	0.5	10.0	0.64	10.0	2.50	5.0
U10_H10_R05_E1	1.0	10.0	0.64	10.0	0.50	0.5
U10_H10_R1_E1	1.0	10.0	0.64	10.0	1.00	1.0
U10_H10_R25_E1	1.0	10.0	0.64	10.0	2.50	2.5
U10_H10_R5_E1	1.0	10.0	0.64	10.0	5.00	5.0
U10_H10_R05_E25	2.5	10.0	0.64	10.0	1.25	0.5
U10_H10_R1_E25	2.5	10.0	0.64	10.0	2.50	1.0
U10_H10_R25_E25	2.5	10.0	0.64	10.0	6.25	2.5
U10_H10_R5_E25	2.5	10.0	0.64	10.0	12.50	5.0
U10_H10_R05_E5	5.0	10.0	0.64	10.0	2.50	0.5
U10_H10_R1_E5	5.0	10.0	0.64	10.0	5.00	1.0
U10_H10_R25_E5	5.0	10.0	0.64	10.0	12.50	2.5

5. EFFECT OF GEOMETRY CHANGES ON THE FLAT PLATE MODEL

5.1 MAXIMUM SHEAR STRESS ON THE SOIL BOUNDARY

One of the most important assumptions in the Jet Erosion Test calculation is the flat plate assumption. Testing this assumption requires a comparison of model results from the flat plate case to each of the modeled scour hole shapes. Table 5-1 shows the results of all models and how each differs from the flat plate case. The deviations from the flat plate, which has a zero depth of scour, are greater as the scour holes grew deeper. The deviation is calculated as the difference between the two values divided by the flat plate value. The maximum applied shear stress on the soil boundary generally decreased as depths increased. The two smallest scour holes are an exception to this rule. Both small holes actually saw higher maximum shear stress values and higher normal stresses at the jet centerline.

Table 5-1 Values and Locations of Maximum Applied Shear Stress

Depth, ε (cm)	Radius, r (cm)	Ratio, r/ϵ	Max Shear	Deviation from Flat Plate	Distance to Max Shear	Deviation from Flat Plate
0	0.00	0.0	100.65	0%	0.120	0%
0.5	0.25	0.5	107.58	3%	0.120	2%
0.5	0.50	1.0	110.47	5%	0.120	2%
0.5	1.25	2.5	80.96	10%	0.158	13%
0.5	2.50	5.0	95.94	2%	0.151	10%
1	0.50	0.5	93.81	3%	0.130	1%
1	1.00	1.0	93.13	4%	0.150	7%
1	2.50	2.5	75.31	13%	0.179	18%
1	5.00	5.0	82.61	9%	0.136	2%
2.5	1.25	0.5	59.36	21%	0.190	13%
2.5	2.50	1.0	48.60	26%	0.224	25%
2.5	6.25	2.5	63.74	18%	0.170	7%
2.5	12.50	5.0	60.53	20%	0.157	3%
5	2.50	0.5	34.79	34%	0.246	15%
5	5.00	1.0	35.85	32%	0.272	26%
5	12.50	2.5	42.16	29%	0.202	6%

By only measuring the centerline depth, this assumes that the length of the jet is the only factor that affects the applied shear stress and neglects any other component of the scour hole geometry. The model data showed that the applied maximum shear stress did decrease as the

33

distance from the jet origin increased. Figure 5-1 shows the decreasing trend. Plotting the shear stress against the radius of the scour hole or the radius to depth ratio did not yield any significant correlation.
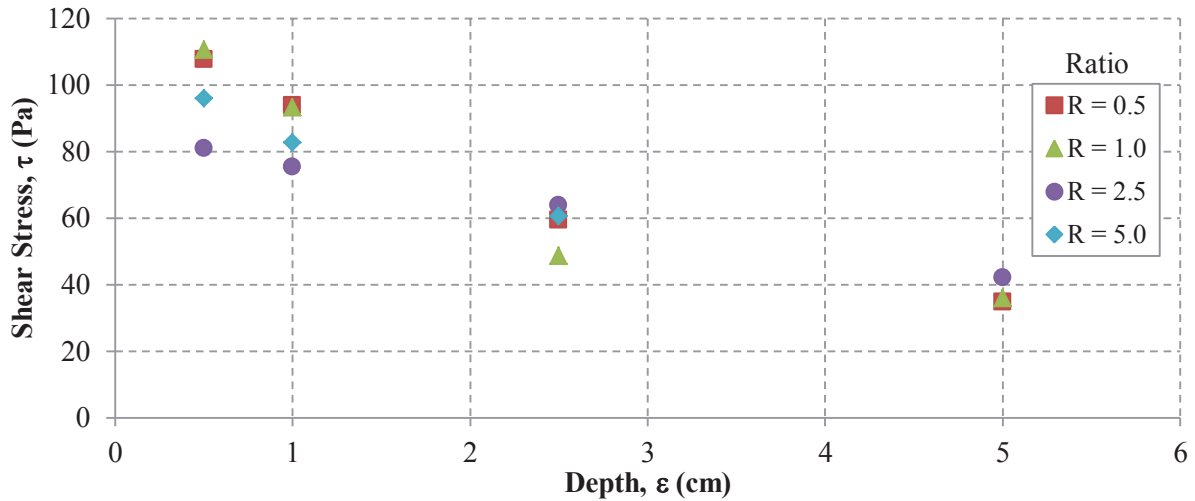
Figure 5-1 Effect of the scour depth on the maximum applied shear stress

The depth of the scour hole, or the distance from the jet nozzle to the surface, is the best indicator of the resulting maximum shear stress. However, the effect of the scour hole shape may not be as apparent in the maximum shear stress values due to the location of the maximum occurring away from the jet centerline.

The effect of the scour hole shape is more likely to be apparent in the distribution of the shear stress. Figure 5-2 shows the shear stress acting on the boundary for four different cases. The three scour holes all have same radii, but different depths. As a scour hole develops, the soil boundary would start at the flat plate case and then reach the other cases as the eroded depth increases over time. As expected from the other depth versus shear stress graphs, the shear stress decreases with increasing depth. Also, the location of the maximum shear stress moves farther from the jet centerline as the scour hole develops.
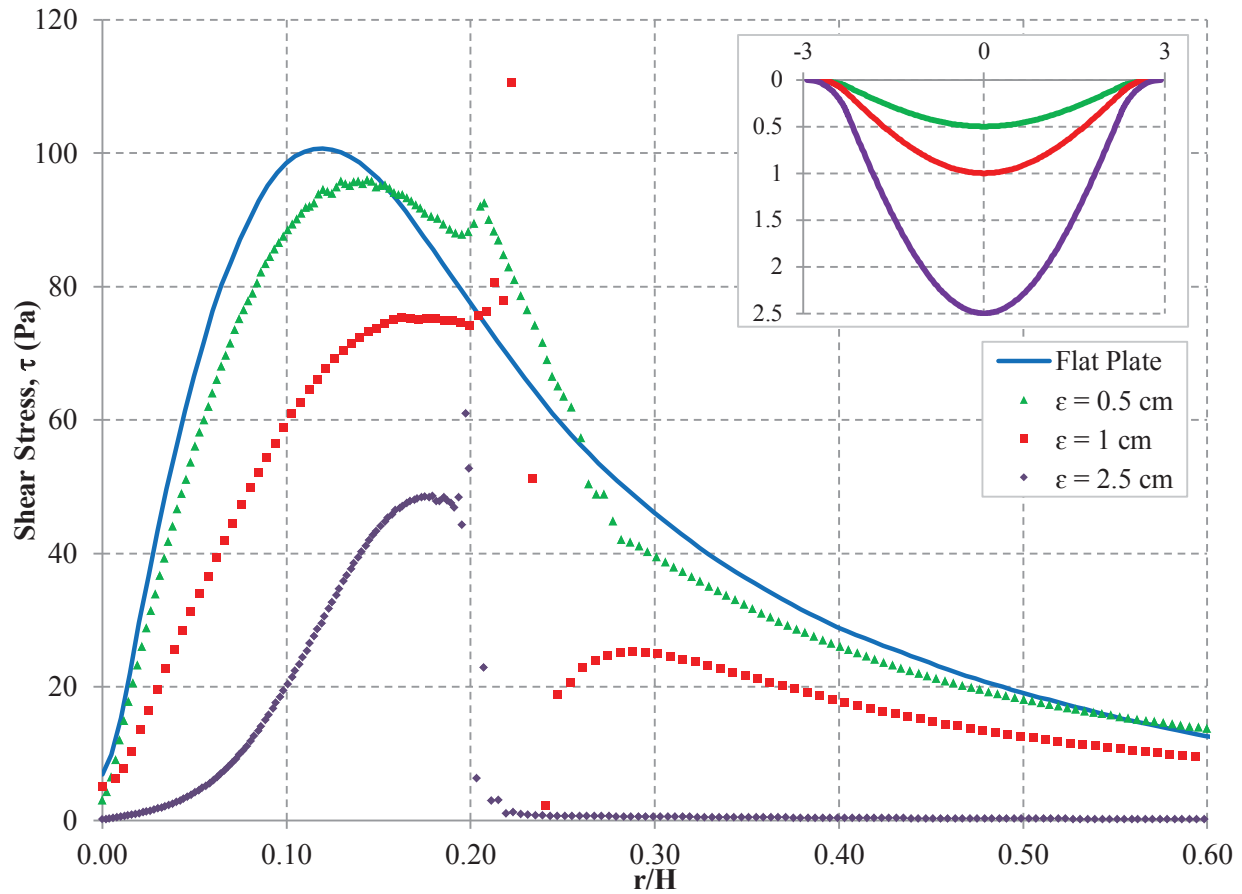
Figure 5-2 Shear stress distributions of a deepening scour hole

5.2 COMPARING NARROW AND WIDE HOLES

The numerical models showed agreement with the findings seen in previous studies. The velocity fields in a narrow hole are very different than a wide hole. The model confirmed the reversal of the jet in narrow, deep holes as seen by Mazurek. Figure 5-3 shows the vector plots of a section of three models: the flat plate case, a narrow scour hole (aspect ratio of 0.5) and a wide scour hole (aspect ratio of 5). In the narrow hole, the jet dissipated almost immediately after entering the scour hole. Most of the jet flow does not enter the hole but is deflected outside of the scour hole region. This flow pattern results in low boundary shear stress values within the scour hole itself. The normalized vector plot shows that small eddies form within the narrow hole causing energy to dissipate within the hole. Scour holes with larger aspect ratios showed less

eddy behavior. The wide hole flow field is similar to the flat plate case. While the jet flow is reversed, the flow still enters the hole and travels along the boundary.

Figure 5-3 Velocity Fields of an impinging jet on a A) Flat Plate, B) Wide Hole (depth = 1 cm, radius = 5 cm), and C) a Narrow Hole (depth = 1 cm, radius = 0.5 cm) Inset: Detail of the velocity field showing velocity contours and vectors within a Narrow Hole. D) Magnitude vectors, E) Normalized vectors
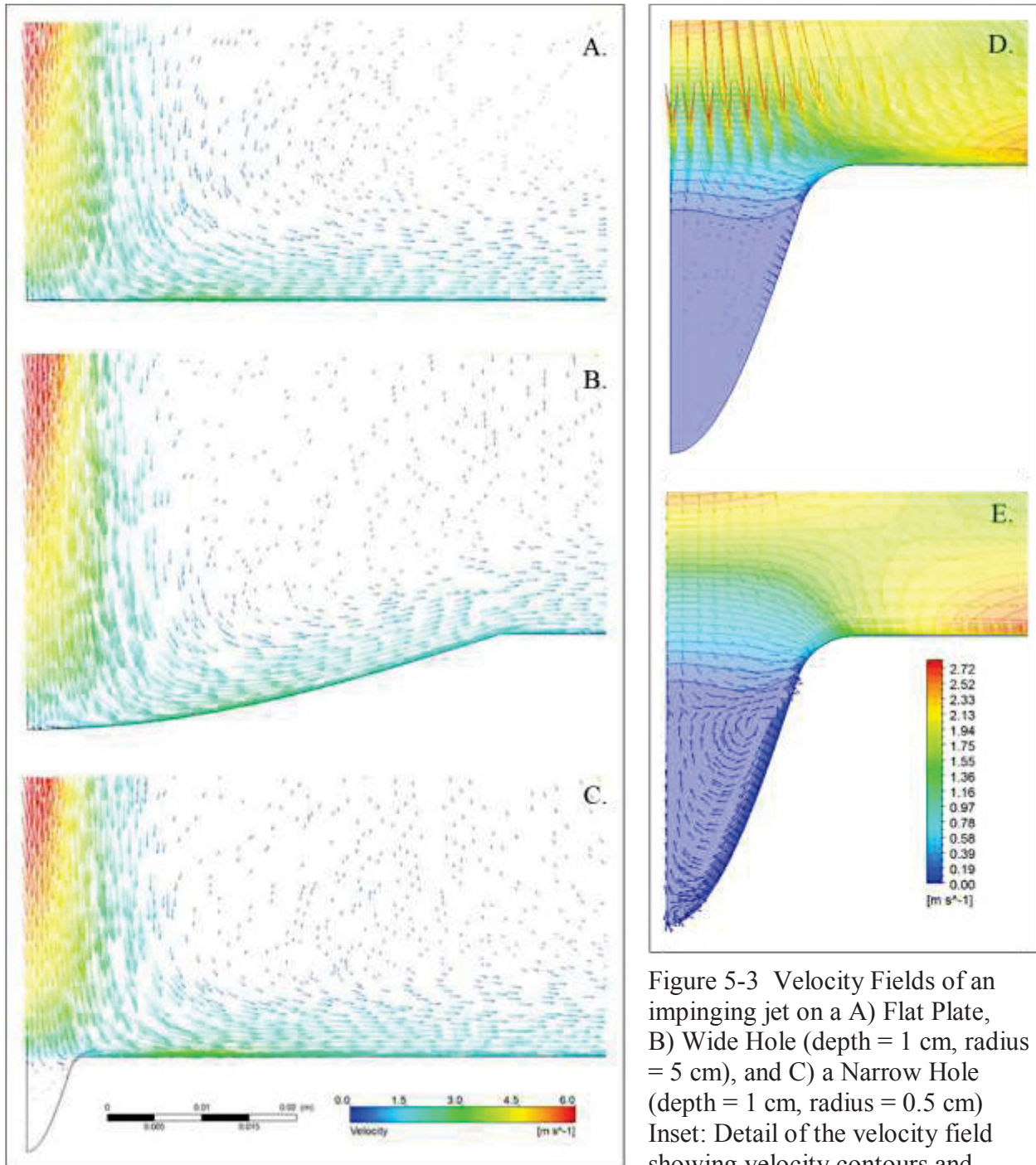
5.2.1 Narrow Scour holes

The reverse and stagnation flows within a narrow scour hole have the greatest effect on the local scour conditions. Figure 5-4 shows the boundary shear stress distribution and the normal pressure on the boundary for the two smallest scour holes modeled. Both holes have small depths, $\epsilon = 0.5$ cm. The first model has a scour hole radius of 0.25 cm and the second model has a radius of 0.5 cm. The models have aspect ratios of 0.5 and 1, respectively. In both small holes, the normal pressure is "cut" off inside the scour hole. Correspondingly, the shear stress within the scour hole is almost zero. Beyond the scour hole, the shear stress distribution begins to follow a similar pattern to the flat plate data. This result makes sense considering Mazurek's conclusions. Mazurek found that narrow holes had much smaller volumes than their wide counterparts. The stagnation flow seen within the narrow hole models yield lower applied shear stresses on the soil boundary. The lower applied shear stresses would be less likely to continue to erode soil from within the scour hole resulting in smaller volume holes.
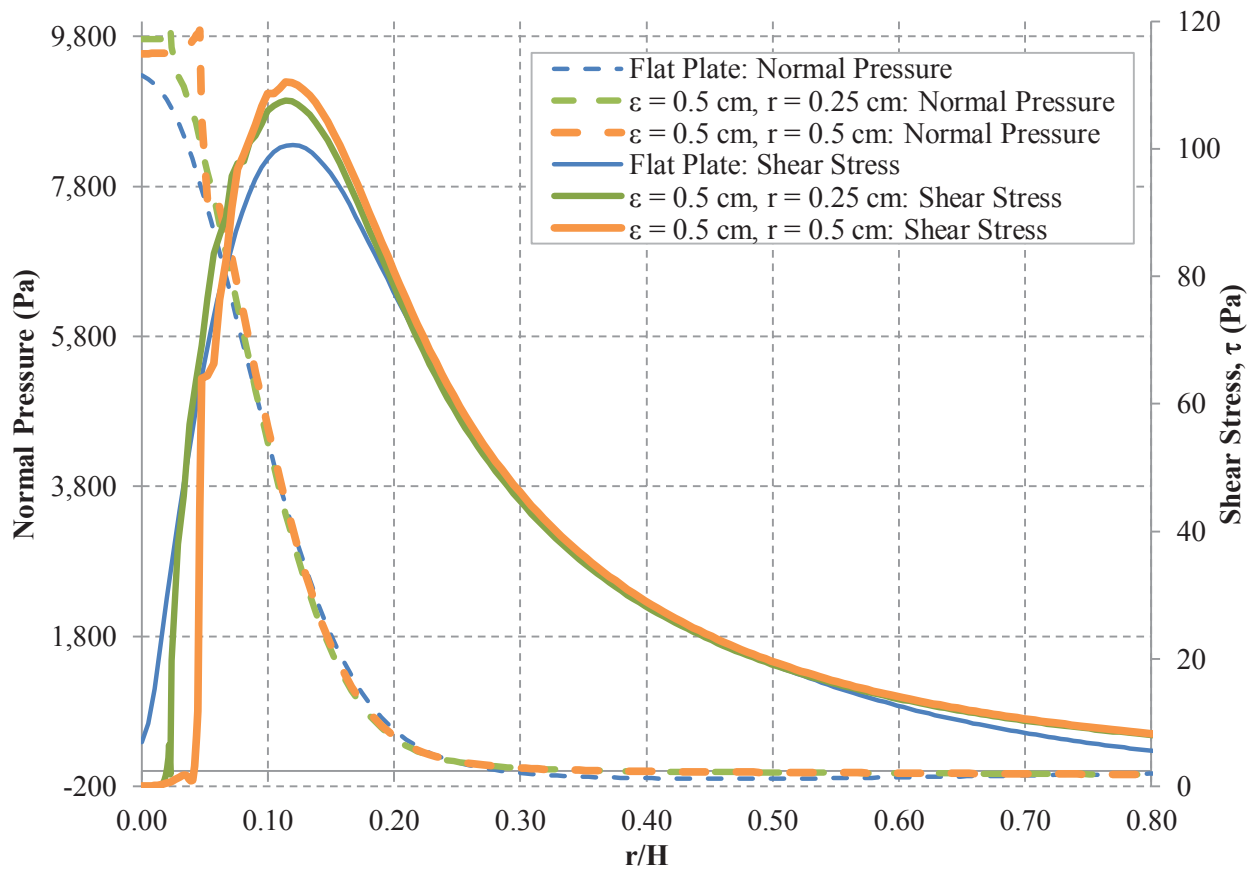
Figure 5-4 Normal pressure and shear stress distributions in small scour holes. Broken lines show the distribution of normal pressure and solid lines show the shear stress distributions.

This trend of zero velocities and shear stresses within narrow holes was seen in all models with a 0.5 depth to radius ratio as shown in Figure 5-5. The r/H location for each scour hole is marked, showing that the shear stress increases drastically as the location nears the edge of the scour hole. The location of the maximum shear moves farther from the jet centerline as the edge of the scour hole moves farther away. The method for calculating the critical shear stress uses the maximum applied shear stress based on the depth of the scour hole. Use of the maximum shear stress assumes that it is applicable to the conditions at the jet centerline. Therefore, in narrow scour holes, where the shear is zero within the hole and the maximum acts farther from the centerline, the assumption that the theoretical velocity at the new depth can be used to find the shear stress acting on the boundary is not valid. As the aspect ratio increased, the smaller volume holes continued to behave as narrow holes, with decreased shear stress values in the scour hole but larger volume holes started to act as wide holes. Beyond an aspect ratio of 2, all scour holes began to behave as wide holes.
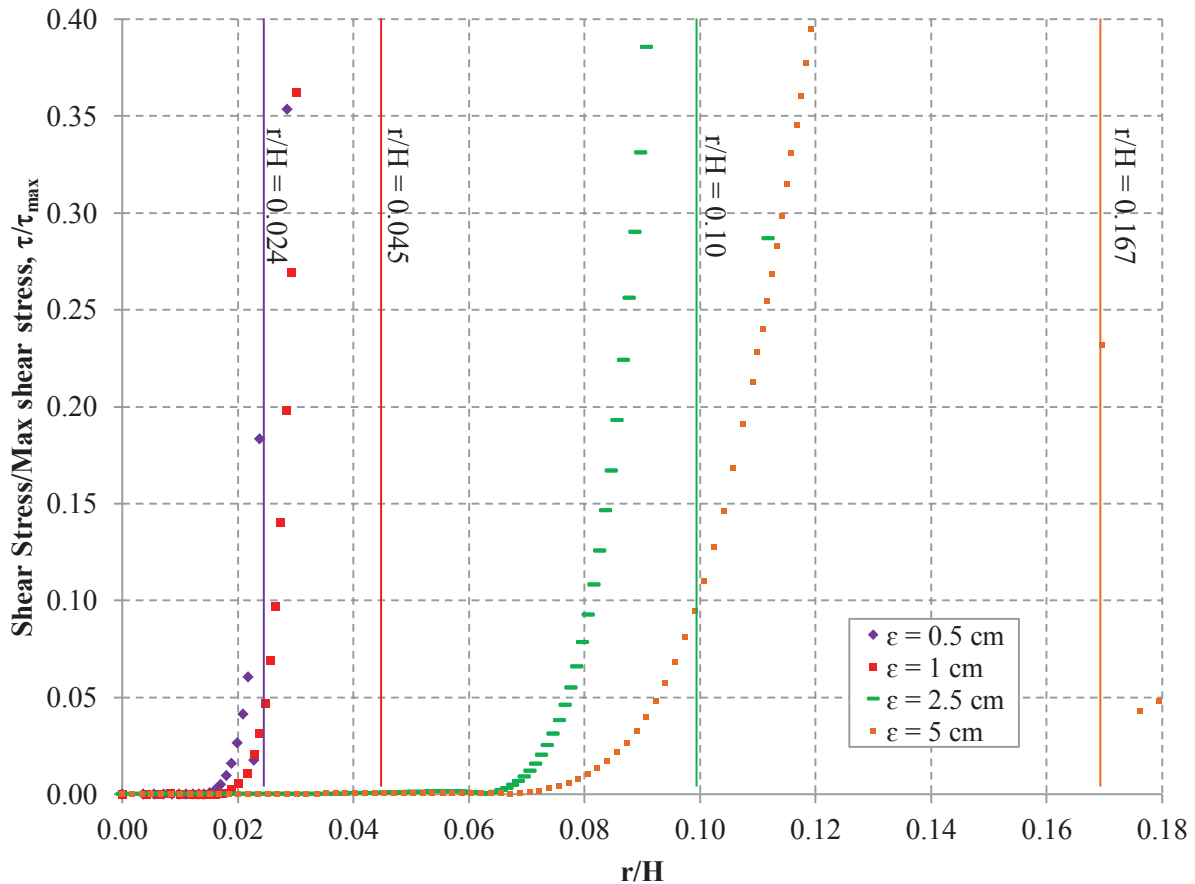

Figure 5-5 Boundary shear stress within narrow scour holes

5.2.2 Wide Shallow Holes

Wider scour holes behave differently than narrow holes. Scour holes with aspect ratios larger than 2 exhibited velocity vector fields similar to the flat plate case. Figure 5-6 shows the shear stress and normal pressure distributions for two wide scour holes. Both scour holes have 12.5 cm radii. The first scour hole has a depth of 5 cm and the second has a depth of 2.5 cm. The two scour holes have aspect ratios of R= 2.5 and R= 5 cm, respectively. The location of the maximum shear stress is consistent with the flat plate case. Also, the shear stress distribution shows little evidence of the effect of the scour hole. Unlike the narrow holes, the profile of both the shear stress and the normal pressure is consistent with the flat plate case. The maximum values are very different in magnitude. The flat plate maximum shear stress is 100 Pa, the maximum in the 2.5 cm hole was 60.5 Pa and the maximum in the 5 cm deep hole was 42.16.
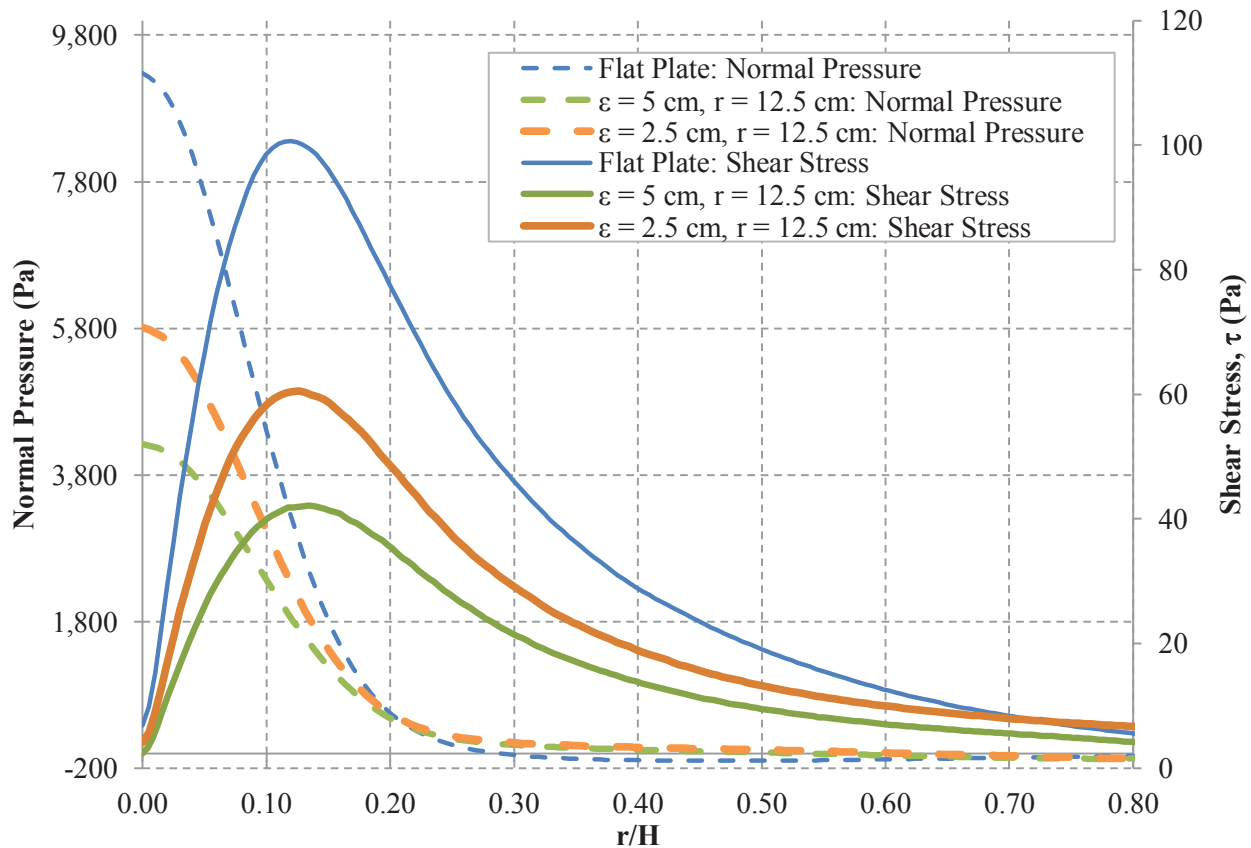

Figure 5-6 Normal pressure and shear stress distributions in wide holes. Broken lines show the distribution of normal pressure and solid lines show the shear stress distributions.

Despite these magnitude differences, the nondimensional shear stress profiles all fall on the same line as show in Figure 5-7. The profiles were nondimensionalized by dividing the shear

stress and the normal pressure by the respective maximum values for each model. The dimensional shear stress profile confirms that the depth of the scour hole and thus the distance from the jet nozzle controls the magnitude of the wall shear stress. The nondimensional profile confirms that the applied shear stress in wide holes is well represented by the flat plate case. The similarities between wide scour holes and the flat plate case show that using results of jet tests from wide scour holes better represent the assumptions used to determine the erodibility of the channel.
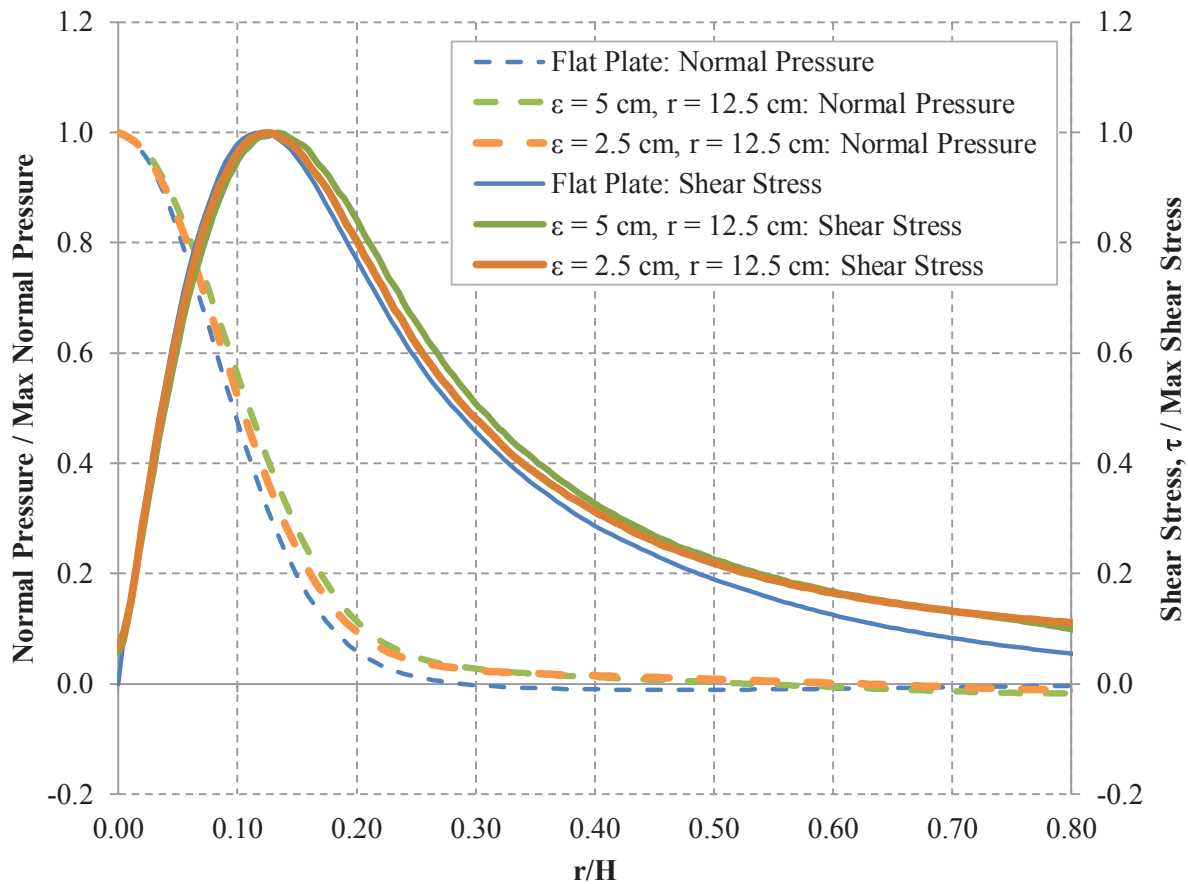
Figure 5-7 Nondimensional normal pressure and shear stress distributions in wide holes. Broken lines show the distribution of normal pressure and solid lines show the shear stress distributions.

5.3 IMPACT ON JET TEST CALCULATIONS

To build a model associated with time steps, imput data from a wide scour hole was used from Mazurek (2001). The model was run at each recorded time step using the specified flowrate, nozzle diameter, and scour hole radius and depth. The scour hole shape was defined using the same sine equation specified earlier. While most field tests only record data for

approximately one hour, Mazurek ran lab jet tests until the jet-soil setup reached an equilibrium state. Throughout the chosen test, the aspect ratio of the scour hole varied from 5 to 2.5, the equilibrium scour hole having an aspect ratio of 2.5. Figure 5-8 shows that there is an assymptotic behavior for both variables over time. Again, the depth is inversely proportional to the shear stress, so over time the applied shear stress decreases as the depth increases.
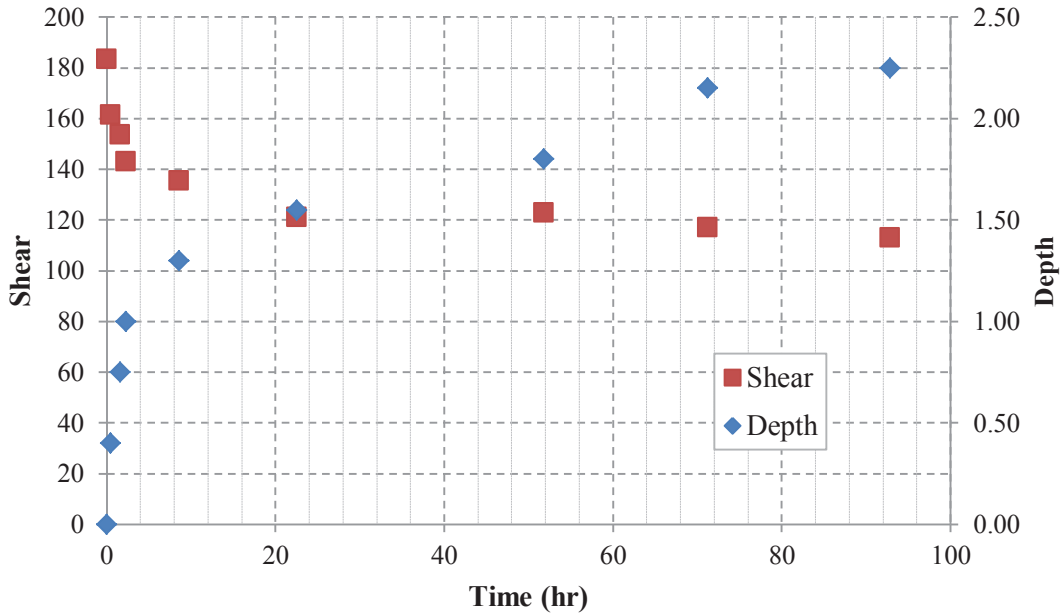
Figure 5-8 Scour hole depth and boundary shear stress over time

Table 5-2 shows the ratio of the maximum shear stress for each scour hole to the flat plate maximum shear stress. The model ratio is the shear stress from each scour hole model divided by the flat plate model shear stress. The theoretical ratio is based on equation 13 and is equal to

$$\left(\frac{H_0}{H_0+\epsilon}\right)^2 \tag{21}$$

The percent difference between the two ratios is shown as the deviation from the flat plate assumptions.

Table 5-2 Theoretical and Model Shear Stress Ratios

Depth, ε (cm)	Radius, r (cm)	Theoretical ratio	Model ratio	Deviation from Flat Plate
0	0.00	1	1	0%
0.5	0.25	0.907	1.069	16%
0.5	0.50	0.907	1.098	19%
0.5	1.25	0.907	0.804	12%
0.5	2.50	0.907	0.953	5%
1	0.50	0.826	0.932	12%
1	1.00	0.826	0.925	11%
1	2.50	0.826	0.748	10%
1	5.00	0.826	0.821	1%
2.5	1.25	0.640	0.590	8%
2.5	2.50	0.640	0.483	28%
2.5	6.25	0.640	0.633	1%
2.5	12.50	0.640	0.601	6%
5	2.50	0.444	0.346	25%
5	5.00	0.444	0.356	22%
5	12.50	0.444	0.419	6%

The error between the model ratio and the theoretical ratio ranged from 1 to 28%. For each depth, at least one model differed less than 6% from theoretical case. While there are models that match well with the theoretical ratio, the errors for some models were over 20%. The amount of deviation from the theoretical model depended more on the aspect ratio of the hole than on the depth of the hole. For each depth, the lowest error was for a wide hole case. Especially at high depth values, ϵ =2.5 and ϵ =5, the error in wide holes varied from 1% to 6%, while the narrow holes saw as much as 22% to 28% error.

In Figure 5-9, the shear stress calculated using Hansen's flat plate assumption is plotted against the maximum shear stress in each model. A summary of the maximum shear stress values shown in the figure are given in Table 5-3. The error between the two calculations is indicated by the distance from each point to the 1:1 line. The majority of the points fall below the 1:1 line, therefore the flat plate assumption tends to overestimate the applied shear stress. Narrow holes tended to be farther from the line of perfect agreement.

Table 5-3 Summary of Maximum Shear Stress from the Numerical models

Depth	Flat Plate Assumption	Aspect Ratio, R = ε/r			
		0.5	1.0	2.5	5.0
0.5	91.29	107.58	110.47	80.96	95.94
1.0	83.18	93.81	93.13	75.31	82.61
2.5	64.41	59.36	48.60	63.74	60.53
5.0	44.73	32.68	35.85	42.16	-
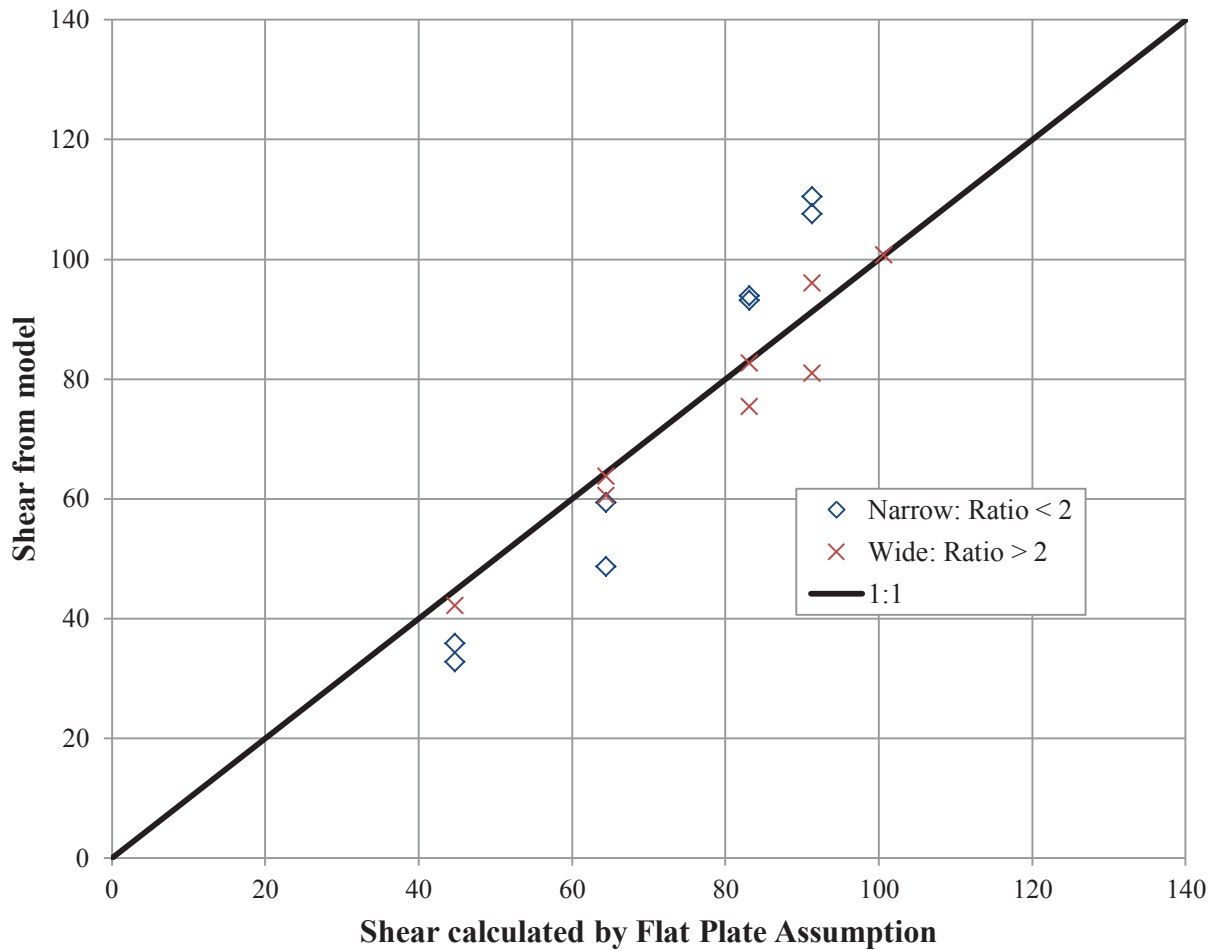
Figure 5-9 Shear stress calculated using the model and using the flat plate assumption

The deviation from the expected shear depended on the aspect ratio (radius divided by depth) of the scour hole as seen in Figure 5-10. Low ratios, or narrow holes, had a high variability in the amount of error seen between the model shear stress and the theoretical shear stress. Wide holes had smaller error values and had less variability in the error from one depth to another.

Figure 5-10 Error in shear stress based on scour hole aspect ratio

If the theoretical equation used to determine the applied shear stress is consistently overestimating the stress, the error could propagate through the calculations.

From a field test, the critical shear stress is found by extrapolating the measured depth values over time based on a hyperbolic equation. The assymptote of the hyperbolic equation is assumed to be the equilibrium depth. The applied shear stress co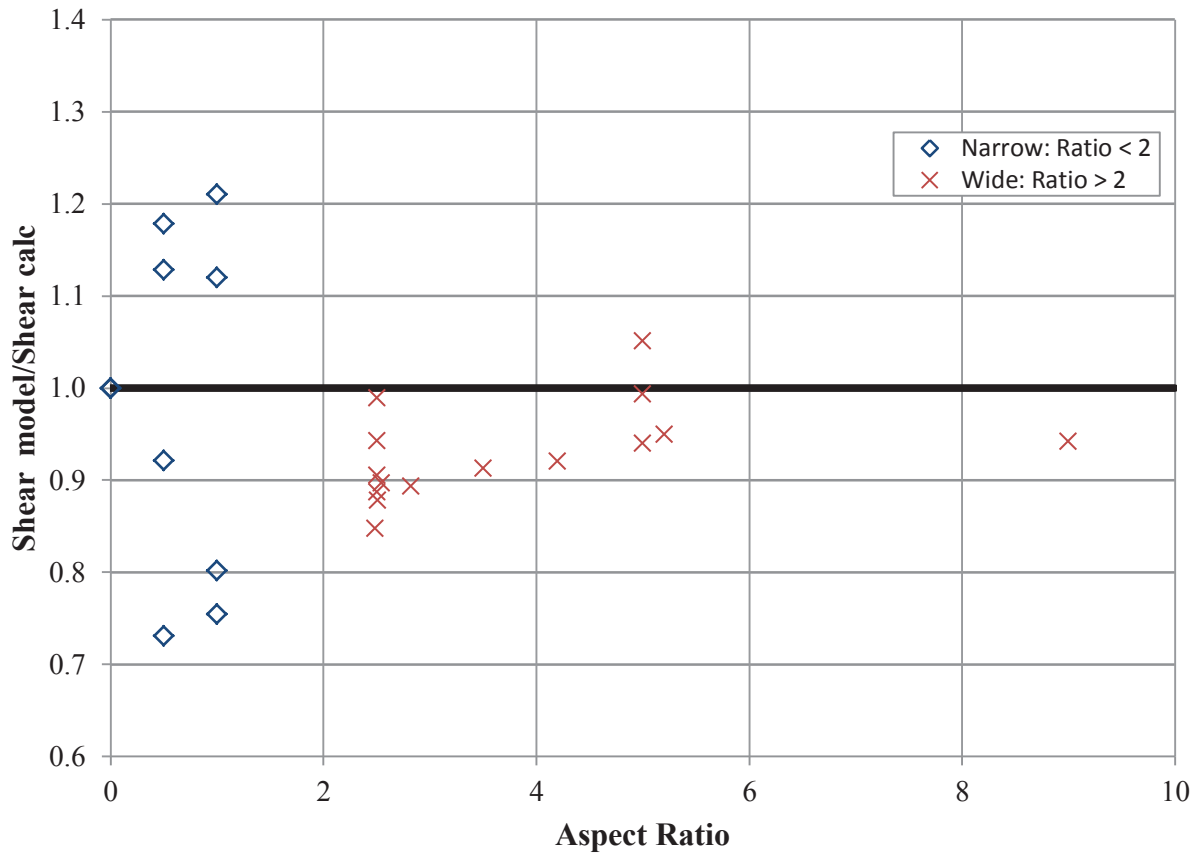rresponding to the equilibrium depth is the critical shear stress. The seond part of the excess shear equation, the coefficient of erodibility, k_d, is found by fitting the time based integral of the excess shear equation to the field data.

Many of the assumptions used in the jet test calculation are sound. The depth will eventually reach an equilibrium state. The first stage of the calculation fits a hyperbola to the depth and time data in order to find the equilibrium depth. Vector plots from wide scour holes exhibit the same conditions as a flat plate model as the depth begins to near the equilibrium depth. In narrow holes, the fluid dynamic conditions are not likely to create a change in the depth over time that would represent the erosional properties of the soil. Since the depth over time data

for a narrow hole would not represent the flat plat scenario, the results would not be valid to use in the jet test calculation for determining the critical shear stress and coefficient of erodibility. Given that the depth data is valid based on a wide hole configuration, the equilibrium depth calculation would be valid. The critical shear stress is calculated as the stress corresponding to the equilibrium depth using the equation $\tau_{o\epsilon} = \frac{H_o^2}{(H_o+\epsilon)^2} \tau_{oFP}$. The numerical models showed that the applied shear stress was usually overestimated using this equation, but that for wide scour holes the model value was within 10% of the value predicted. This 10% error value can be used to address the range for a factor of safety when calculating the potential bank erosion in a reach.

The critical shear stress is one of the parameters used to calculate the coefficient of erodibility. Error in the calculated critical shear stress will propagate through the k_d calculation. Using the equilibrium depth found in the first curve fit, a second curve fit is applied to the dimensionless depth data and a dimensionless time. The curve fit is found using the following equation, which is based on an integral of the dimensionless excess shear stress, equation 14.

The dimensional time can be written as $t_* = \frac{t}{T_r}$. The value of T_r can be found through fitting the curve to the data. The coefficient of erodibility, k_d, is found using the equation:

$$k_d = \frac{H_e}{T_r \tau_c} \tag{22}$$

Based on the above equation, the erodibility coefficient is directly related to the accuracy of the critical shear stress. Since both the equilibrium depth and the T_r value are found empirically using curve fitting, error in the critical shear stress will directly affect the coefficient of erodibility. A 10% overestimation of the critical shear stress would mean a 10% underestimation of the coefficient of erodibility.

Considering the excess shear stress equation, equation 1, the corresponding error in the two parameters would lead to underestimating the total bank erosion. For wide holes, this error would be smaller than for narrow holes. In the narrow hole case, the velocities are extremely low within the hole creating very little shear stress. Due to the low stress, it is unlikely that the erosion at the jet centerline will be indicative of the assumed shear stress from the flat plate assumption. A narrow hole, based on the applied shear stress, would erode slower than a wide hole of the same material. Small depth changes in narrow holes would cause the calculated equilibrium depth to be artificially low. Relying on data from a narrow hole, the soil would be

deemed unlikely to erode, with a high critical shear stress and a corresponding low coefficient of erodibility.

Using data from both wide and narrow scour holes could result in large variations from one test to another. This variability was seen in the tests taken on the lower Roanoke River site. Some tests resulted in high critical shear stress values while other tests in the same approximate location yielded much smaller values of critical shear stress. At Site 1, the lowest calculated critical shear stress was 1.14 Pa, but 6 of the 14 tests at Site 1 reported critical shear stress values greater than 12 Pa. The highest critical shear stress found using a jet test on the lower Roanoke River was 21.5 Pa.

The high critical shear stresses could have been the result of a narrow scour holes. The lower critical shear stress was likely the result of a wide scour hole. In addition to a wide scour hole better representing a flat plate, the lower critical shear stress is a more conservative value to use in estimating potential erosion. In order to improve the accuracy of the erosional properties found at the lower Roanoke River site, it would be necessary to run additional jet tests, noting the aspect ratio of the scour holes formed.

5.4 LIMITATIONS

The Jet Erosion Test is a site specific test. The test uses the change in depth over time to find characteristics of the soil used to estimate erosion at that site. In the field, the only parameter measured is the eroded depth. It is assumed that all the effects of parameters, such as soil structure, grain size distribution, organic matter content and many others, are combined into the rate of erosion seen in the changing scour hole depth. Since the test does not use any data to find the dependence of the erosion rate on other soil parameters, results from an individual jet erosion cannot be applied to sites with different soil properties.

The numerical model found the reaction of shear stress and normal stress distributions to different soil profiles. Previously, only flat plate cases had been studied in depth as to the stresses created by an impinging jet. The results showed the differences between the flat plate and scour hole cases, but cannot be used to determine the erosion characteristics of a soil without further modelling. Values of the stresses in the immediate vicinity of the scour hole edge were subject to error as well. The sudden change in slope found near the boundary edge created discontinuities

that can be seen in some of the shear stress plots. In most cases, these discontinuities could be minimized through the smoothing of the transition from the scour hole to the undisturbed soil.

6. CONCLUSIONS

The depth of the scour hole was the best indicator of the magnitude of the maximum shear stress acting on the soil boundary. However, the maximum shear stress does not act at the jet centerline where the scour depth measurements are taken. The flat plate model assumes that the maximum shear stress calculated based on the depth is a reasonable indicator of the erosional forces acting at the centerline. The model showed that the shear stress distribution near the jet centerline depended on the aspect ratio of the scour hole.

The shear stress in narrow holes exhibited a "cut off" behavior. Within the scour hole, the applied shear stress values wear near zero, even though outside the hole the shear stress distribution was similar to the flat plate case. The vector plots showed the velocity components within the narrow scour holes to be close to zero confirming the observed shear stress results. Low applied shear stresses will cause narrow holes to erode slowly and have small volumes. Results from narrow holes will give high critical shear stress values. The model results saw high variations between the narrow holes and the flat plate assumption.

Wide holes will produce better results in field tests. Vector plots from wide holes better resemble the flat plate case. Models of wide holes varied less than narrow holes, falling within 10% of the predicted flat plate values. Wide scour hole results should indicate lower critical shear stress values and corresponding high coefficients of erodibility. Using these erosional properties in the excess shear stress equation will yield a more conservative estimate of riverbank erosion.

To improve accuracy in the field, the aspect ratio of the scour hole should be measured. In calculating the critical shear stress and the coefficient of erodibility, only results from wide scour hole tests, tests with aspect ratios greater than 2, should be used. Jet tests resulting in narrow holes should be considered a failed test. Narrow holes are more likely to form when the jet nozzle is too close to the soil or when initial bulk failures create a deep hole at the start of a test. Minimizing these conditions would help to eliminate narrow hole results.

There is a need for future research to continue to improve the accuracy and usefulness of the jet test. More field data should be taken to introduce the use of the aspect ratio in determining

effective jet test measurements. More validation data should be found not just for the flat plate data, but for a jet impinging on a curved surface.

There is also a need for determining the effect of the duration of the test on the results. Each lower Roanoke River test was run for approximately an hour. Since this length of time is significantly less than the time to reach equilibrium, it is necessary to determine whether the outcome would change if the test were run longer.

REFERENCES

Albertson, M. L., Dai, Y. B., Jensen, R. A., and Rouse, H. (1949). "Diffusion of submerged jets." *American Society of Civil Engineers -- Proceedings*, 75(10), 1541-1548.

Arulanandan, K., Gillogley, E. and Tully, R. (1980). "Development of a quantitaive method to predict critical shear stress and rate of erosion of natural undisturbed cohesive soils." Technical Report GL-80-5. Army Corps of Engineers.

ASTM (2000)."Standard Test Method for Erodibility Determination of Soil in the Field or in the Laboratory by the Jet Index Method." Standard D5852 *ASTM International*, West Conshohocken, PA: American Society for Testing and Materials

Beltaos, S. (1974). "Turbulent impinging jets." PhD, The University of Alberta, Edmonton, Alberta.

Beltaos, S., and Rajaratnam, N. (1974). "Impinging Circular Turbulent Jets." *ASCE Journal of the Hydraulics Division*, 100(10), 1313-1328.

Beltaos, S., and Rajaratnam, N. (1977). "Impingement of Axisymmetric Developing Jets." *Journal of Hydraulic Research*, 15(4), 311-326.

Blaisdell, F. W., Anderson, C. L., and Hebaus, G. G. (1981). "Ultimate dimensions of local scour." 107(3), 327-337.

Bouchez, J., Gaillardet, J., France-Lanord, C., Maurice, L., and Dutra-Maia, P. (2011). "Grain size control of river suspended sediment geochemistry: Clues from Amazon River depth profiles." *Geochemistry Geophysics Geosystems*, 12.

Buffington, J. M. (1999). "The legend of A. F. Shields." *Journal of Hydraulic Engineering-Asce*, 125(4), 376-387.

Buffington, J. M., and Montgomery, D. R. (1997). "A systematic analysis of eight decades of incipient motion studies, with special reference to gravel-bedded rivers." *Water Resources Research*, 33(8), 1993-2029.

Charonko, C. M. (2010). "Evaluation of an in situ measurement technique for streambank critical shear stress and soil erodibility." Master of Science, University Libraries, Virginia Polytechnic Institute and State University, Blacksburg, Va.

Dianat, M., Fairweather, M., and Jones, W. P. (1996). "Predictions of axisymmetric and two-dimensional impinging turbulent jets." *International Journal of Heat and Fluid Flow*, 17(6), 530-538.

Dianat, M., Fairweather, M., and Jones, W. P. (1996). "Reynolds stress closure applied to axisymmetric, impinging turbulent jets." *Theoretical and Computational Fluid Dynamics*, 8(6), 435-447.

Diplas, P., Dancey, C. L., Celik, A. O., Valyrakis, M., Greer, K., and Akar, T. (2008). "The Role of Impulse on the Initiation of Particle Movement Under Turbulent Flow Conditions." *Science*, 322(5902), 717-720.

Dorrell, R. M., Hogg, A. J., Sumner, E. J., and Talling, P. J. (2011). "The structure of the deposit produced by sedimentation of polydisperse suspensions." *Journal of Geophysical Research-Earth Surface*, 116.

Fairweather, M., and Hargrave, G. K. (2002). "Experimental investigation of an axisymmetric, impinging turbulent jet. 1. Velocity field." *Experiments in Fluids*, 33(3), 464-471.

Hanson, G. J. (1991). "Development of a jet index to characterize erosion resistance of soils in earthen spillways." *Transactions of the American Society of Agricultural Engineers*, 34(5), 2015-2020.

Hanson, G. J., and Cook, K. R. (1997). "Development of excess shear stress parameters for circular jet testing." *Proceedings of the 1997 ASAE Annual International Meeting. Part 1 (of 3), August 10, 1997 - August 14, 1997*, ASAE, Minneapolis, MN, USA.

Hanson, G. J., and Cook, K. R. (2004). "Apparatus, test procedures, and analytical methods to measure soil erodibility in situ." *Applied Engineering in Agriculture*, 20(4), 455-462.

Hargrave, G. K., Williams, T. C., Anandarajah, K., and Halliwell, N. A. (2006). "The 3D Velocity Field of an Impacting Turbulent Jet." *Second International Conference on Optical and Laser Diagnostics*, J. o. P. C. Series, ed., Institute of Physics Publishing, 162-172.

Hollick, M. (1976). "Towards a Routine Test for the Assessment of the Critical Tractive Forces of Cohesive Soils." *Transactions of the American Society of Agricultural Engineers*, 19(Compendex), 1076-1081.

Julian, J. P., and Torres, R. (2006). *Hydraulic erosion of cohesive riverbanks*.

Looney, M. K., and Walsh, J. J. (1984). "Mean-flow and turbulent characteristics of free and impinging jet flows." *Journal of Fluid Mechanics*, 147(OCT), 397-429.

Mazurek, K. A. (2001). "Scour of clay by jets." PhD, University of Alberta, Edmonton, Alberta.

Mazurek, K. A., and Gheisi, A. R. (2009). "Assessment of the Erodibility of a Cohesive Soil using a Submerged Circular Turbulent Impinging Jet." *33rd IAHR Congress: Water Engineering for a Sustainable Environment*, International Association of Hydraulic Engineering & Research.

Mazurek, K. A., Rajaratnam, N., and Sego, D. C. (2001). "Scour of cohesive soil by submerged circular turbulent impinging jets." *Journal of Hydraulic Engineering*, 127(7), 598-606.

Mazurek, K. A., Rajaratnam, N., and Sego, D. C. (2003). "Scour of a cohesive soil by submerged plane turbulent wall jets." *Journal of Hydraulic Research*, 41(2), 195-206.

Moore, W. L., and Masch, J. F. D. (1962). "Experiments on scour resistance of cohesive sediments." *Journal of Geophysical Research*, 67(4), 1437-1449.

Mostafa, T. S., Imran, J., Chaudhry, M. H., and Kahn, I. B. (2008). "Erosion resistance of cohesive soils." *Journal of Hydraulic Research*, 46(6), 777-787.

Nam, S. (2005). "Settling and sedimentation behavior of fine-grained materials." Master of Science, University Libraries, Virginia Polytechnic Institute and State University, Blacksburg, Va.

Nam, S., Gutierrez, M., and Diplas, P. (2008). "Channeling during settling and self-weight consolidation of cohesive sediments." *Canadian Geotechnical Journal*, 45(6), 867-876.

Nam, S., Petrie, J., Diplas, P., and Gutierrez, M. (2010). "Effects of Spatial Variability on the Estimation of Erosion Rates for Cohesive Riverbanks." *International Conference on Fluvial Hydraulics (River Flow 2010)*. Braunschweig, Germany. Sept 8-10 2010.

"National Hydropower Association." <hydro.org>. (2011).

Odgaard, A. J. (1987). "Streambank Erosion Along Two Rivers in Iowa." *Water Resources Research*, 23(7), 1225-1236.

Poreh, M., and Cermak, J. E. (1959). "Flow characteristics of a circular submerged jet impinging normally on a smooth boundary." *Proceedings of the Sixth Annual Conference on Fluid Mechanics* University of Texas, Austin.

Poreh, M., Tsuei, Y. G., and Cermak, J. E. (1967). "Investigation of a Turbulent Radial Wall Jet." *Journal of Applied Mechanics*, 34(2), 457-463.

Poreh, M., Tsuei, Y. G., and Cermak, J. E. (1967). "Investigation of a Turbulent Radial Wall Jet." *Journal of Applied Mechanics*, 34(2), 457-463.

Potter, K. N., Velázquez-Garcia, J. d. J., and Torbert, H. A. (2002). "Use of a submerged jet device to determine channel erodibility coefficients of selected soils of Mexico." *Journal of Soil and Water Conservation*, 57(5), 272-277.

Rajaratnam, N. (1976). *Turbulent jets*, Elsevier Scientific Pub. Co., Amsterdam; New York.

Rajaratnam, N., and Beltaos, S. (1977). "Erosion by Impinging Circular Turbulent Jets." *ASCE Journal of the Hydraulics Division*, 103(10), 1191-1205.

Sabersky, R. H., Acosta, A. J., Hauptmann, E. D., and Gates, E. M. (1999). *Fluid Flow: A First Course in Fluid Mechanics*, Prentice-Hall, Upper Saddle River, NJ.

Sheilds, A. (1936). "Application of similarity principles and turbulence research to bed-load movement." *Hydrodynamics Laboratory Publication No. 167*, W. P. Ott, and J. C. van Uchelen, trans., U.S. Dept. of Agriculture, Soil Conservation Service Cooperative Laboratory, California Institute of Technology, Pasadena, CA.

Stein, O. R., and Nett, D. D. (1997). "Impinging jet calibration of excess shear sediment detachment parameters." *Transactions of the American Society of Agricultural Engineers*, 40(6), 1573-1580.

Sumer, B. M., Chua, L. H. C., Cheng, N. S., and Fredsoe, J. (2003). "Influence of turbulence on bed load sediment transport." *Journal of Hydraulic Engineering-Asce*, 129(8), 585-596.

Syvitski, J. P. M., Vorosmarty, C. J., Kettner, A. J., and Green, P. (2005). "Impact of humans on the flux of terrestrial sediment to the global coastal ocean." *Science*, 308(5720), 376-380.

Ternat, F., Boyer, P., Anselmet, F., and Amielh, M. (2008). "Erosion threshold of saturated natural cohesive sediments: Modeling and experiments." *Water Resources Research*, 44(W11434).

Valyrakis, M., Diplas, P., Dancey, C. L., Greer, K., and Celik, A. O. (2010). "Role of instantaneous force magnitude and duration on particle entrainment." *Journal of Geophysical Research-Earth Surface*, 115.

Williams, G. P., and Wolman, M. G. (1984). "Downstream effects of dams on alluvial rivers." *Geological Survey Professional Paper (United States)*.

Winterwerp, J. C., and van Kesteren, W. G. M. (2004). "Introduction to the Physics of Cohesive Sediment in the Marine Environment." Elsevier.

Yoshida, H., Suenaga, K., and Echigo, R. (1990). "Turbulence structure and heat-transfer of a 2-dimensional impinging jet with gas solid suspensions." *International Journal of Heat and Mass Transfer*, 33(5), 859-867.

Zhu, Y., Lu, J., Liao, H., Wang, J., Fan, B., and Yao, S. (2008). "Research on cohesive sediment erosion by flow: An overview." *Science in China, Series E: Technological Sciences*, 51(11), 2001-2012.
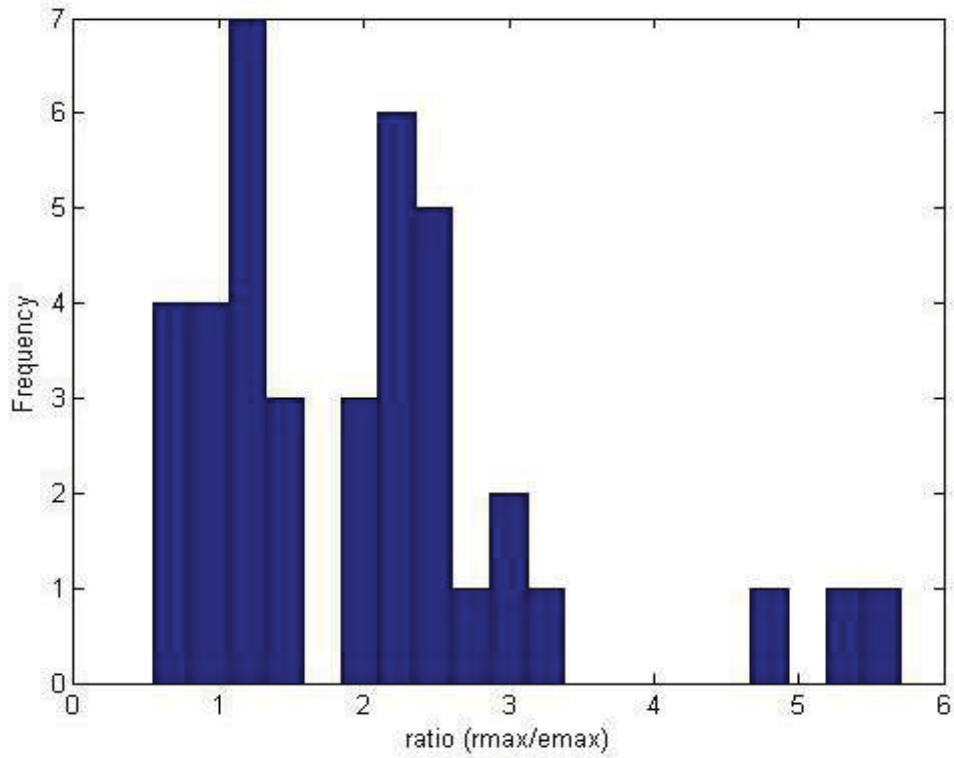
A. SUMMARY OF ASPECT RATIOS (MAZUREK 2001)

Figure A-1 Histogram of Aspect Ratios found in laboratory tests
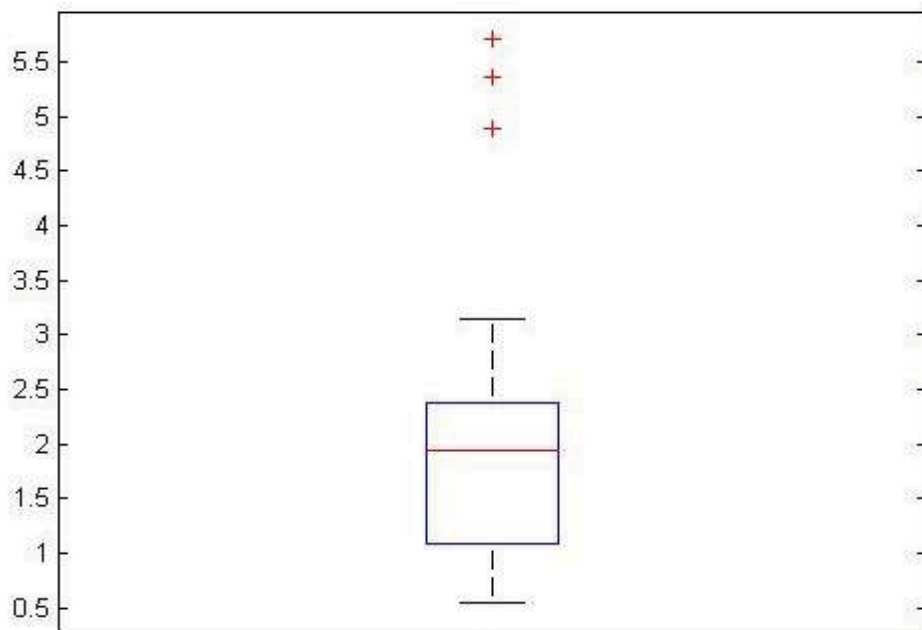
Figure A-2 Box and Whisker plot of the distribution of aspect ratios

B. Lower Roanoke River Jet Test Results

Table B-1 Summary of Jet Test Results

Test	Site	Head Tank Height (m)	U (m/s)	Max Scour Depth (cm)	Nozzle Diameter (in)	Nozzle Height, H (cm)	kd (m3/N-s)	τ_c (Pa)	Soil Type
T61L-1	S1	NA	6.54	2.43	0.25	7.88	4.00E-07	6.90	CL1
T61L-3	S1	2.9591	7.14	3.12	0.25	8.90	4.43E-07	1.18	CL2
S1T5	S1	3	7.14	2.93	0.25	9.62	5.96E-07	4.83	CL2
T61L-2-B	S1	NA	6.98	0.74	0.25	9.74	1.70E-07	12.13	MH
T61L-4	S1	NA	7.10	1.05	0.25	9.60	2.35E-07	14.81	MH
S1-1	S1	2.20	6.31	0.44	0.25	9.87	3.79E-07	19.54	MH
S1-2	S1	2.70	6.53	0.85	0.25	9.44	3.18E-07	16.88	MH
S1-4	S1	3.70	7.87	1.35	0.25	10.28	2.22E-07	2.48	MH
S1-6	S1	2.61	6.79	3.06	0.25	9.08	4.16E-07	1.14	MH
S1-7	S1	2.59	6.55	1.95	0.25	9.36	4.79E-07	6.11	MH
S1-8	S1	2.50	6.74	1.92	0.25	9.36	7.28E-07	13.19	MH
S1-9	S1	2.59	6.65	1.99	0.25	10.46	4.67E-07	3.42	MH
T61L-2-A	S1	2.15	6.10	0.43	0.25	8.73	2.21E-07	21.50	MH
S1-L	S1	1.88	5.58	3.20	0.25	7.97	7.69E-07	2.23	SM
S2-R	S2	1.10	4.55	3.06	0.25	7.82	9.96E-07	1.07	CL
11BR	S2	2.40	5.95	0.32	0.25	10.70	3.91E-07	14.89	
S2-R-1	S2	1.70	5.46	8.77	0.25	7.49	6.13E-06	3.82	CL
S3-R1	S3	1.93	5.27	4.64	0.25	8.43	1.39E-06	0.53	ML
S3-R-2	S3	2.97	6.44	3.38	0.25	9.82	2.39E-06	10.79	ML
S3 T1	S3	1.71	4.68	1.47	0.25	6.98	5.77E-07	10.57	ML
S3 T2	S3	1.48	4.50	2.24	0.25	9.52	1.12E-06	1.63	ML
Site 4-L	S4	2.43	6.05	3.82	0.25	9.63	2.03E-06	6.01	CL
S4-L-2-2	S4	NA	6.10	0.86	0.25	8.83	1.73E-07	9.26	ML
S4-L-2-1	S4	NA	5.72	1.22	0.25	8.24	2.72E-07	9.95	
S5 14	S5	NA	4.53	3.80	0.25	9.68	2.23E-06	1.19	ML
S5T2	S5	2.10	5.94	1.96	0.25	8.86	7.36E-07	8.51	ML
S5T3	S5	2.04	5.90	0.66	0.25	9.11	2.11E-07	10.86	ML

Table B-2 Summary of Soil Properties for the 3 soil types

USCS	Sand %	Silt %	Clay %	LL	PI	No. of Sample
CL	16.6	50.2	33.2	41.8	18.6	26
	10.9	8.1	7.3	5.8	3.9	
ML	25.8	47.9	26.3	41.0	13.8	10 (3)*
	18.4	10.9	9.5	11.9	7.2	
MH	9.2	44.7	46.2	52.7	21.6	7
	3.3	2.9	2.8	2.4	2.4	

* 10 samples for grain size distribution and 3 samples for Atterberg tests.
**Upper rows present average value, lower rows present standard deviation.
***LL=Liquid Limit, PI=Plasticity Index

C. Results from ANSYS FLUENT Models

The following appendix includes results from each of the ANSYS FLUENT models. Each page includes a summary of the input values as well as results in terms of the maximum shear stress and the distance, r/H, to the maximum shear stress. H is defined as the distance from the nozzle to the scour hole centerline. In each figure, the mesh for each case is presented first (a) followed by a contour plot showing the entire model domain (b). The contour plots show the general behavior of the jet flow. The final two figures depict the flow fields within each scour hole. The first vector plot (c) shows the magnitude of the velocities within the hole and the normalized vector plot (d) shows the directional behavior of the velocities within the scour hole.

a)

b)

c)
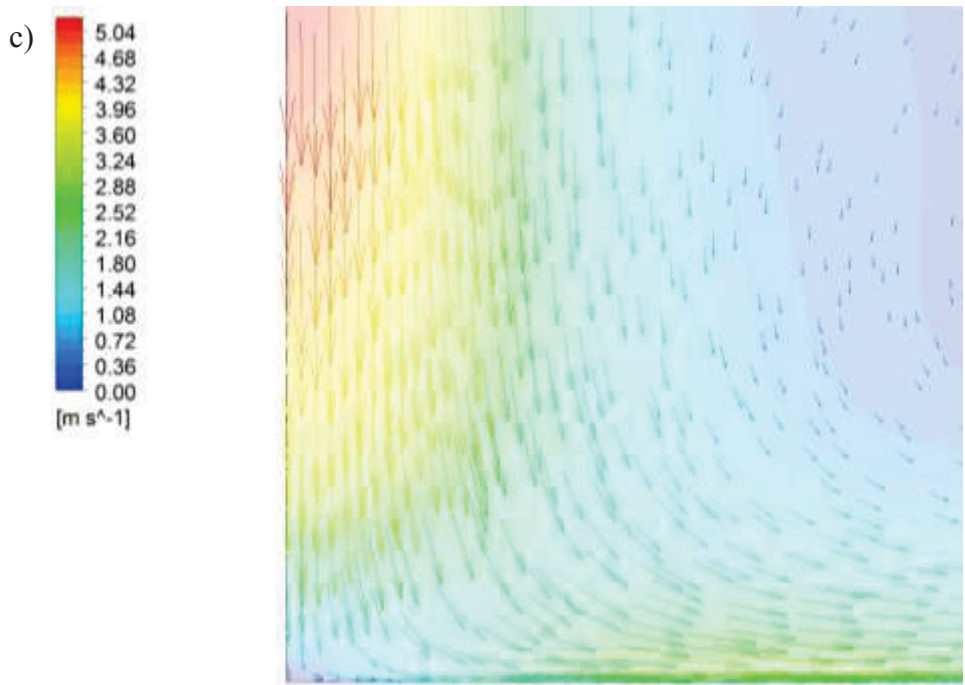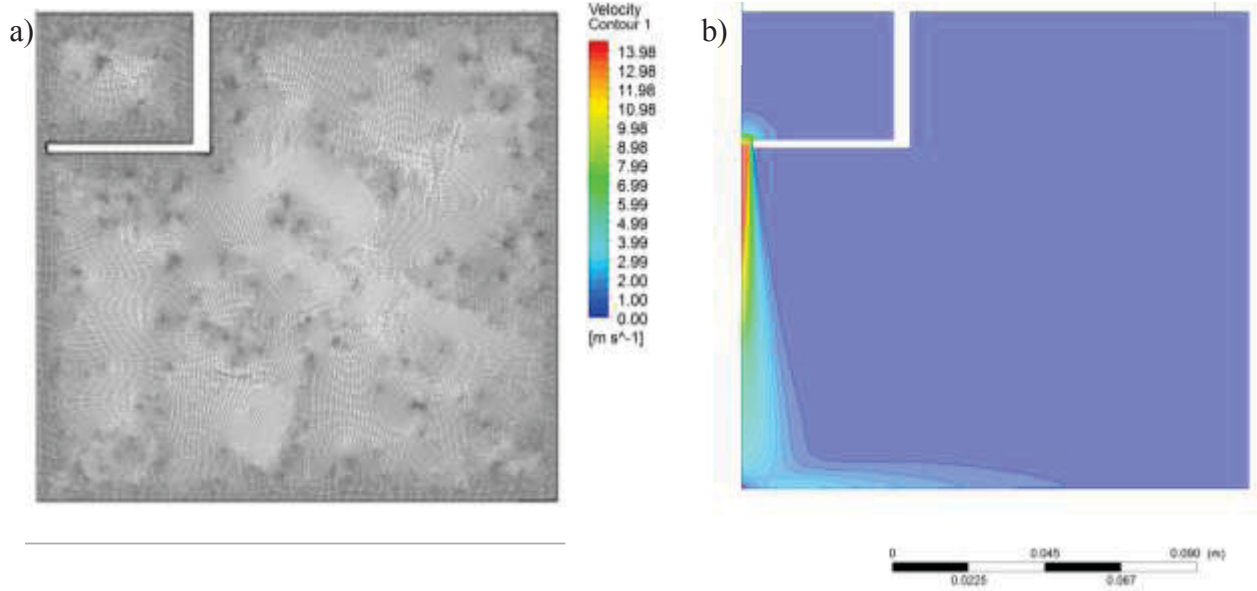
Depth, e (cm)	0.0
Radius, r (cm)	0.0
Ratio, $R = \varepsilon/r$	0.0
Nozzle Diameter, d (cm)	0.64
Initial Distance from Nozzle, H (cm)	10
Average Jet Velocity, U_0 (m/s)	10
Max Shear, τ (Pa)	100.65
Location of Max Shear Stress, r/H	0.120

Figure C-1 Result of Scour Hole Model, Flat Plate. a) Mesh, b) Contours, c) Velocity Vectors near the impingement point

a)

b)

Velocity
R05 E05

14.28
13.26
12.24
11.22
10.20
9.18
8.16
7.14
6.12
5.10
4.08
3.06
2.04
1.02
0.00

[m s^-1]

c)

Velocity
R05 E05 Vector 1

3.01

2.26

1.51

0.75

0.00

[m s^-1]

d)
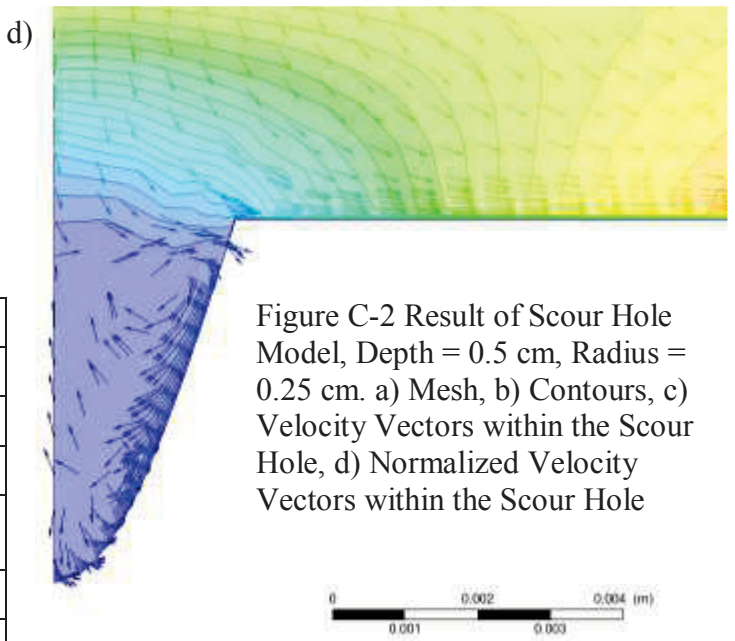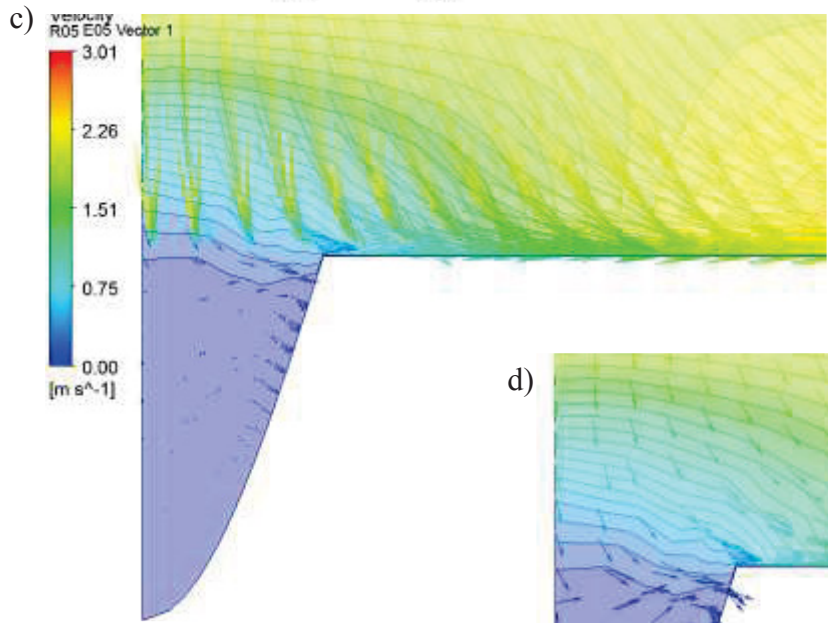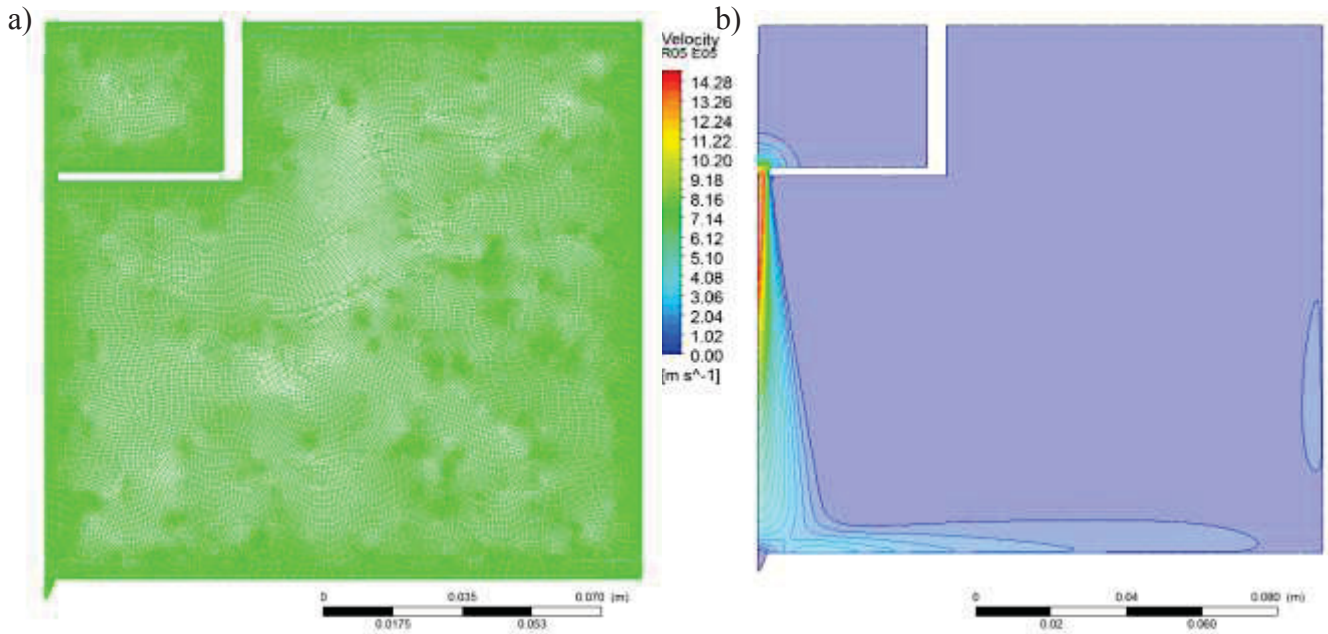
Depth, e (cm)	0.5
Radius, r (cm)	0.25
Ratio, $R = \varepsilon/r$	0.5
Nozzle Diameter, d (cm)	0.64
Initial Distance from Nozzle, H (cm)	10
Average Jet Velocity, U_0 (m/s)	10
Max Shear, τ (Pa)	107.58
Location of Max Shear Stress, r/H	0.114

Figure C-2 Result of Scour Hole Model, Depth = 0.5 cm, Radius = 0.25 cm. a) Mesh, b) Contours, c) Velocity Vectors within the Scour Hole, d) Normalized Velocity Vectors within the Scour Hole
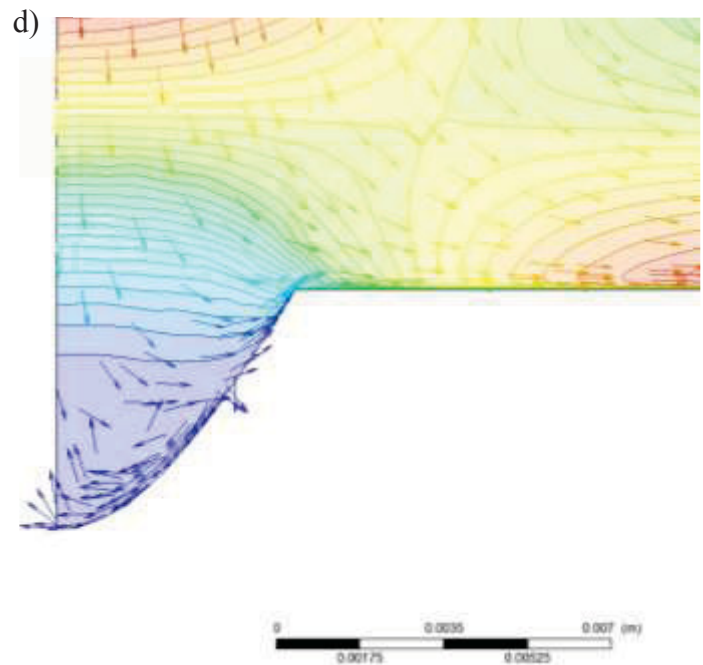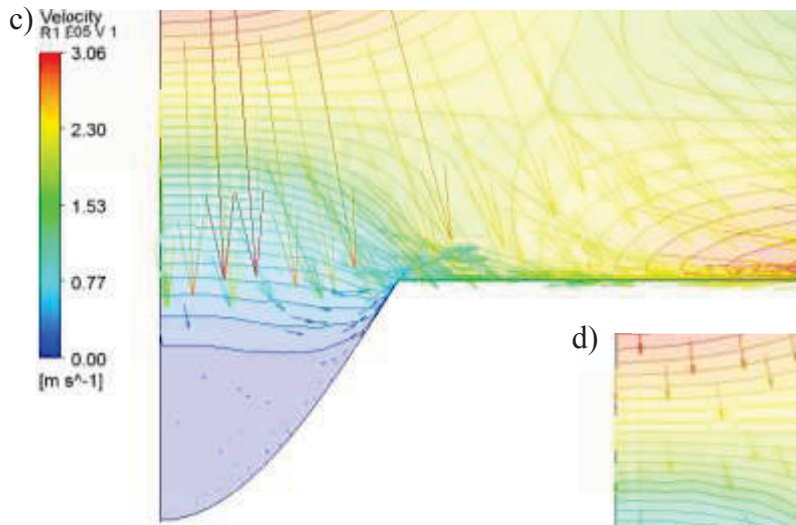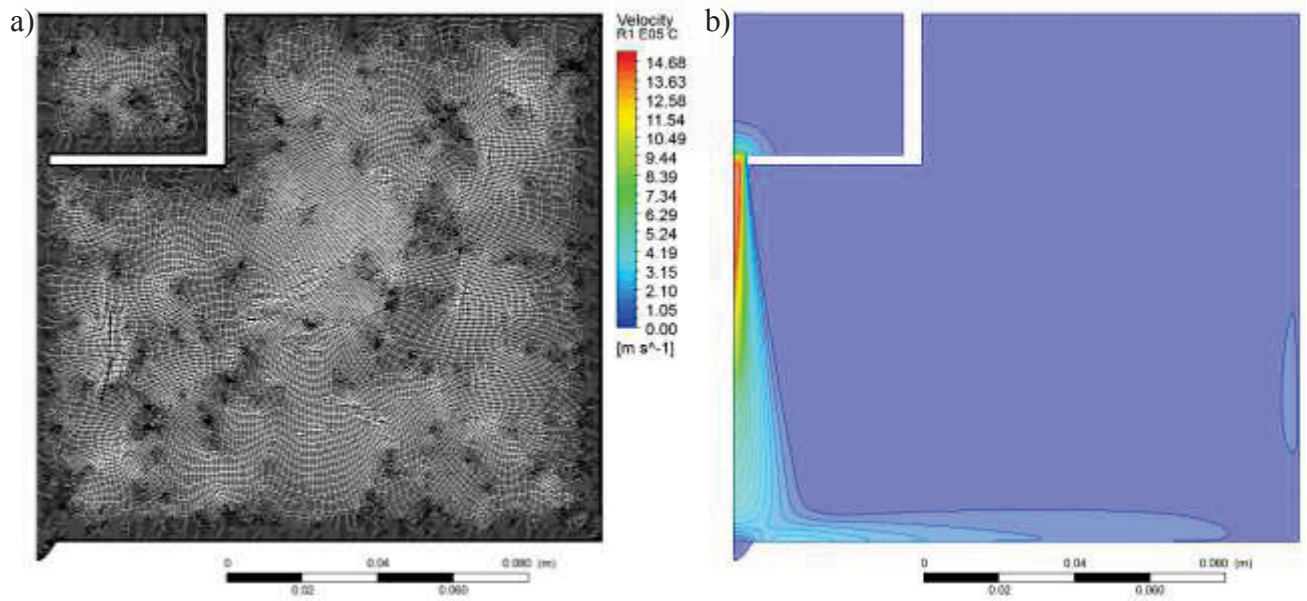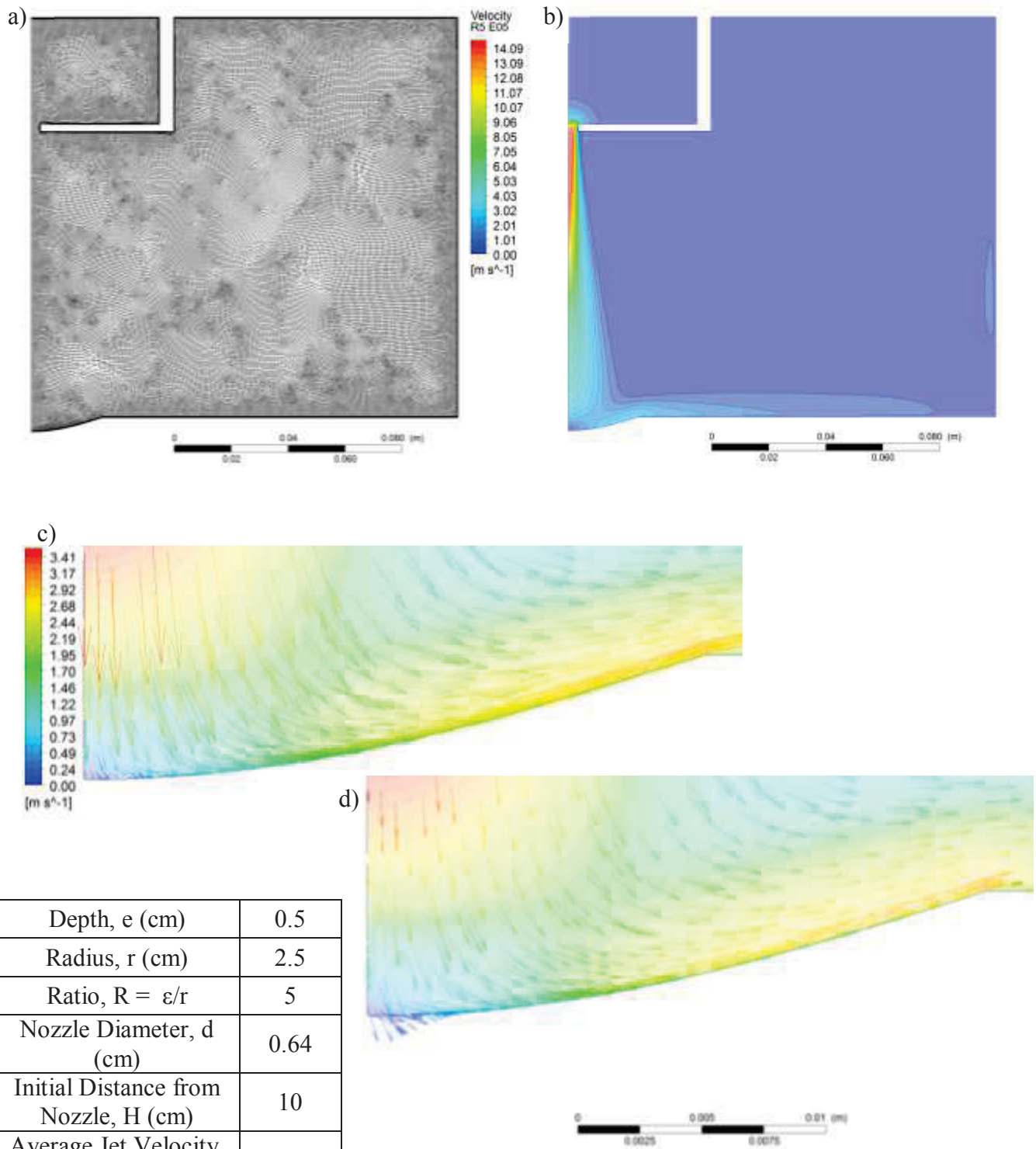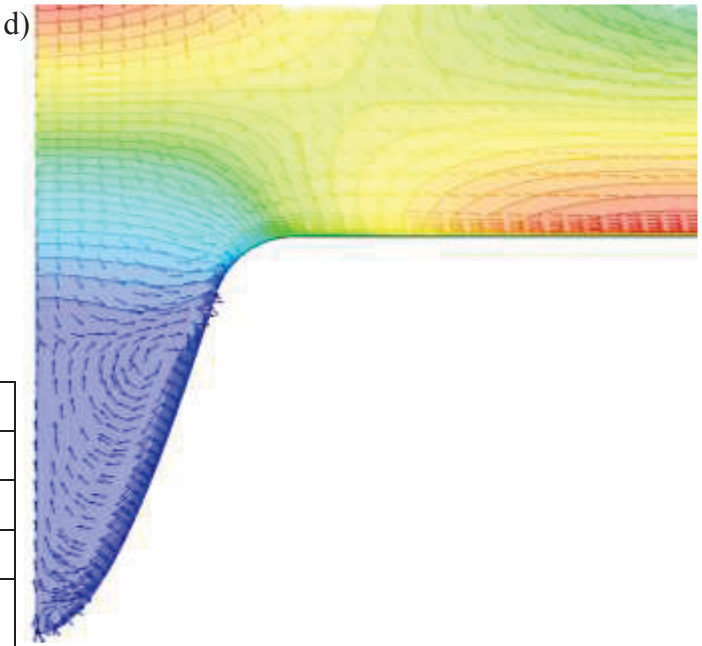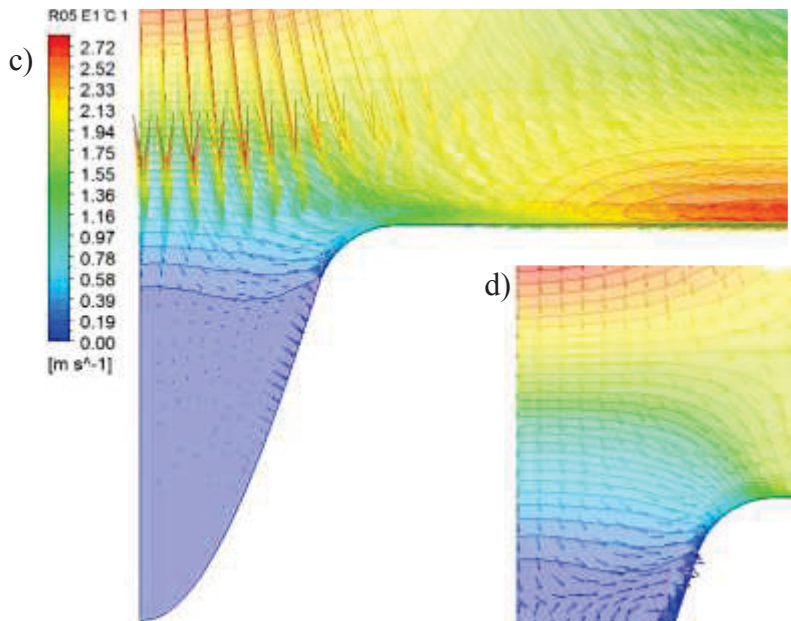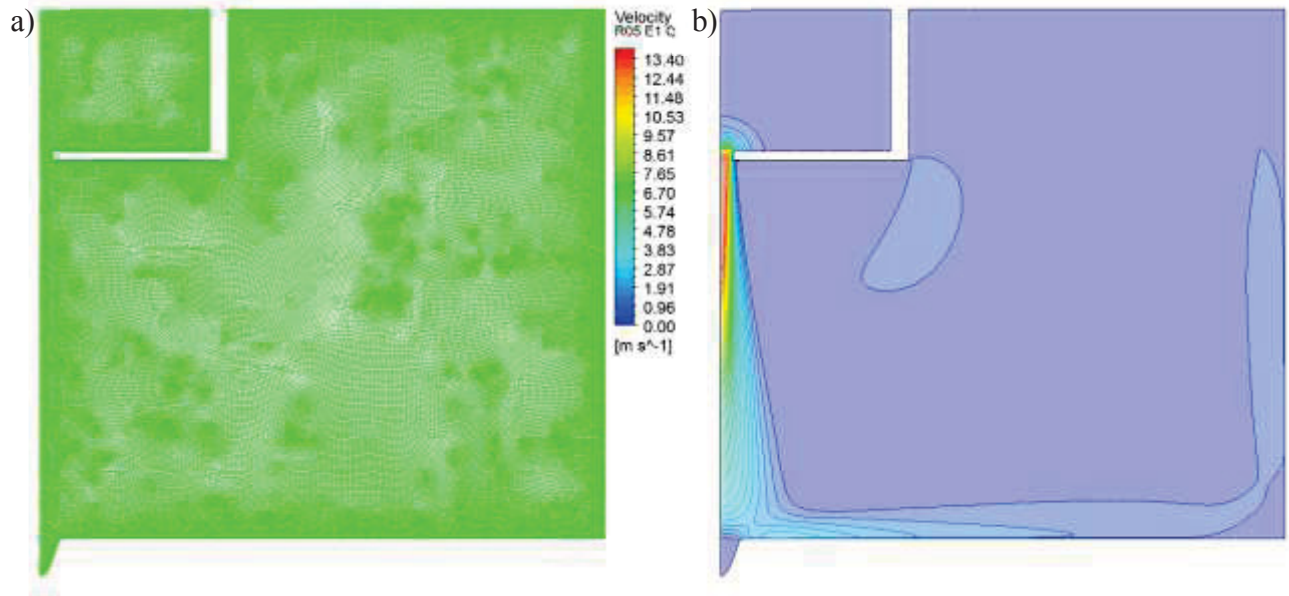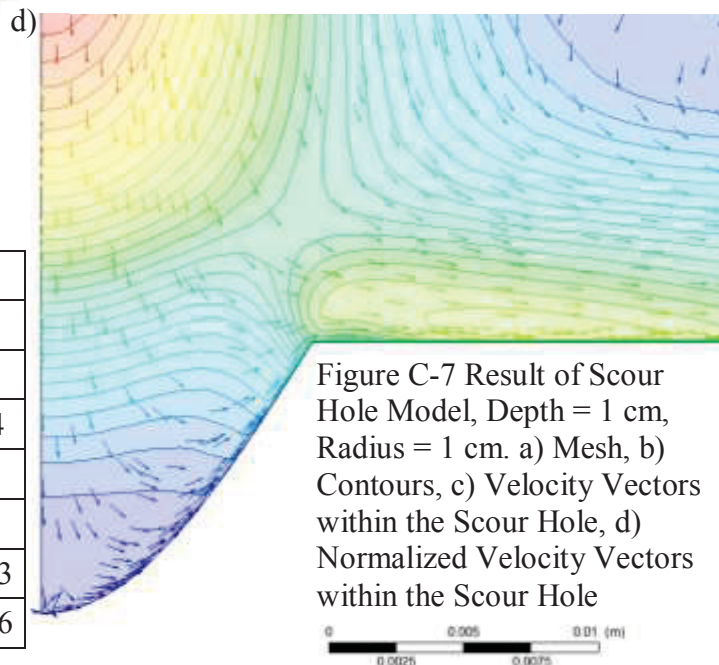
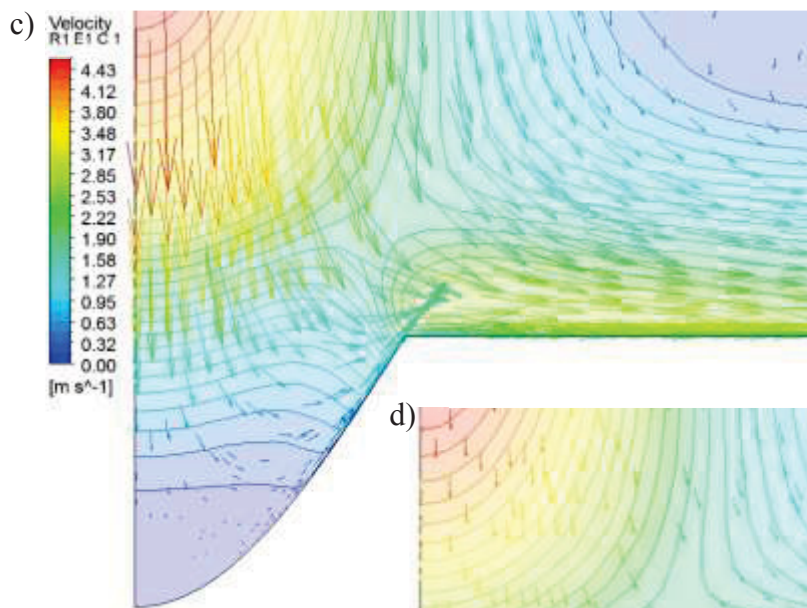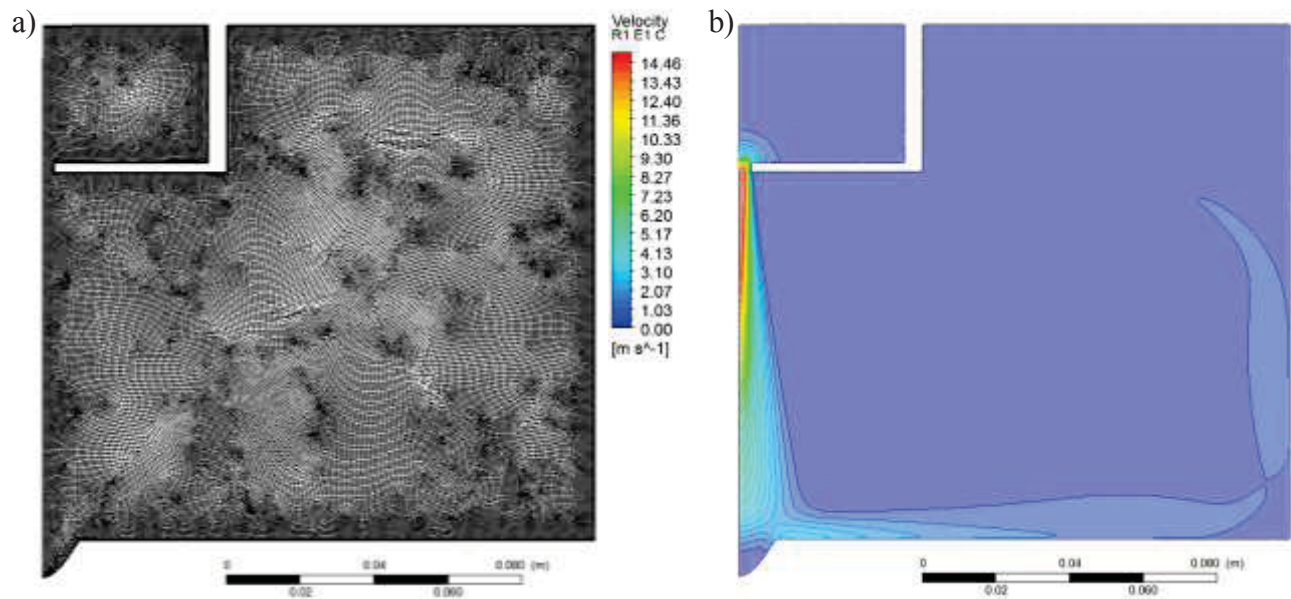| Depth, e (cm)	0.5
Radius, r (cm)	0.5
Ratio, R = ε/r	1
Nozzle Diameter, d (cm)	0.64
Initial Distance from Nozzle, H (cm)	10
Average Jet Velocity, U_0 (m/s)	10
Max Shear, τ (Pa)	110.4655
Location of Max Shear Stress, r/H	0.114041

Figure C-3 Result of Scour Hole Model, Depth = 0.5 cm, Radius = 0.5 cm. a) Mesh, b) Contours, c) Velocity Vectors within the Scour Hole, d) Normalized Velocity Vectors within the Scour Hole

Depth, e (cm)	0.5
Radius, r (cm)	1.25
Ratio, ε/r	2.5
Nozzle Diameter, d (cm)	0.64
Initial Distance from Nozzle, H (cm)	10
Average Jet Velocity, U_0 (m/s)	10
Max Shear, τ (Pa)	80.96
Location of Max Shear Stress, r/H	0.151
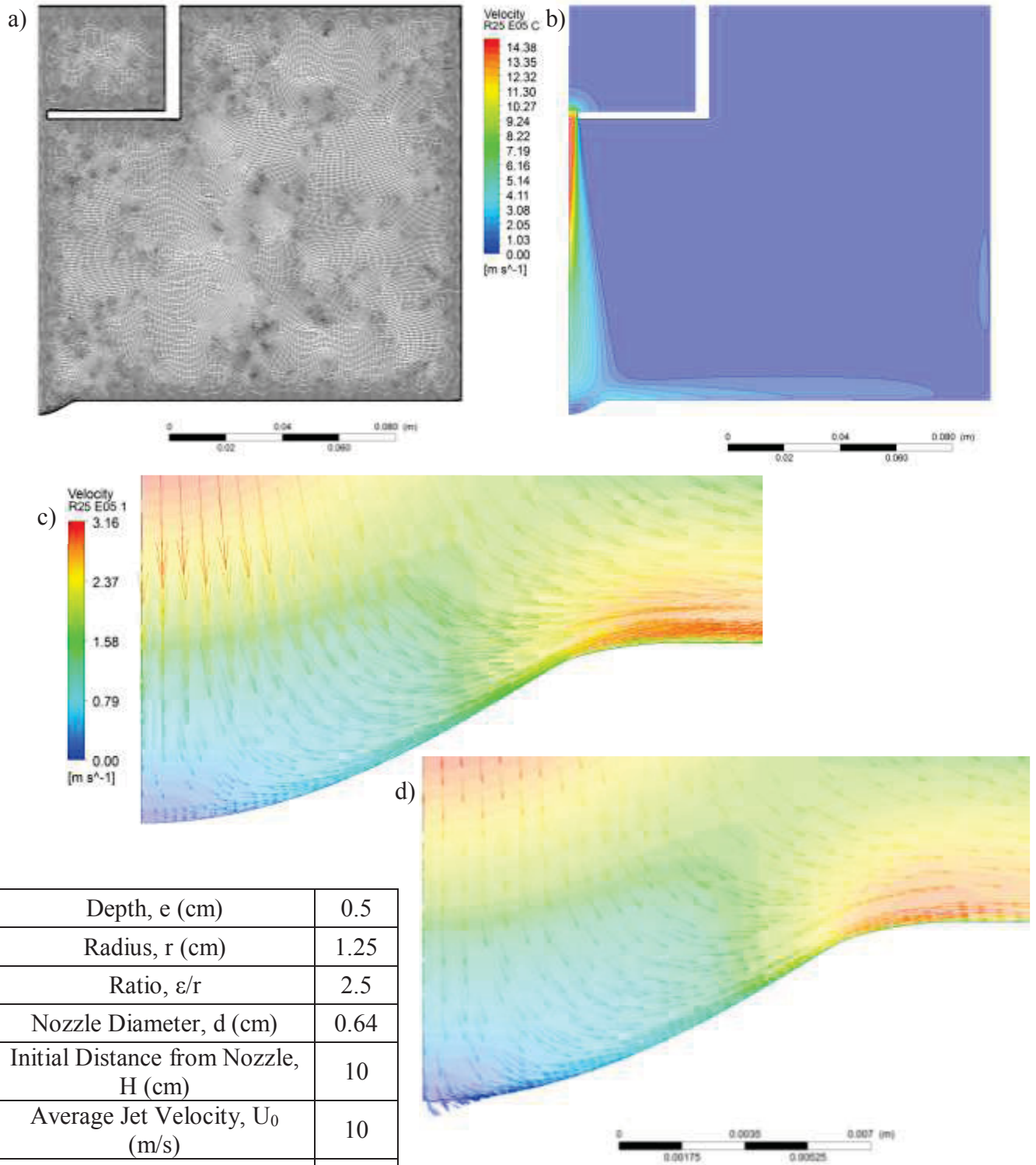
Figure C-4 Result of Scour Hole Model, Depth = 0.5 cm, Radius = 1.25 cm. a) Mesh, b) Contours, c) Velocity Vectors within the Scour Hole, d) Normalized Velocity Vectors within the Scour Hole
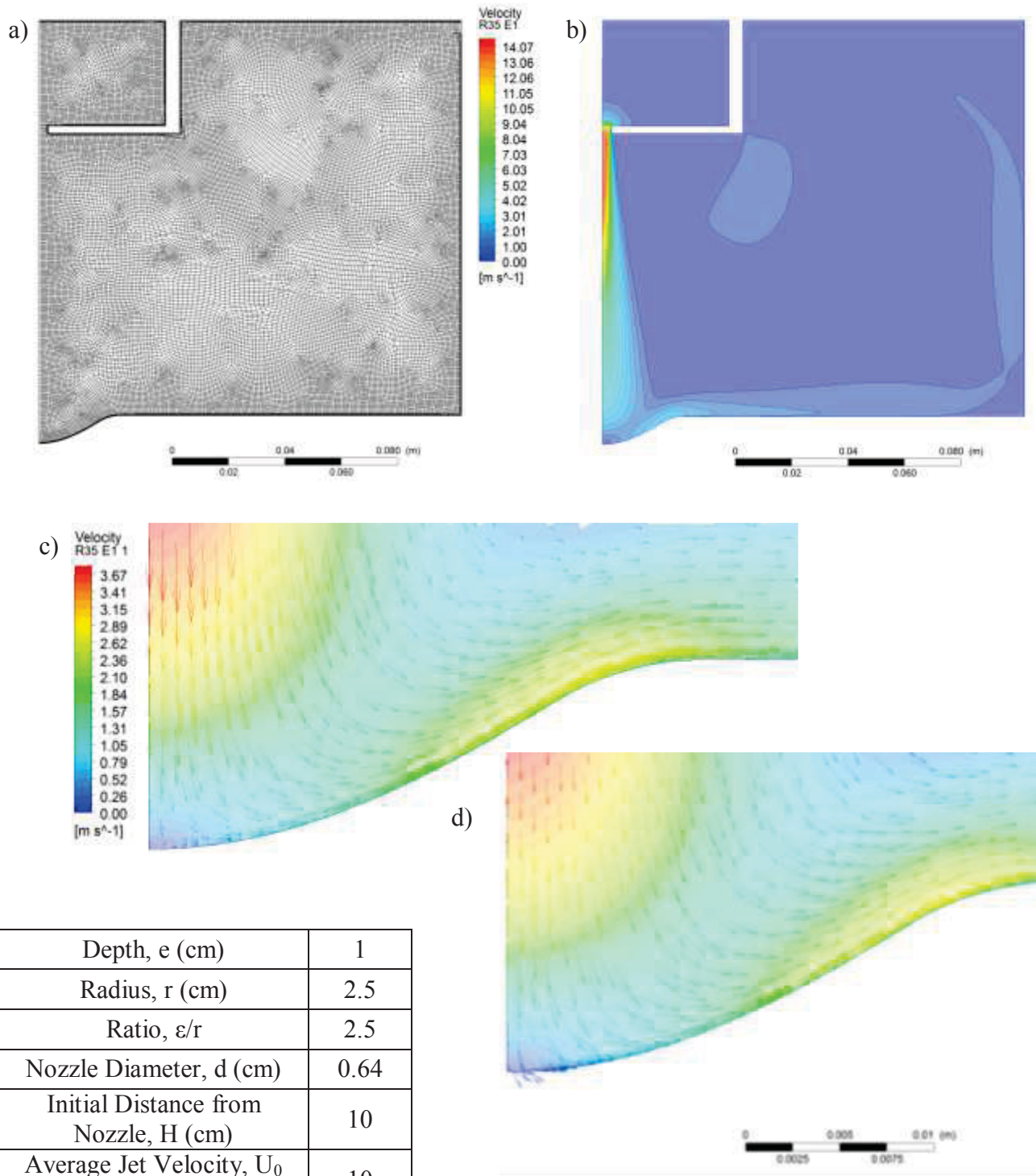
61

Depth, e (cm)	0.5
Radius, r (cm)	2.5
Ratio, $R = \varepsilon/r$	5
Nozzle Diameter, d (cm)	0.64
Initial Distance from Nozzle, H (cm)	10
Average Jet Velocity, U_0 (m/s)	10
Max Shear, τ (Pa)	95.94
Location of Max Shear Stress, r/H	0.144

Figure C-5 Result of Scour Hole Model, Depth = 0.5 cm, Radius = 2.5 cm. a) Mesh, b) Contours, c) Velocity Vectors within the Scour Hole, d) Normalized Velocity Vectors within the Scour Hole
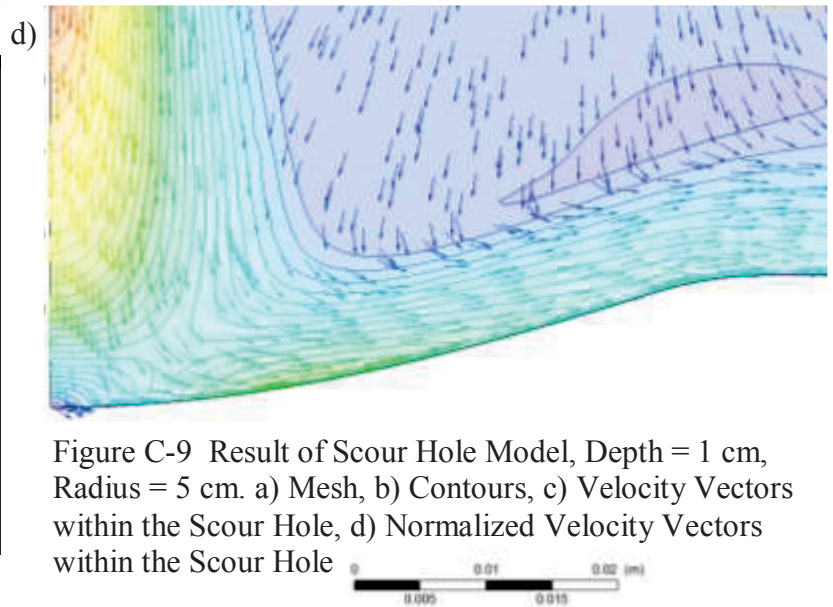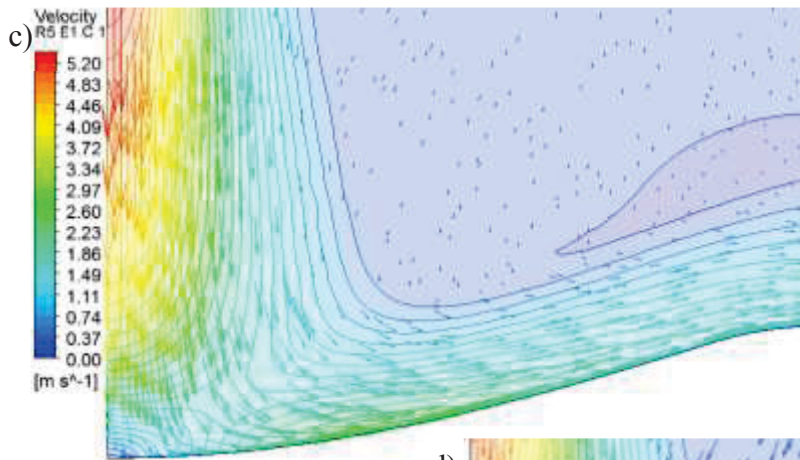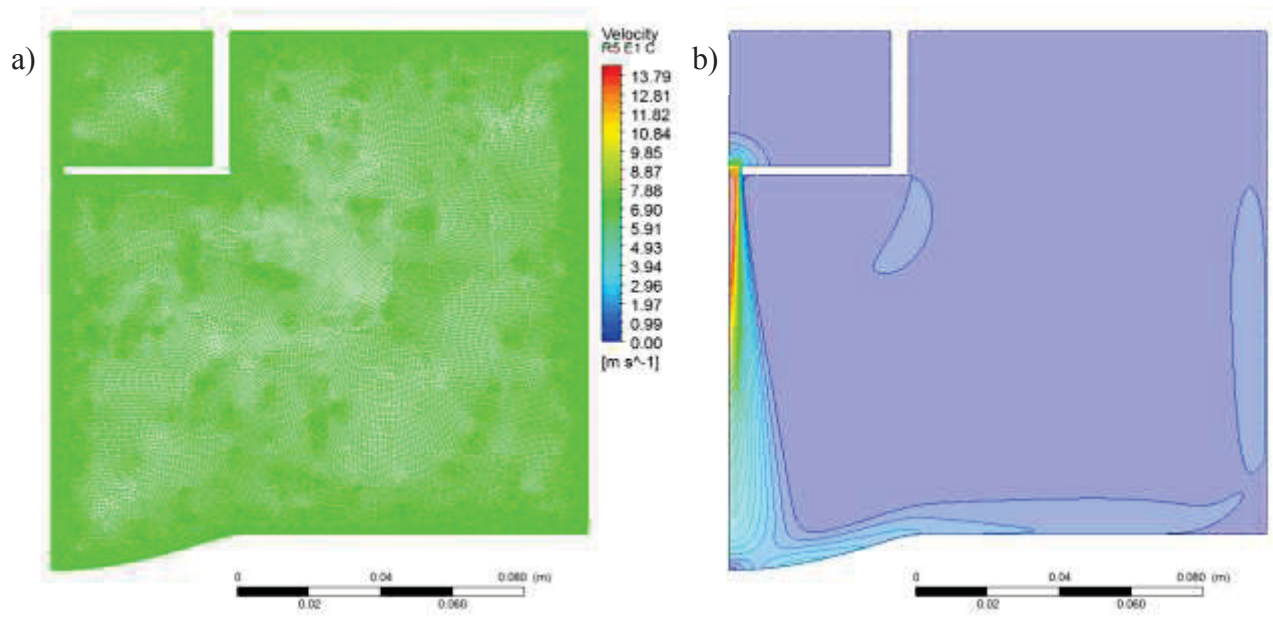
Depth, e (cm)	1
Radius, r (cm)	0.5
Ratio, R = ε/r	0.5
Nozzle Diameter, d (cm)	0.64
Initial Distance from Nozzle, H (cm)	10
Average Jet Velocity, U₀ (m/s)	10
Max Shear, τ (Pa)	93.81
Location of Max Shear Stress, r/H	0.118

Figure C-6 Result of Scour Hole Model, Depth = 1 cm, Radius = 0.5 cm. a) Mesh, b) Contours, c) Velocity Vectors within the Scour Hole, d) Normalized Velocity Vectors within the Scour Hole
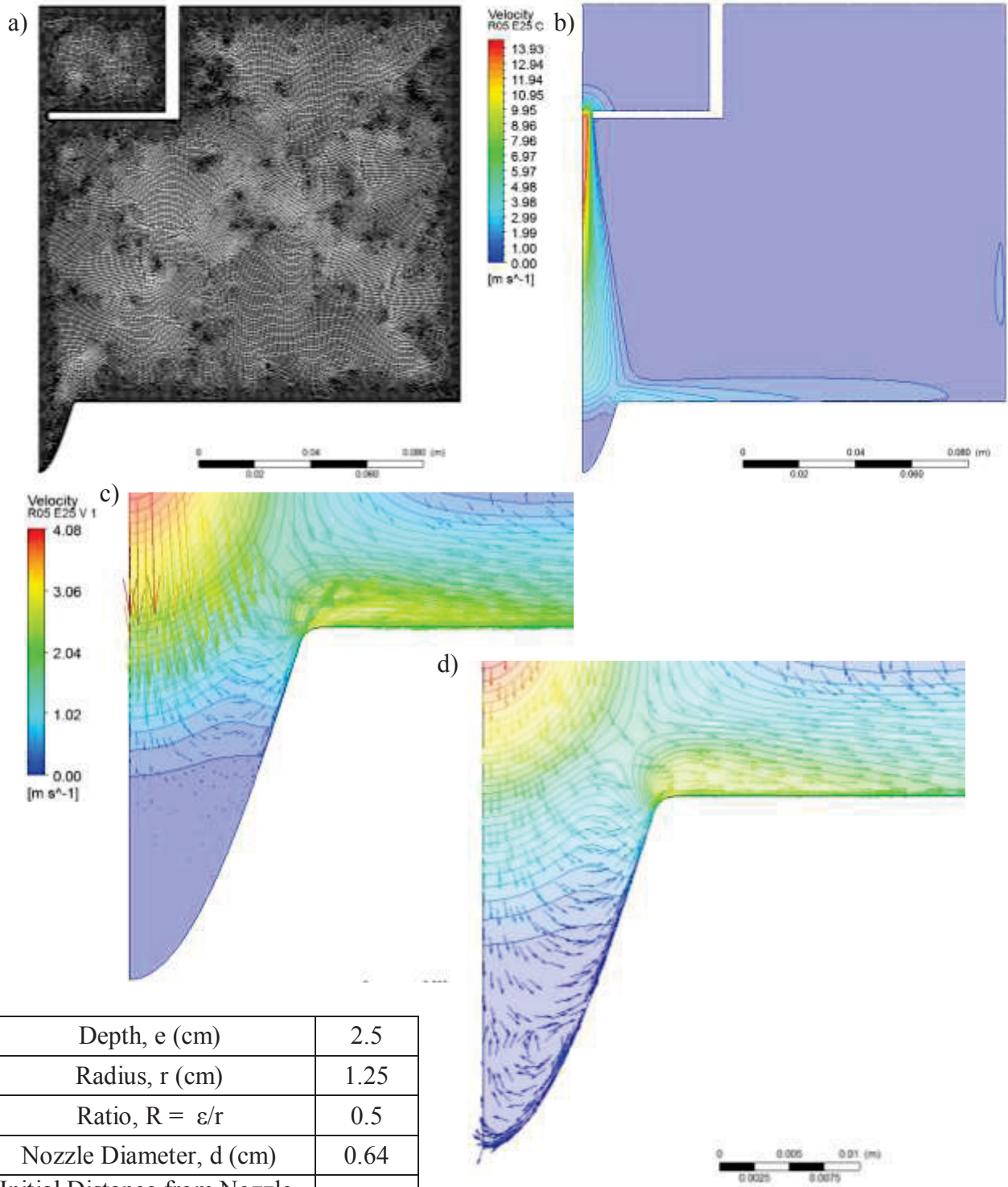
63

Depth, e (cm)	1
Radius, r (cm)	1
Ratio, $R = \varepsilon/r$	1
Nozzle Diameter, d (cm)	0.64
Initial Distance from Nozzle, H (cm)	10
Average Jet Velocity, U_0 (m/s)	10
Max Shear, τ (Pa)	93.13
Location of Max Shear Stress, r/H	0.136

Figure C-7 Result of Scour Hole Model, Depth = 1 cm, Radius = 1 cm. a) Mesh, b) Contours, c) Velocity Vectors within the Scour Hole, d) Normalized Velocity Vectors within the Scour Hole
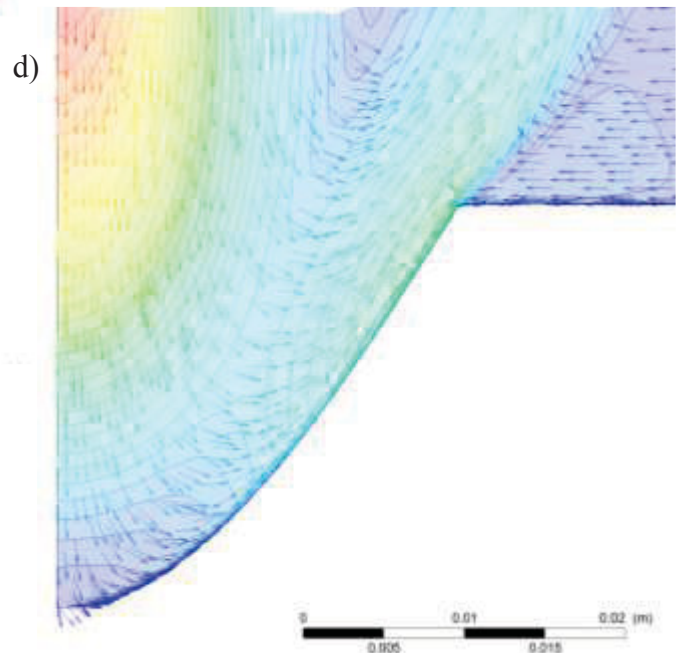
Depth, e (cm)	1
Radius, r (cm)	2.5
Ratio, ε/r	2.5
Nozzle Diameter, d (cm)	0.64
Initial Distance from Nozzle, H (cm)	10
Average Jet Velocity, U_0 (m/s)	10
Max Shear, τ (Pa)	75.31
Location of Max Shear Stress, r/H	0.163

Figure C-8 Result of Scour Hole Model, Depth = 1 cm, Radius = 2.5 cm. a) Mesh, b) Contours, c) Velocity Vectors within the Scour Hole, d) Normalized Velocity Vectors within the Scour Hole
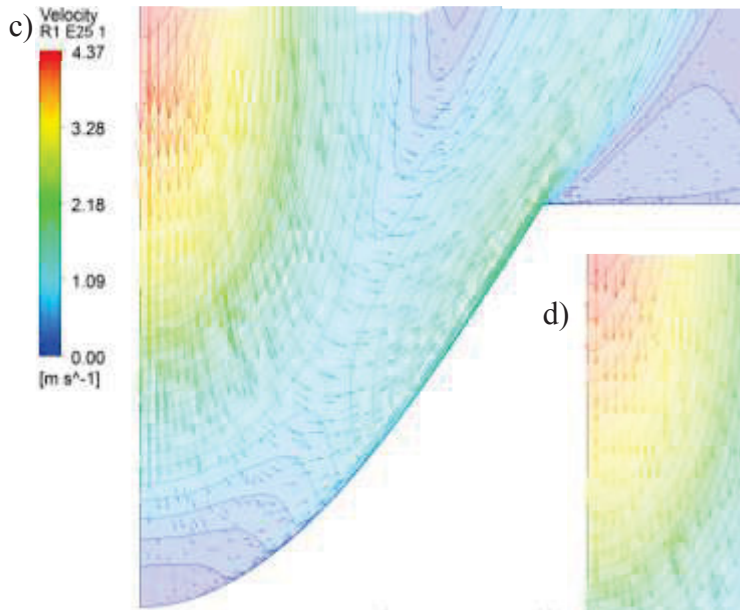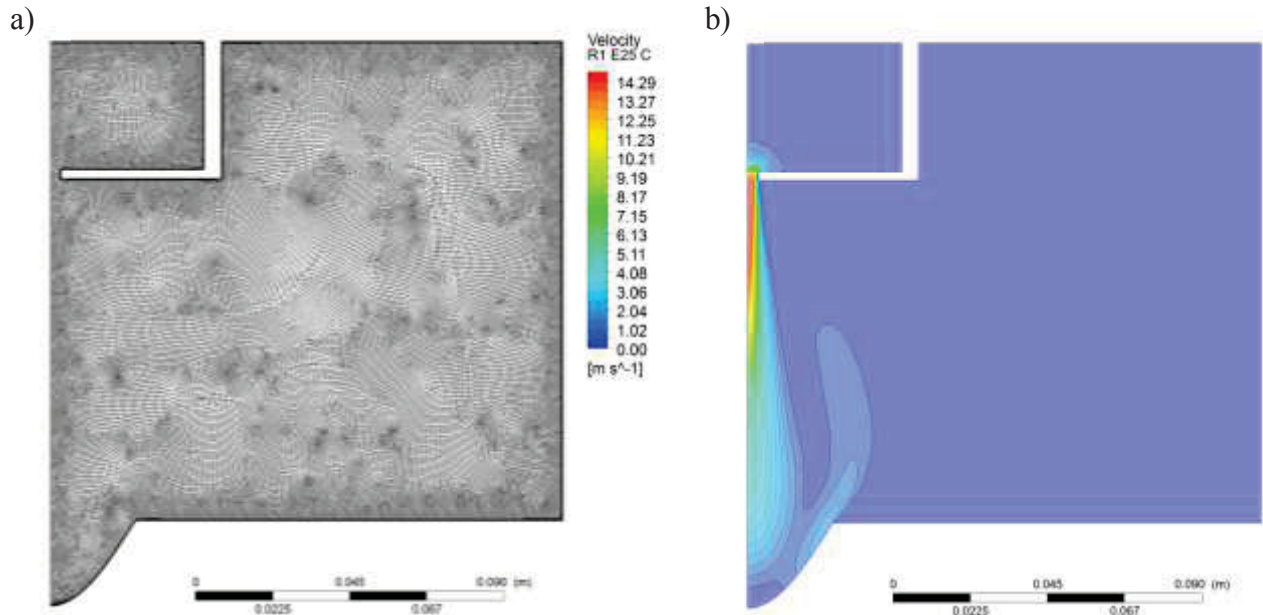
65

Depth, e (cm)	1
Radius, r (cm)	5
Ratio, $R = \varepsilon/r$	5
Nozzle Diameter, d (cm)	0.64
Initial Distance from Nozzle, H (cm)	10
Average Jet Velocity, U_0 (m/s)	10
Max Shear, τ (Pa)	82.61
Location of Max Shear Stress, r/H	0.124

Figure C-9 Result of Scour Hole Model, Depth = 1 cm, Radius = 5 cm. a) Mesh, b) Contours, c) Velocity Vectors within the Scour Hole, d) Normalized Velocity Vectors within the Scour Hole

Depth, e (cm)	2.5
Radius, r (cm)	1.25
Ratio, R = ε/r	0.5
Nozzle Diameter, d (cm)	0.64
Initial Distance from Nozzle, H (cm)	10
Average Jet Velocity, U_0 (m/s)	10
Max Shear, τ (Pa)	59.36
Location of Max Shear Stress, r/H	0.152

Figure C-10 Result of Scour Hole Model, Depth = 2.5 cm, Radius = 1.25 cm. a) Mesh, b) Contours, c) Velocity Vectors within the Scour Hole, d) Normalized Velocity Vectors within the Scour Hole

Depth, e (cm)	2.5
Radius, r (cm)	2.5
Ratio, $R = \varepsilon/r$	1
Nozzle Diameter, d (cm)	0.64
Initial Distance from Nozzle, H (cm)	10
Average Jet Velocity, U_0 (m/s)	10
Max Shear, τ (Pa)	48.60
Location of Max Shear Stress, r/H	0.179

Figure C-11 Result of Scour Hole Model, Depth = 2.5 cm, Radius = 2.5 cm. a) Mesh, b) Contours, c) Velocity Vectors within the Scour Hole, d) Normalized Velocity Vectors within the Scour Hole
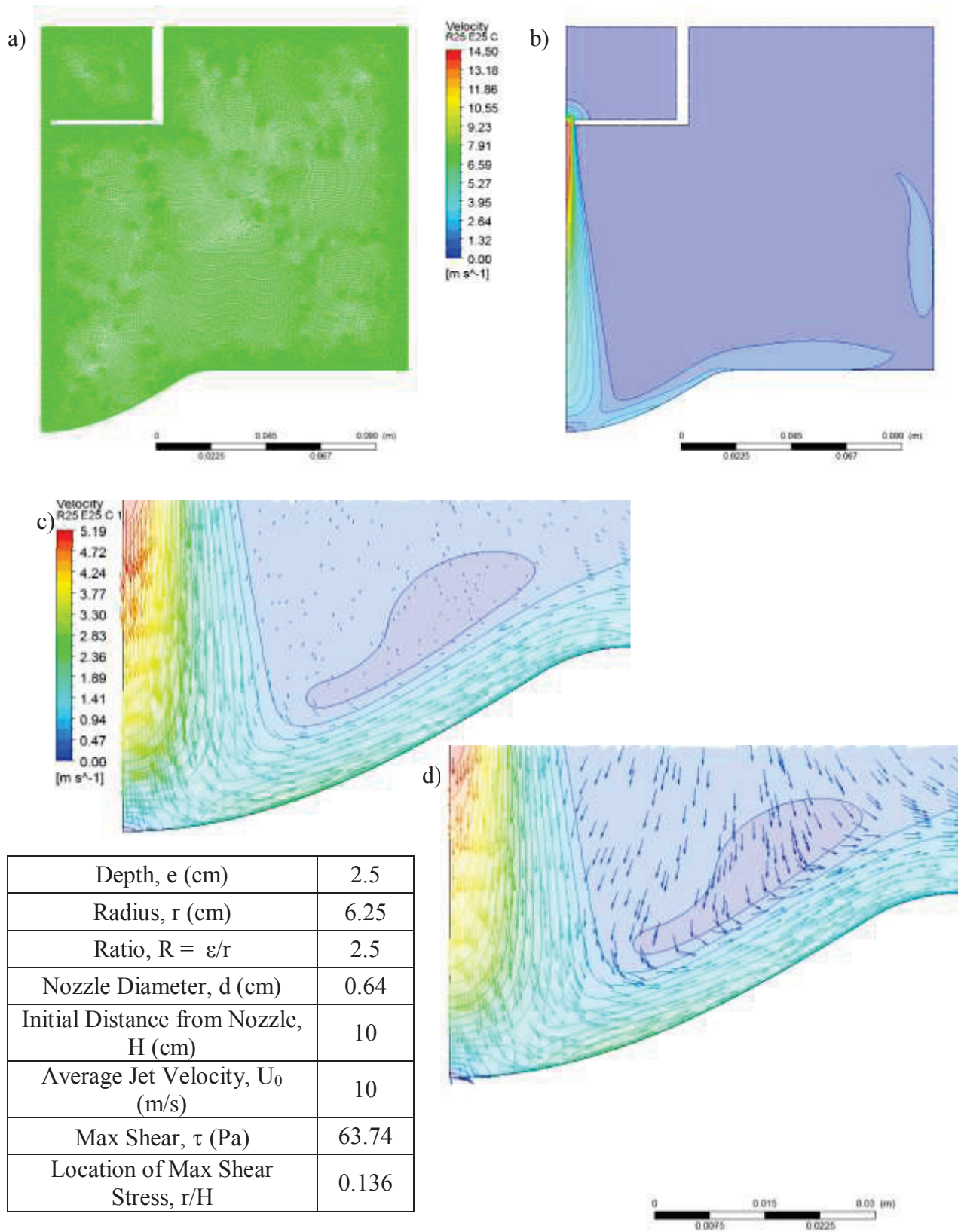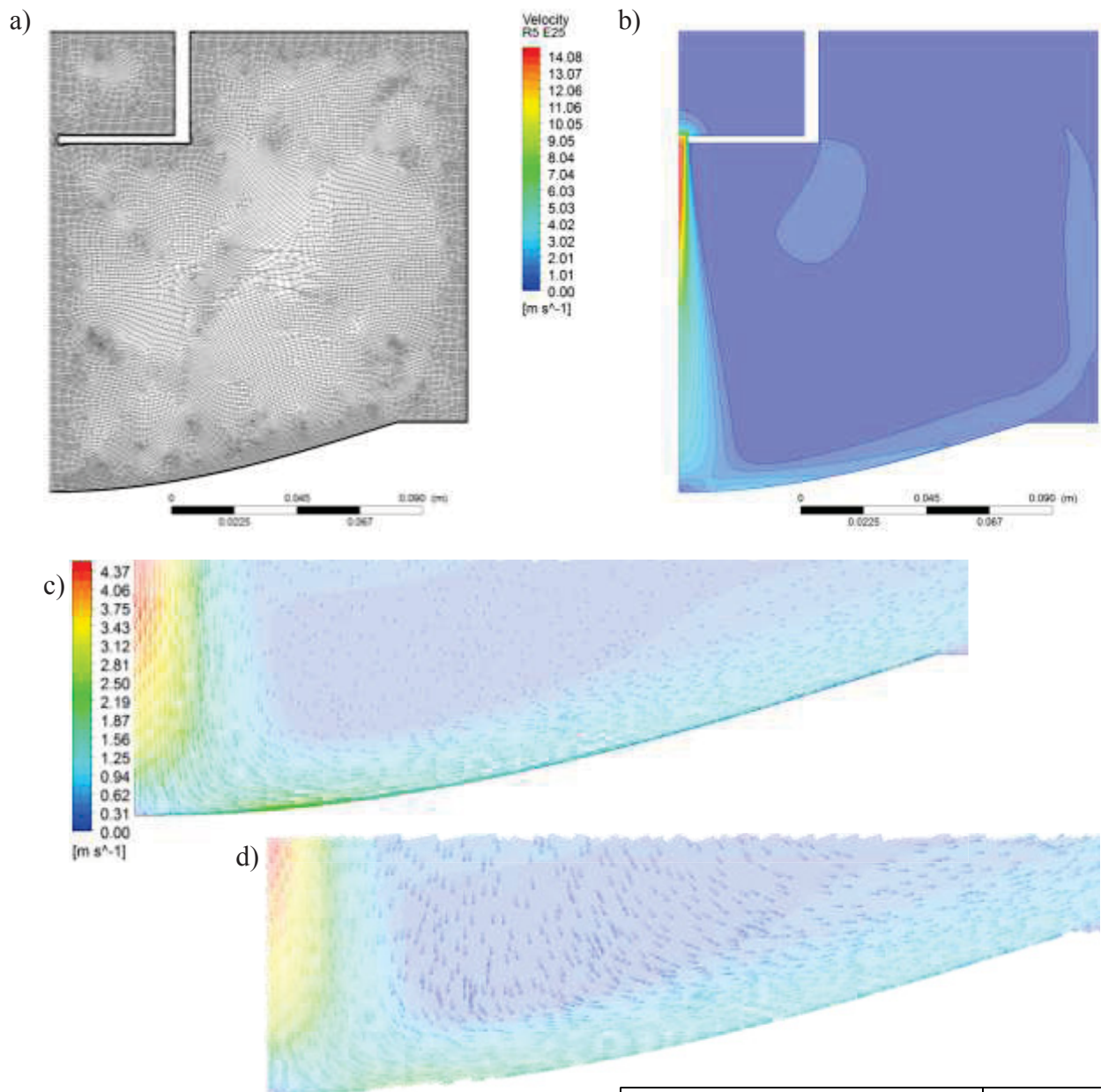
68

Depth, e (cm)	2.5
Radius, r (cm)	6.25
Ratio, R = ε/r	2.5
Nozzle Diameter, d (cm)	0.64
Initial Distance from Nozzle, H (cm)	10
Average Jet Velocity, U_0 (m/s)	10
Max Shear, τ (Pa)	63.74
Location of Max Shear Stress, r/H	0.136

Figure C-12 Result of Scour Hole Model, Depth = 2.5 cm, Radius = 6.25 cm. a) Mesh, b) Contours, c) Velocity Vectors within the Scour Hole, d) Normalized Velocity Vectors within the Scour Hole
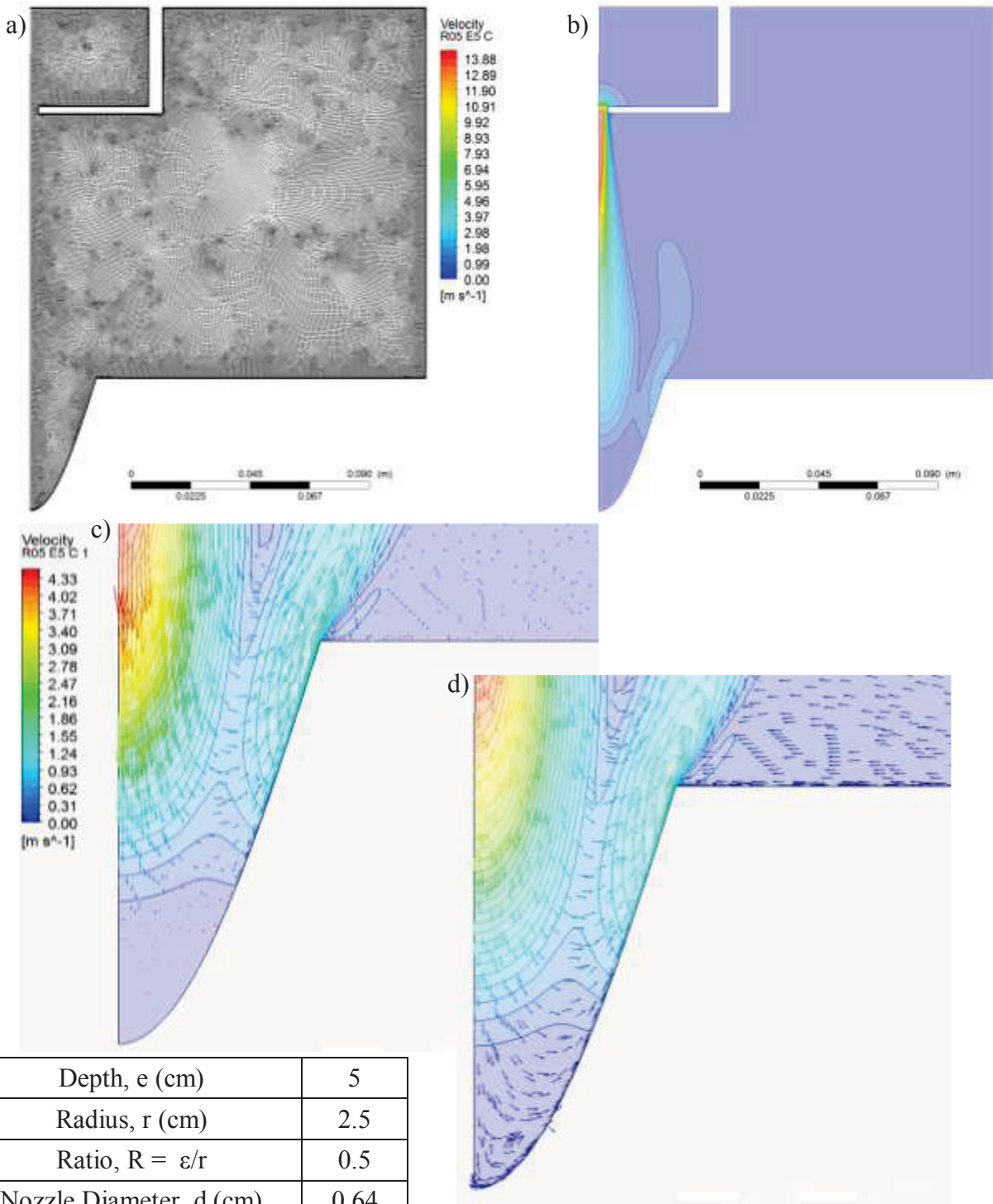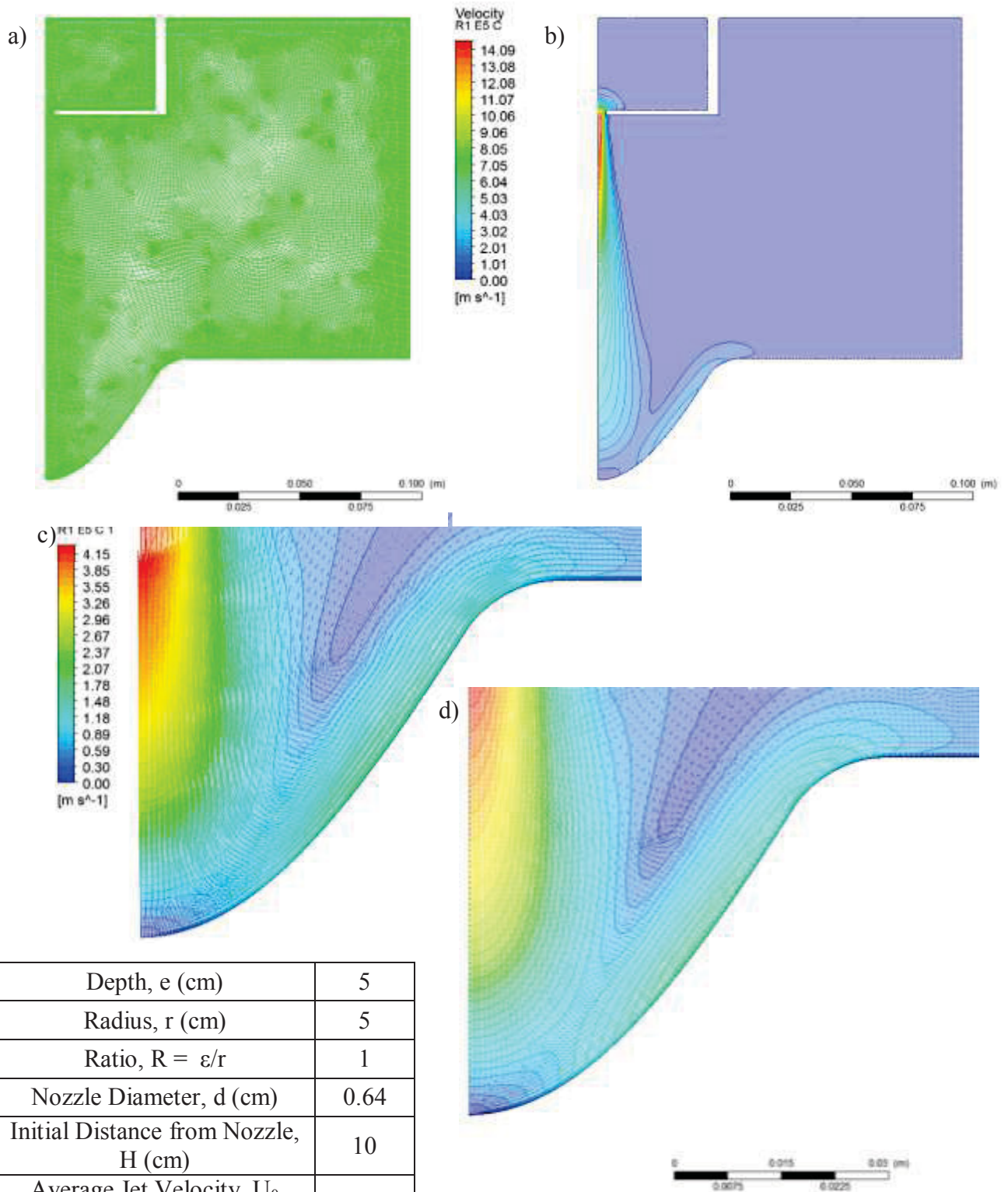
Figure C-13 Result of Scour Hole Model, Depth = 2.5 cm, Radius = 12.5 cm. a) Mesh, b) Contours, c) Velocity Vectors within the Scour Hole, d) Normalized Velocity Vectors within the Scour Hole

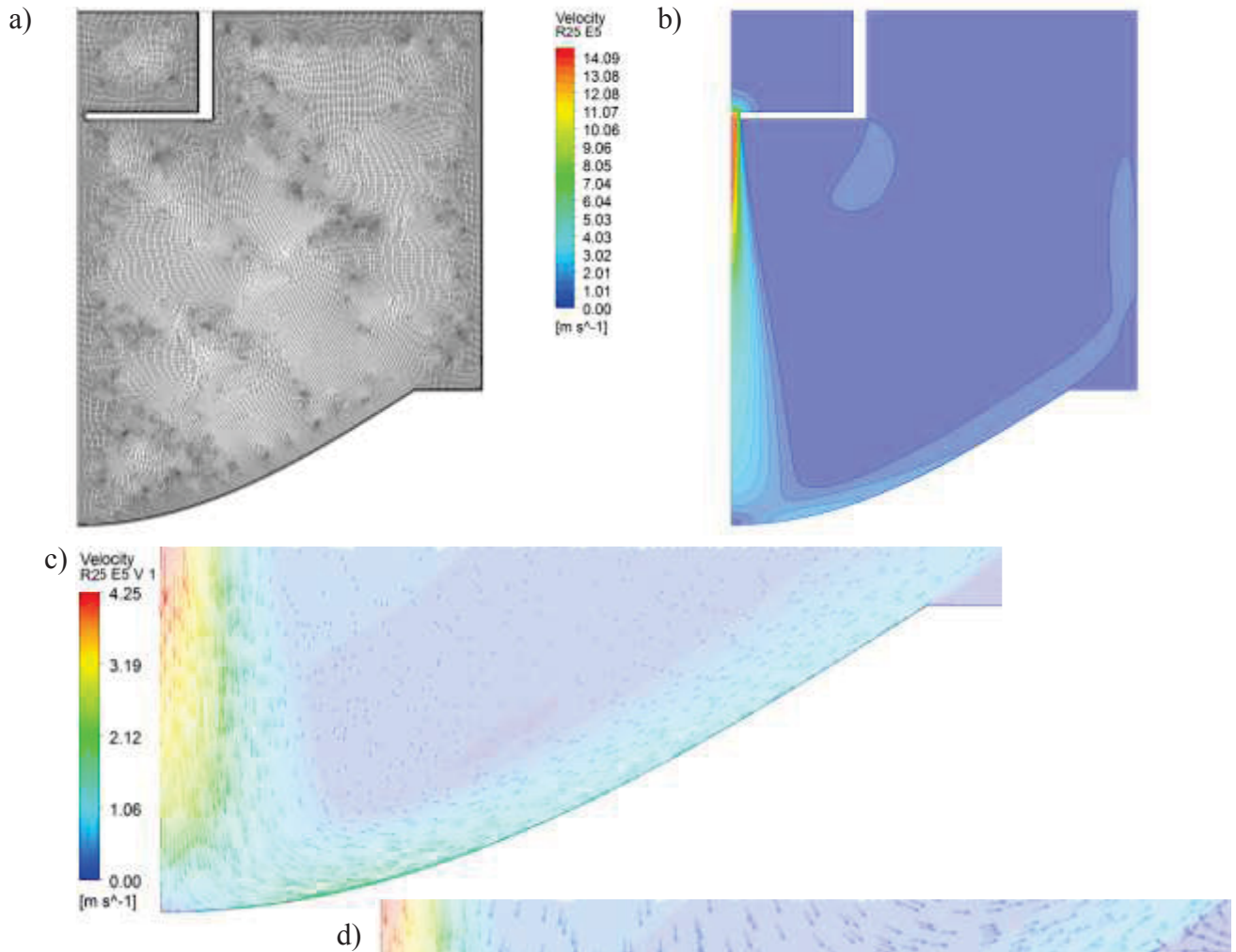| Depth, e (cm)	2.5
Radius, r (cm)	12.5
Ratio, R = ε/r	5
Nozzle Diameter, d (cm)	0.64
Initial Distance from Nozzle, H (cm)	10
Average Jet Velocity, U_0 (m/s)	10
Max Shear, τ (Pa)	60.53
Location of Max Shear Stress, r/H	0.125994

Depth, e (cm)	5
Radius, r (cm)	2.5
Ratio, R = ε/r	0.5
Nozzle Diameter, d (cm)	0.64
Initial Distance from Nozzle, H (cm)	10
Average Jet Velocity, U_0 (m/s)	10
Max Shear, τ (Pa)	32.68
Location of Max Shear Stress, r/H	0.155

Figure C-14 Result of Scour Hole Model, Depth = 5 cm, Radius = 2.5 cm. a) Mesh, b) Contours, c) Velocity Vectors within the Scour Hole, d) Normalized Velocity Vectors within the Scour Hole

Depth, e (cm)	5
Radius, r (cm)	5
Ratio, R = ε/r	1
Nozzle Diameter, d (cm)	0.64
Initial Distance from Nozzle, H (cm)	10
Average Jet Velocity, U_0 (m/s)	10
Max Shear, τ (Pa)	35.85
Location of Max Shear Stress, r/H	0.181

Figure C-15 Result of Scour Hole Model, Depth = 5 cm, Radius = 5 cm. a) Mesh, b) Contours, c) Velocity Vectors within the Scour Hole, d) Normalized Velocity Vectors within the Scour Hole

72

Depth, e (cm)	5
Radius, r (cm)	12.5
Ratio, R = ε/r	2.5
Nozzle Diameter, d (cm)	0.64
Initial Distance from Nozzle, H (cm)	10
Average Jet Velocity, U_0 (m/s)	10
Max Shear, τ (Pa)	42.16
Location of Max Shear Stress, r/H	0.134

Figure C-16 Result of Scour Hole Model, Depth = 5 cm, Radius = 12.5 cm. a) Mesh, b) Contours, c) Velocity Vectors within the Scour Hole, d) Normalized Velocity Vectors within the Scour Hole

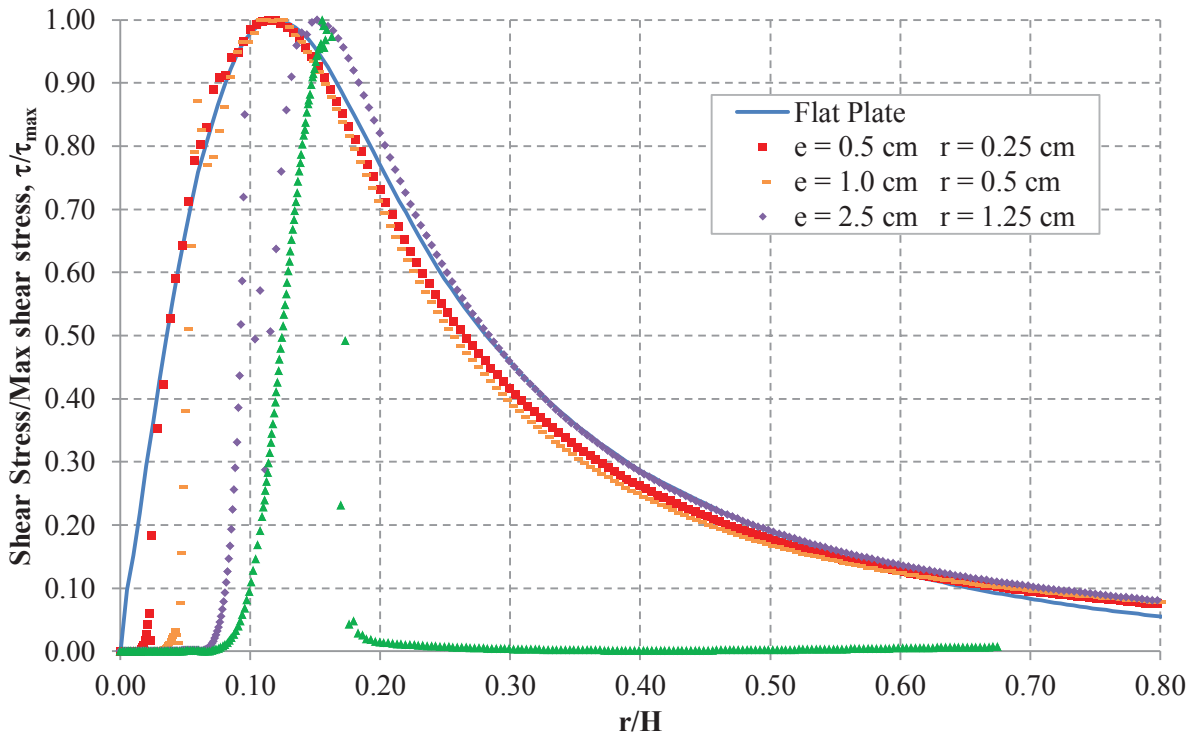## D. SHEAR STRESS PROFILES FROM NUMERICAL MODELS

Figure D-1 Nondimensional Shear Stress in scour holes with an Aspect Ratio of 0.5
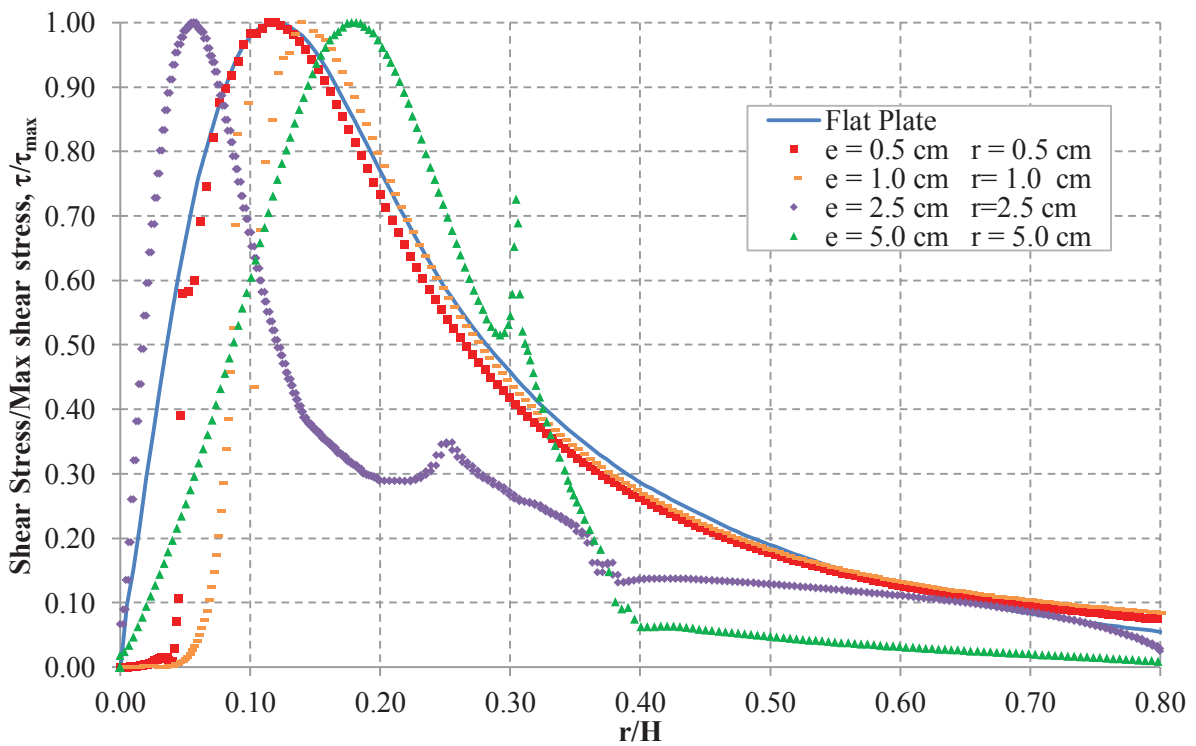

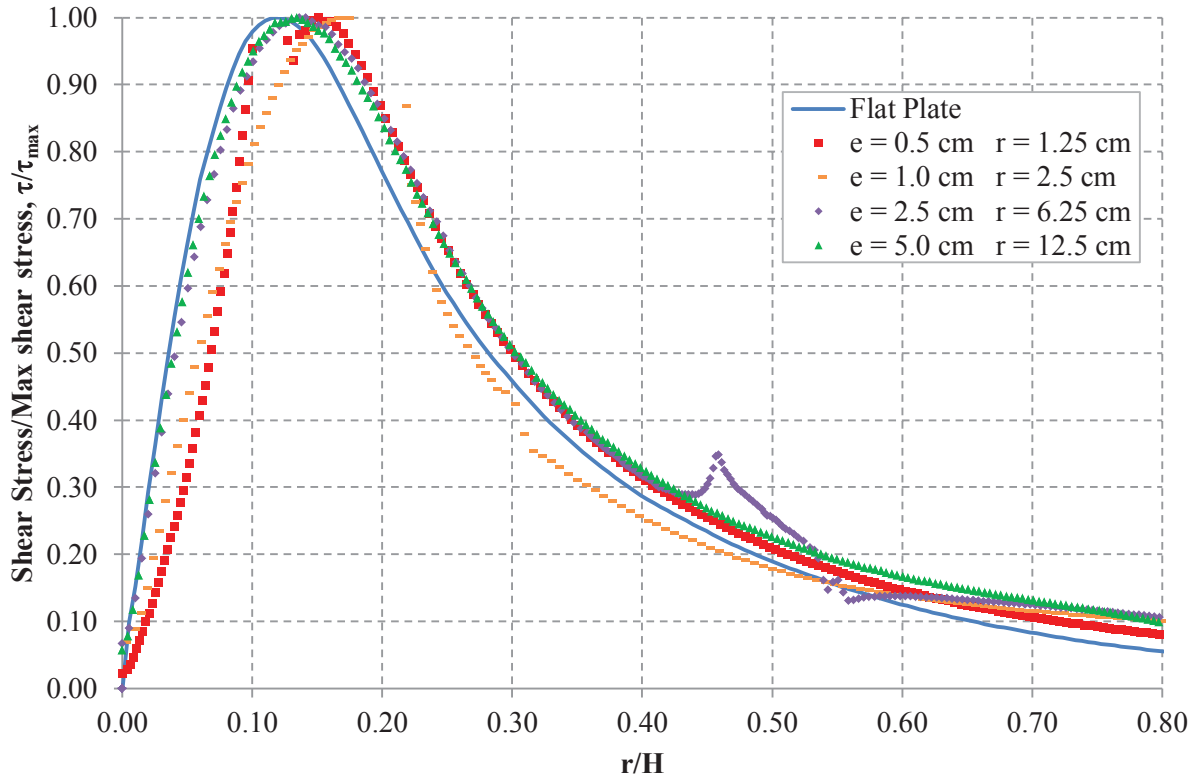Figure D-2 Nondimensional Shear Stress in scour holes with an Aspect Ratio of 1.0

Figure D-3 Nondimensional Shear Stress in scour holes with an Aspect Ratio of 2.5
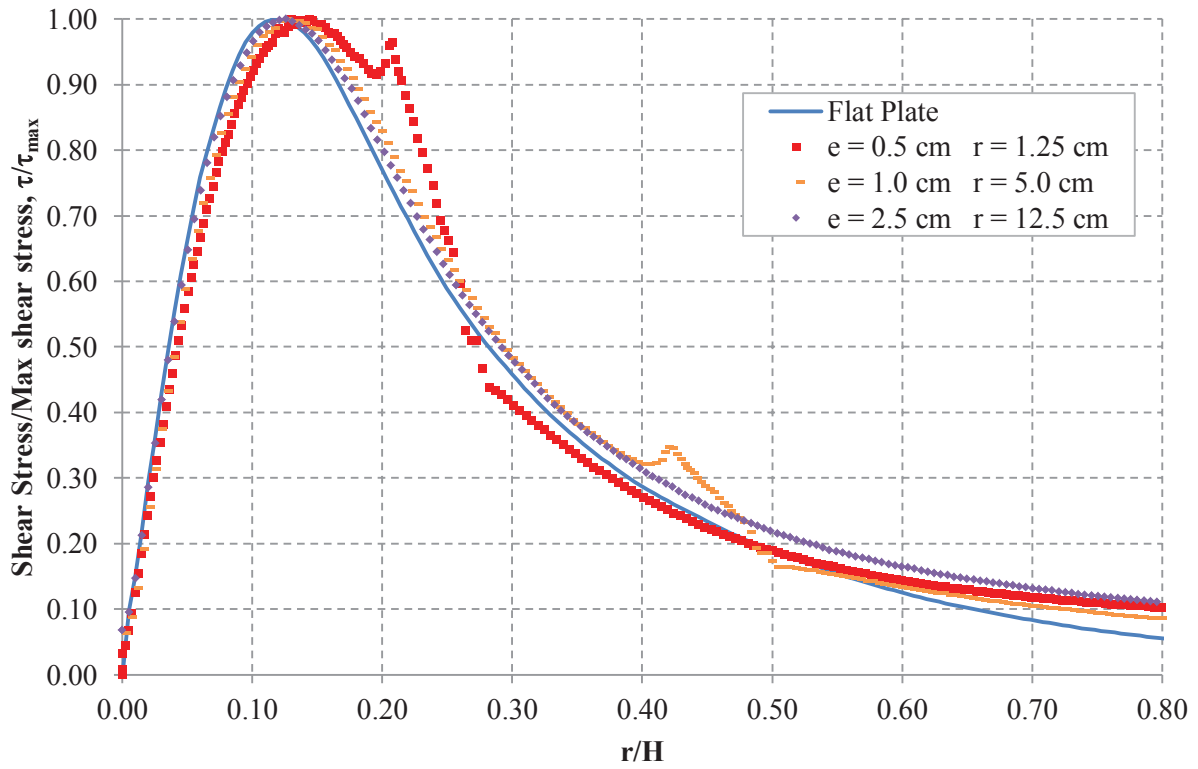

Figure D-4 Nondimensional Shear Stress in scour holes with an Aspect Ratio of 5.0

E. SCOUR HOLE SHAPES USED IN THE NUMERICAL MODELS OF THE MAZUREK LAB TESTS

Table E-1 Summary of the parameters used in the Numerical models based on one of Mazurek's Lab tests

d (cm)	0.8
H (cm)	11.6
Q (m^3/s)	0.00055

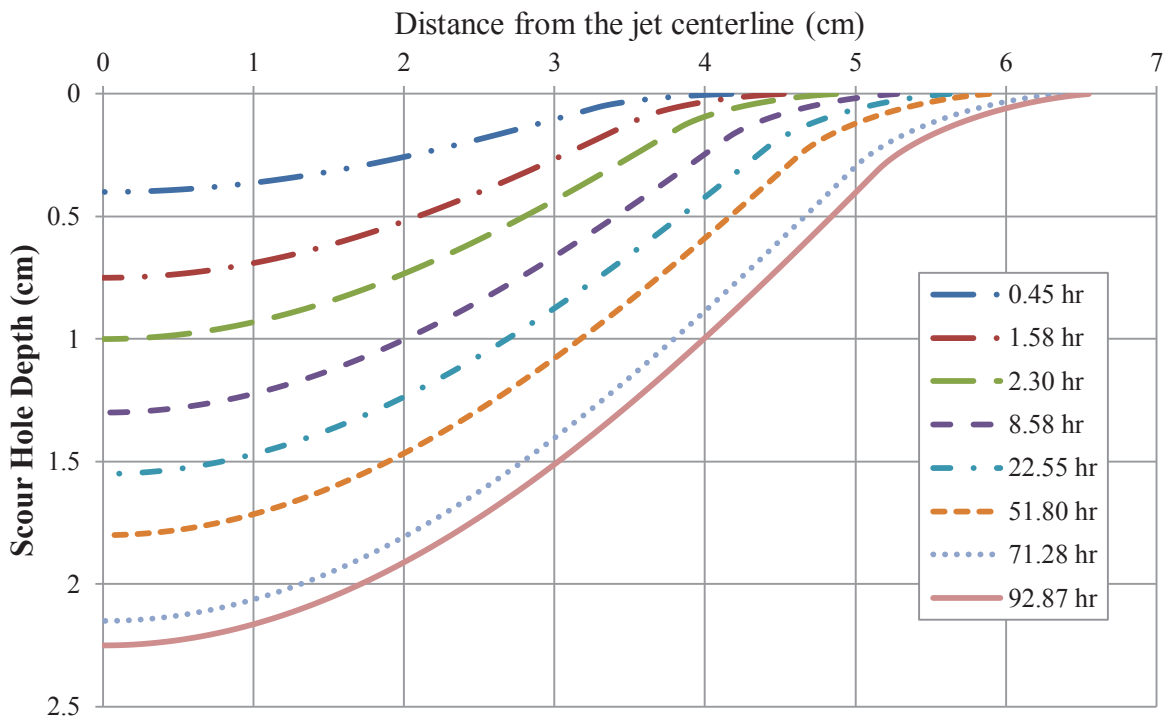| Time (min)	Time (hr)	Max disturbance (cm)		V (cm^3)	ε_m (cm)	ε_{cl} (cm)
		Width	Length			
0	0.00	0.0	0.0	0.0	0.00	0.00
27	0.45	6.4	8.0	19.0	1.40	0.40
95	1.58	7.5	8.1	25.0	1.50	0.75
138	2.30	7.8	9.0	30.0	1.50	1.00
515	8.58	8.5	9.7	43.0	1.60	1.30
1353	22.55	9.7	9.7	55.0	1.75	1.55
3108	51.80	10.2	10.1	70.0	1.85	1.80
4277	71.28	11.2	10.7	98.0	2.55	2.15
5572	92.87	11.7	10.9	99.0	2.55	2.25

Figure E-1 Scour Hole Geometry